Inorganic single crystalline bers for dual-readout calorimetry

Kristof Pauwels

▶ To cite this version:

HAL Id: tel-00803565

https://theses.hal.science/tel-00803565

Submitted on 22 Mar 2013

THÈSE DE L'UNIVERSITÉ DE LYON

délivrée par

L'UNIVERSITÉ LYON I - CLAUDE BERNARD

ÉCOLE DOCTORALE DE PHYSIQUE & ASTROPHYSIQUE

DIPLÔME DE DOCTORAT

(arrêté du 7 août 2006)
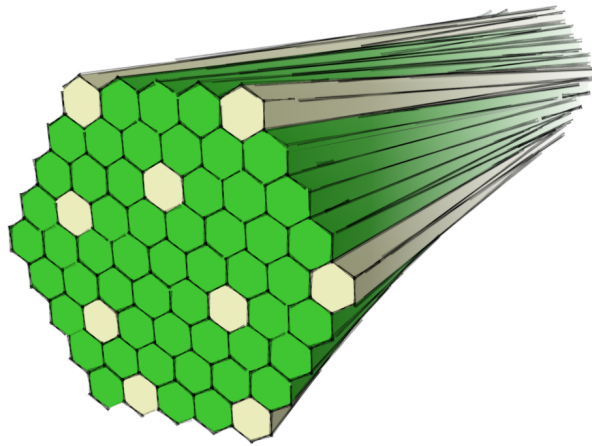
Inorganic single crystalline fibers for dual-readout calorimetry

KRISTOF PAUWELS

– 5 Février 2013 –

JURY D'EXAMEN

M. Bernard ILLE	*Président du jury*
M. Christophe DUJARDIN	*Directeur de thèse*
M. Paul LECOQ	*Co-directeur de thèse*
M. Martin NIKL	*Rapporteur*
M. Adam PARA	*Rapporteur*
Mme Anna VEDDA	*Examinateur*

Résumé

L'amélioration de la résolution en énergie des calorimètres hadroniques est adressée dans cette thèse. L'approche envisagée se base sur la technique du *dual-readout* qui consiste à détecter simultanément les radiations Cherenkov et la scintillation. La comparaison de ces deux signaux permet en effet de compenser les fluctuations observées dans la détection de gerbes hadroniques. Les grenats d'Aluminium et de Lutetium (LuAG), qui sont d'efficaces scintillateurs une fois activés avec des terres rares, peuvent aussi jouer le rôle de radiateur Cherenkov sous leur forme non-dopée. Les deux types de matriaux peuvent alors être assemblés pour former un calorimètre *dual-readout* performant. Dans l'objectif d'étudier la faisabilité de ce concept, les effets de la concentration en dopant et de l'addition de divers co-dopants sur le rendement lumineux et les propriétés temporelles ont été étudiés. Nous avons montré le rôle important de la technique de croissance choisie sur la nature et la concentration des défauts structuraux. La géométrie optimale, qui se base sur des monocristaux en forme de fibres, donne l'avantage à la technique de *micro-pulling down*. Cette technologie ne montre pas de meilleurs résultats que les techniques de Bridgman et de Czochralski mais a été retenue pour des raisons de coût et d'adaptabilité pour une production à grande échelle. L'optimisation des paramètres de croissance a permis la production de fibres monocristallines de LuAG dopées avec du Cérium présentant un rendement lumineux de 8000 photons par MeV et un bon comportement en tant que guide de lumière grâce à une qualité optique bien matrisée. Des tests avec des faisceaux d'électrons et de pions, en conditions de calorimétrie à haute énergie, permettent désormais d'envisager la production d'un prototype à plus grande échelle.

Abstract

This thesis focuses on the improvement of the energy resolution of hadron calorimeters. The approach is based on dual-readout, which consists in the simultaneous detection of both scintillation and Cherenkov light. The comparison of these two signals allows a compensation of the energy fluctuations, which are inherent to the detection of hadronic showers. Lutetium Aluminium garnets (LuAG), which are efficient scintillators when activated with rare-earth dopants (i.e. Cerium), can also act as Cherenkov radiators when undoped. Both undoped and doped crystals can then be assembled to build an efficient dual-readout calorimeter. With the objective to investigate the feasibility of this concept, the effects of the doping concentration and the use of various co-dopant on the light output and the timing properties of LuAG were studied. The growth method was demonstrated to induce significant differences in the nature and concentration of structural defects. The optimum geometry, which is based on single-crystals shaped into fibers, favors the micro-pulling down technique. This technology does not outperform Bridgman and Czochralski techniques but was chosen on bases of cost considerations and large scale productions abilities. The optimization of the growth parameters led to the production of single-crystalline fibers of Cerium-doped LuAG with a light output of 8000 photons per MeV and an adequate behavior as light guide due to a well-controlled optical quality. Test with electrons and pions in high energy calorimetry conditions allow to engage a future production of a larger-scale prototype.

Acknowledgements

I will start with the people of Lab 27 at CERN and first with *Paul Lecoq*. He had the initial idea of a dual readout concept based on inorganic scintillators and selected me for investigating its feasibility. By sharing his passion for scintillators and always asking unexpected questions, he injected a lot of curiosity in my research.

Then I had liked to thank *Etiennette Auffray*. Although not officially my thesis supervisor, she was the person who guided the organization of my research. The part of freedom that she gave me, allowed me to try new approaches which, in worst scenarios, at least explained me why the standard approach is actually a very good choice! More importantly, her trust in me made me trust myself. She also spent a lot of time in proof-reading not only the different versions of my thesis but also the different documents I wrote during these three years.

Many thanks to *Benjamin Frisch* who was there to answer any of my questions although he had a thesis to finish or/and simulations to run. Regardless of the topic, Ben has an opinion on anything. He was a very valuable adviser to me. Besides his office has this special thing: it triggers connections in my brain. Ben actually quickly got used to the fact that I often only start formulating a question and then go back to my desk because I understood. In the end, he only raised eyes when my talking was getting longer than expected!

I also had the opportunity to work with *Arno Knapitsch* who started his thesis one year before me. I am grateful to him for having showed me the reports that he wrote after each set of experiments. Such a good example was very useful to me since I used to have some difficulties to keep track of my experimental data! Arno also introduced

me to Litrani and spared me the time he spent in understanding this simulation tool.

I am also grateful to *Oliver Poppe*, who shared my office for five months and taught me how to measure light yields. I always tried to have the same remarkable care he had.

There is as well *Stefan Gundacker*, who started his PhD one year after me. He quickly became expert in the timing aspects of scintillation and during the last year of my thesis, he used to head to my office with lots of questions, challenging my understanding of these complex mechanisms. Although writing my thesis did not leave me enough time to discuss with him thoroughly, I learned a lot from the exchanges we had.

Special thanks to *Marco Lucchini* who became my office mate starting from February 2012. His expertise in test beam analysis was very precious for the last chapter of this thesis. I thought my data analysis was complete, quick and reliable and, well, he demonstrated that I could further improve each of these points!

I also want to thank *Alain Machard* who has been of high help in designing new benches, finding the adequate tools and the useful contacts at CERN. He left Lab 27 in December 2012 after 13 years of service as technician and we will miss him! Besides, I appreciated his habit to pass by my office to discuss the importance of the real world as opposed to the virtual world in which we, scientists, are hiding.

At least as much gratefulness goes to *Dominique Deyrail*. He is the technician you need if you are looking for a perfect surface state for your crystals. Far away from industrial polishing, it is with his fingers and patience that he will obtain the best you could hope, even if the crystal has an enormous crack hidden under the surface. His skills in machining where also very valuable for obtaining crystals holders designed with an outstanding accuracy.

I had liked to mention also the persons who gave me some company in my office during these three years: *Georgios Mavromanolakis, Daniel Edström, Florent Larrouturou, Kévin Trouilleux and Pawel Modrzynski.*

There are as well the persons that were just a few offices further: *Pier-Paolo Trapani, Guy Chevenier, David Bailleux, Iouri Musienko, Igor Tarasov, Norbert Frank, Tom Meyer, Pierre Jarron, Evangelia Dimovasili, Rita Giuffredi, Giulia Fornaro, Farah Ben Mimoun, Katayoun Doroud, Nicolas Di Vara, Marco Pizzichemi, Francesco Geraci* and *Alessio Ghezzi.* They did not hesitate to give me a hand when I needed it. Many thanks to all of you ! I feel ashamed to just cite the name of these persons but I cannot decently make this section longer than the rest of this document...

In return, I had the pleasure to help some of them. I am grateful to the persons who entered my office looking for an answer. They thought they would annoy me and waste my time but they were wrong! I learned a lot from their questions: by explaining things I realized I did not completely understand them myself! Besides these exchanges often triggered new ideas. My only hope is that I succeeded to help them as much as they did. A special memory goes to the trainees Claire-Anne Reidel and Jean Torion-Hudry who were the first I had the opportunity to advise.

Of course I cannot omit the daily 10 o'clock coffee appointment where *Renaud Bruneliere, Stefan Rossegger* and *Gerhard Burghart* used to join us.

Working in Lab 27 was a great pleasure, the mix of so many cultures (Austria, Belgium, France, Germany, Greece, India, Iran, Italy, Poland, Russia, Sweden and United-States !) was an incredible experience and I am happy to say that more than new colleagues, I found new friends.

Contents

Chapter 1

Introduction

Understanding the world we are living in is a challenge. Its surprising success to prevail in time and the complexity of its mechanisms are difficult to apprehend. What are we made of? This very simple question is one of the most difficult to answer. People have always tried to segment the different parts of our world into elementary objects. The idea that all matter is composed of elementary particles dates actually from the 6th century BC. Since then, science made a lot of progress, especially during the last decades and many fundamental questions could eventually be answered. Nevertheless, scientists were forced to admit that the further they were digging, the more complex the answers were becoming.

1.1 High Energy Physics

Fundamental physics is trying to find a unity, a common model for all the parts of the universe. These models can however only be meaningful when confronted to reality. Since the focus is set to the tiniest elements of matter, the conditions in which they could be observed are getting more and more difficult to achieve. This exploration is done at the limits of Physics: the High Energy Physics (HEP). HEP experiments are based on accelerated particles that are collided at very high energy (at the TeV-scale). Each collision creates extreme conditions where new physics is then likely to emerge.

Designing and operating accelerators that provide the required energy range to various particles is not the only challenge. The careful observation of what happened during the collision is critical. The detectors placed around the location of the collision have to provide the physicists with the maximum amount of information describing all the sub-products created (number, nature, energy, momentum, lifetime, etc). High precision of the information provided by the detectors is necessary for the full reconstruction of the details of the collision.

1.2   Calorimetry

When interacting with matter, high energy particles lose energy by generating a cascade of secondary particles. The energy of these particles decreases progressively as the shower develops. In calorimeters, the deposited energy is detectable in the form of a signal which is proportional to the incoming energy. In order to accurately estimate the total energy deposition (the sum of the energies of all sub-products), it is critical to contain the particle shower in the detector. If the leakage energy (energy not deposited in the detector) gets too large, the resolution indeed degrades quickly. Fulfilling this condition while keeping realistic dimensions forces calorimeter designs to be based on dense materials. Scintillation light is often used as a detectable signal in calorimeters. In this case, the shower particles transfer the energy to the material of the calorimeter which is then converted into either UV, visible, or NIR photons which in turn are measured with photodetectors and allow estimating the energy deposit.

It is possible to distinguish electromagnetic calorimeters from hadronic ones. They differ by the type of particles they were designed to study. Electromagnetic calorimeters measure the energy of electromagnetic showers made of electrons, positrons and photons. On the other hand, the showers generated by hadrons (mainly constituted of pions and nucleons) which interact through a succession of various inelastic interactions are studied with hadronic calorimeters. Of course hadron calorimeters do not only focus on hadronic cascades since part of the secondary particles generated (the charged ones) yield electromagnetic cascades. Hadronic calorimeters have actually to deal with both processes and the challenge is to equalize their response to these two signals.

Regardless of the type of calorimeter considered, the actions of stopping the particles and measuring their energy can either be performed in the same volume (homogeneous calorimeters) or in separate volumes (sampling calorimeters).

1.2.1 Homogeneous calorimeters

Homogeneous calorimeters act simultaneously as absorber and active medium. Good energy resolution requires that the leakage energy to be as small as possible, hence it is necessary to maximize the density of the calorimeter. This strongly limits the choice of material. Because heavy inorganic scintillators combine a high density (good stopping power), a high scintillation light yield (efficient energy conversion) and a high transparency (efficient signal extraction), they are excellent candidates. Homogeneous calorimeters can more easily be designed to contain and measure the entire incoming energy but their energy response depends on the nature of the particle interaction and can consequently degrade the energy resolution.

1.2.2 Sampling calorimeters

Sampling calorimeters alternate layers of passive dense material that play the role of absorber and layers of active material that measures the energy absorbed in between layers. Stacking two materials allows an optimized choice for each. The absorber can be selected for its stopping power without any other restriction and the active media only needs to yields the highest signal. Compared to homogeneous calorimeters, sampling calorimeters allow more compact designs. Their performances are however limited by sampling fluctuation since, by definition, sampling calorimeters only measure a fraction of the total energy of the particles. In order to obtain an accurate measurement, this fraction should be the same for all shower particles. This is difficult to achieve since the sampling fraction also depends on the particle type and momentum.

1.3   Calorimetry at CERN

1.3.1   Historical background

To reinforce the scientific unity in Europe after World War II, the creation of a European laboratory was suggested by the French Nobel Prize Louis de Broglie in 1949. Since the early 20th century, nuclear physicists were making tremendous progress and this field quickly became a natural choice for the creation of the laboratory. This idea came to reality in 1954 and twelve states became member of The European Organization for Nuclear Research (CERN). In 1960, the first major particle accelerator, the Proton Synchroton (PS) was built and energies up to 28 GeV could be studied. In 1976, the Super Proton Synchroton (SPS) brought the energy level up to 400 GeV. Subsequently, the Large ElectronPositron Collider (LEP) was built in 1989. This collider was hosted in a circular tunnel of 27.6 km long located 100 meters underground. Two beams of high energy electrons and positrons were injected into the LEP rings. Traveling in opposite directions, they were gaining energy with every lap. Once the operational energy reached, the two beams were collided. In the last years of operation, the collision energy reached 209 GeV and this accelerator became then the most powerful lepton accelerator ever built. The LEP was stopped in 2000 to be replaced by the Large Hadron Collider (LHC).

1.3.2   The Large Hadron Collider (LHC)

The Large Hadron Collider (LHC) uses the same tunnel that previously hosted the LEP. This tunnel spans the Franco-Swiss border near Geneva (see Figure 1.1). Contrary to the lepton accelerator, the LHC has its two beams composed of either protons or lead ions. When being accelerated transversally (as it is in a circular accelerator), light particles such as leptons lose energy through synchrotron radiation. Because of this, the energy of the LEP beams could not reasonably exceed the 104.5 GeV achieved in 2000. On the contrary, hadrons like those accelerated in the LHC, are not limited by synchrotron radiation since their mass is much higher. The upper limit of their energy is fixed instead by the maximum value achievable for the magnetic field of the accelerator. To force the particles
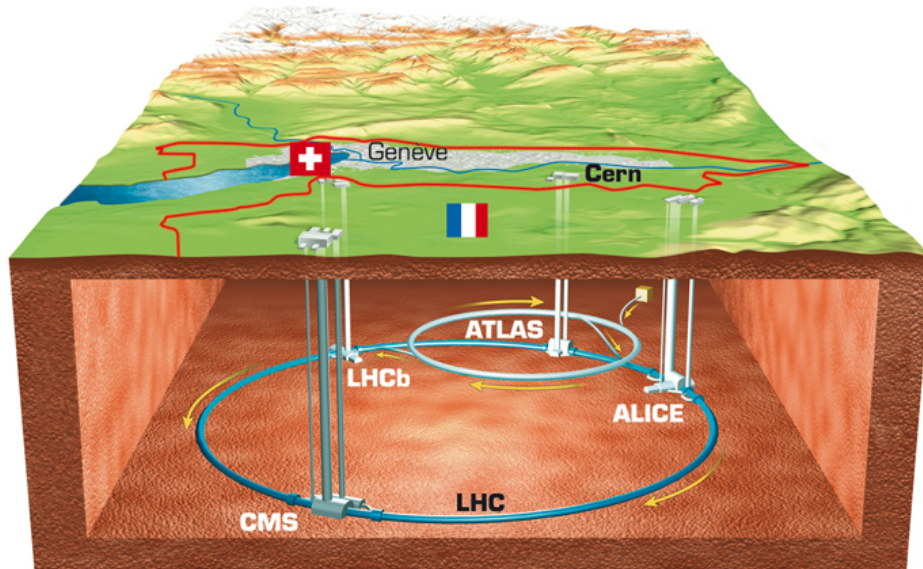
Figure 1.1: Artist view of the underground Large Hadron Collider.

to follow circular trajectories, intense magnetic fields are indeed required. When the particle energy increases, then this magnetic field must increase as well. To reach the 14 TeV collision energy planned by the LHC original design, 8.3 T are required. This very intense magnetic field is obtained with superconducting magnets of niobium-titanium (Nb-Ti) operated at 1.9 K. Ensuring a safe operation of these magnets while 10.4 GJ [1] are being stored in them is complex and will require future upgrades of the collider.

Nevertheless, starting from the first collisions at 7 TeV in March 2010, the performances of the LHC have been impressive. Since April 2012, the two beams are operated at 4 TeV, resulting in a new record collision energy of 8 TeV. Fine tuning of the machine then allowed increasing the collision rate. On the 4th of July 2012, the LHC received a lot of attention when it was officially announced that the gigantic number of these high energy collisions led to the discovery of a new boson. It is very likely for this boson to be the famous Higgs boson that the standard model predicts. The LHC thus successfully opened a track for new physics and new answers.

The outstanding energy required for such discovery is of course not reached at once and both PS and SPS (previously mentioned in 1.3.1) are necessary to progressively increase the energy of the particles before their injection into the LHC. The chain of accelerators is presented in Figure 1.2.
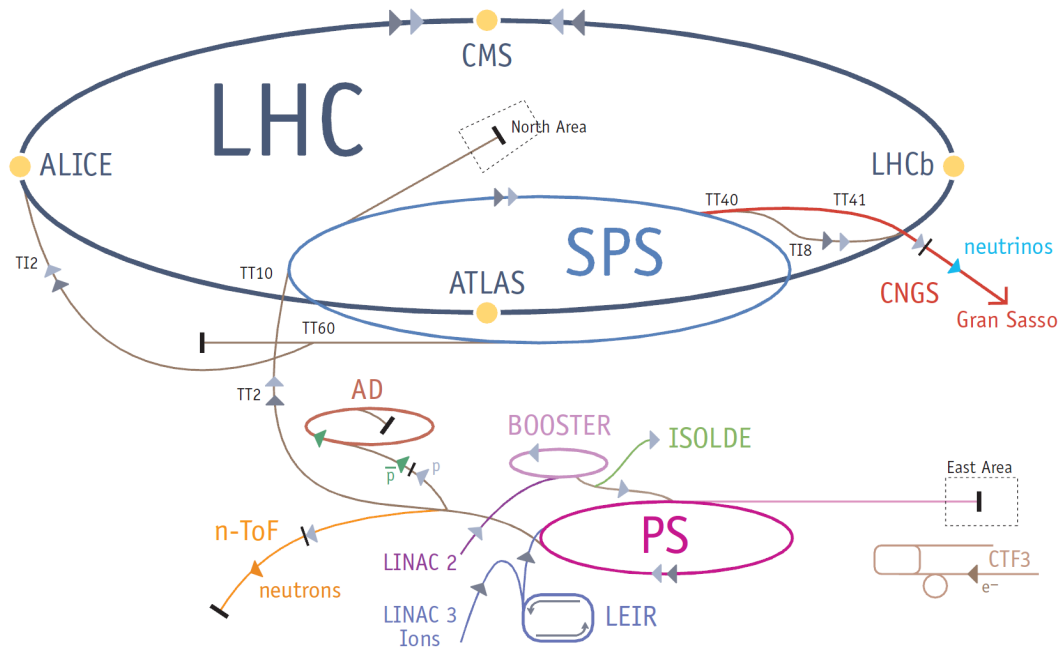
Figure 1.2: Complex of accelerators at CERN

Linear accelerators (LINAC) are the first elements of the accelerator chain. The protons, obtained from Hydrogen atoms from which electrons have been removed, are accelerated along a straight line to an energy of 120 MeV. Then three successive synchrotron accelerators (the Booster, the PS and the SPS) bring their energy respectively to 1.4, 26 and 450 GeV. Once or twice a day, the protons of the SPS are injected into the LHC and accelerated to their final energy (see Figure 1.3 for details on injection cycle). With its 27.6 km, the LHC can store a lot of particles but the objective is not to collide them all at once! The particles are organized in bunches spaced by 50 ns. At the collision points, the two beams intersect and protons of the two bunches collide. An accurate operation of each component in the accelerator chain is in principle able to provide between 10 and 20 hours of collisions.
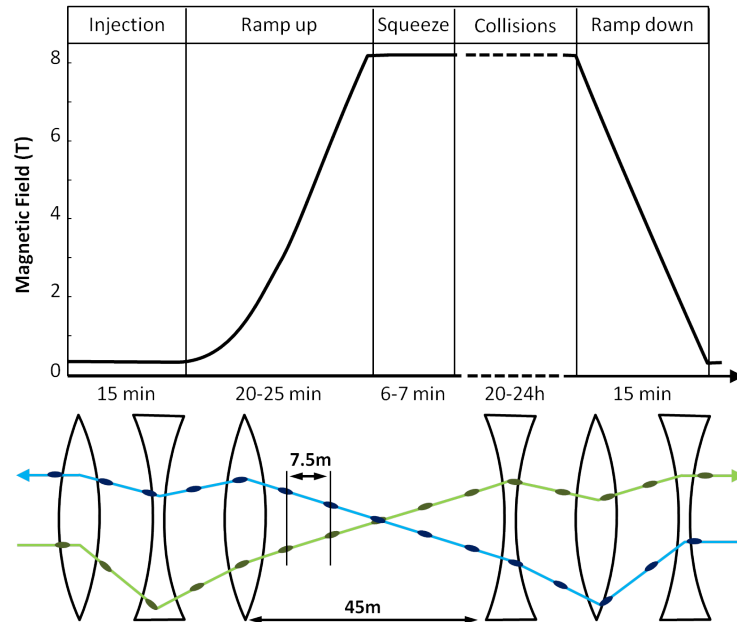
Figure 1.3: Collision Cycle (top) and bunches structure (bottom).

At the collision points, four huge underground caverns host complex detectors. The two largest experiments are ATLAS and CMS and are designed to investigate the largest range of physics possible. The latter experiment will be presented in more details in the next section.

1.3.3 The Compact Muon Solenoid (CMS)

The Compact Muon Solenoid (CMS) is a huge detector that can build up a picture of events at the heart of the collision. *Compact* depends on the point of view since the cylindrical detector is in fact a barrel of 14.6 meters in diameter and 21.6 meters in length. The term *muon* refers to one of CMS objectives that is measuring the momentum of the muons produced by the highly energetic collisions. Muons are unstable (mean half-life time is 2.2 μs) negatively charged leptons. They differ from electrons by their mass that is 207 times higher. For these heavy particles, the Bremsstrahlung effect, which is the main energy loss for leptons (see section 2.1.1), is less intense since it is harder to bend these heavy particle trajectory. Muons momentum are therefore very difficult to measure.

The term *solenoid* refers to the 4-T superconducting magnets that provide a large bending power to compute the muon momentum with a better precision.

The role of CMS is however not restricted to the measurement of muons. Its multilayer design allows in fact the measurement of a wide range of particles. A perspective view of the CMS detector is provided in Figure 1.4. Muons chambers can be seen inside the iron return yoke of the magnet. In the bore of the magnet coil, we can see three concentric layers: the particle tracker, the electromagnetic calorimeter and the hadron calorimeter. These layers are shortly presented in the following.
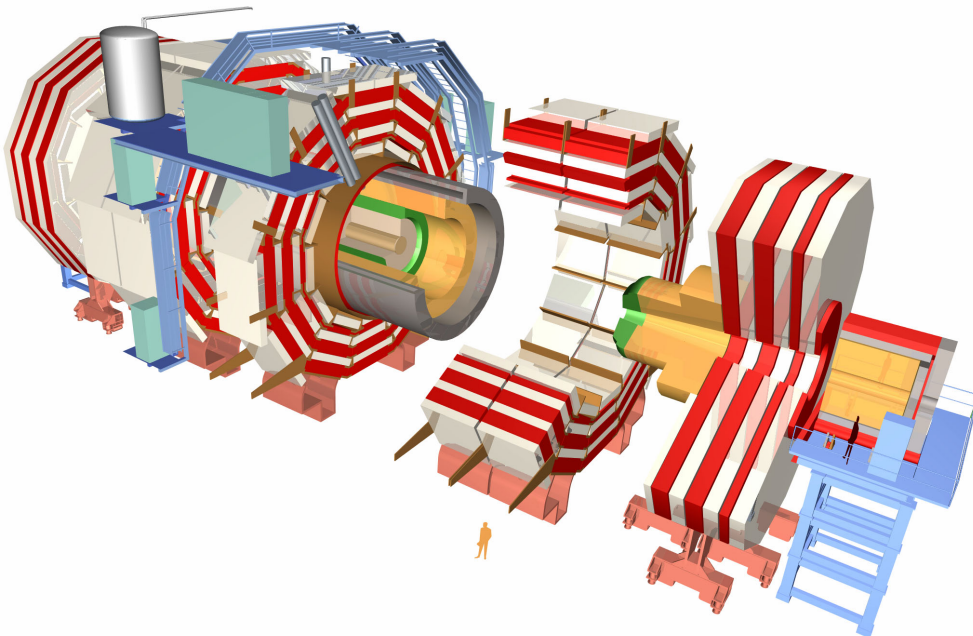
Figure 1.4: The CMS design

Tracker   At the heart of the collisions, the tracking detector records the path of all particles with a high granularity. It consists of ten layers of silicon microstrip detectors and three layers of silicon pixel detectors. The latter one improves the measurement of the impact parameter of charged particles, thereby allowing detection and reconstruction of short-lived particles

ECAL   Just after the tracking volume, two layers of calorimeters measure the energy of the products of the collisions. The first layer is an electromagnetic calorimeter (ECAL) made of lead tungstate (PbWO$_4$) crystals. A fully hermetic structure of 75848 scintillating single crystals (61200 in the central barrel and 7324 in each of the two endcaps), each of dimensions around 2.2×2.2×23 cm^3, has been organized around the tracking volume. PbWO$_4$ was selected for its high density (8.28 g/cm^3) and short radiation length and Molière radius (will be defined in next chapter). This results in a fine granularity and a compact calorimeter. Although the light output is relatively low, the crystals are optically clear, fast enough to meet the LHC collisions repetition rate of 50 ns and have a good energy resolution, inherent to a homogeneous calorimeter. In addition they posses a good radiations hardness.
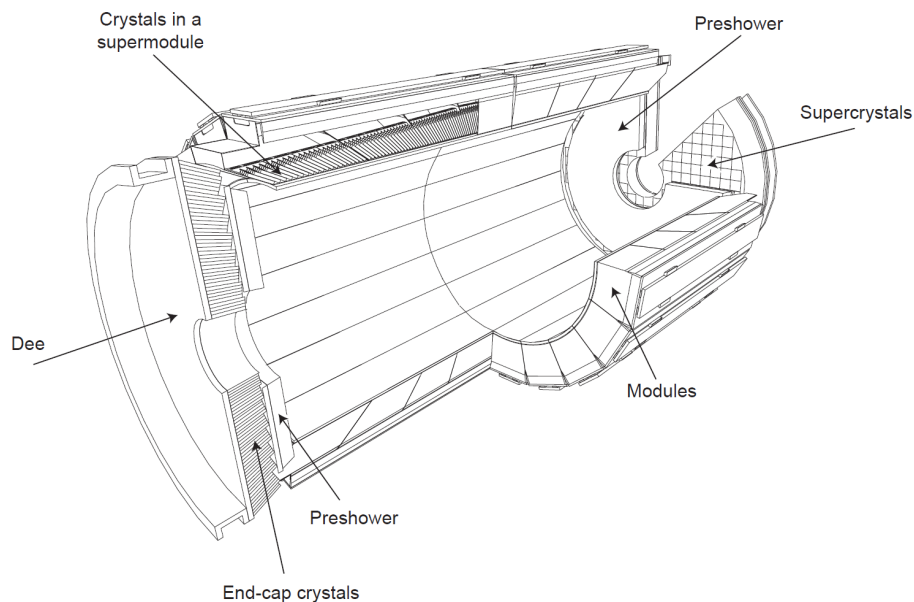
Figure 1.5: The ECAL design [2]

The crystals of the barrel have a tapered shape, slightly varying with their position (see Figure 1.5). They are mounted in a quasi-projective geometry to avoid cracks aligned with particle trajectories, so that their axes make a small angle ($\sim 3°$) with respect to the vector from the collision point. Because of this truncated pyramidal shape the light collection is non-uniform along the crystal

length. One lateral face was therefore depolished in order to meet the uniformity requirements [68]. In the endcaps, the light collection is naturally more uniform because the crystal faces are nearly parallel. Besides, their geometry does not need fine adjustments, contrary to the barrel.

The scintillation light of the $PbWO_4$ is detected by silicon avalanche photodiodes (APDs) and vacuum phototriodes (VPTs) respectively in the barrel and the endcap regions.

HCAL The ECAL, is surrounded by a second calorimeter dedicated to the detection of hadrons (HCAL), that forms the last layer of detector inside the magnet coil. Contrary to the ECAL, the HCAL is a sampling calorimeter composed of brass and plastic scintillators. As shown in Figure 1.6, there are four different regions in HCAL: the hadron barrel (HB), both endcaps (HE), the outer calorimeter (HO) and the forward calorimeter (HF).
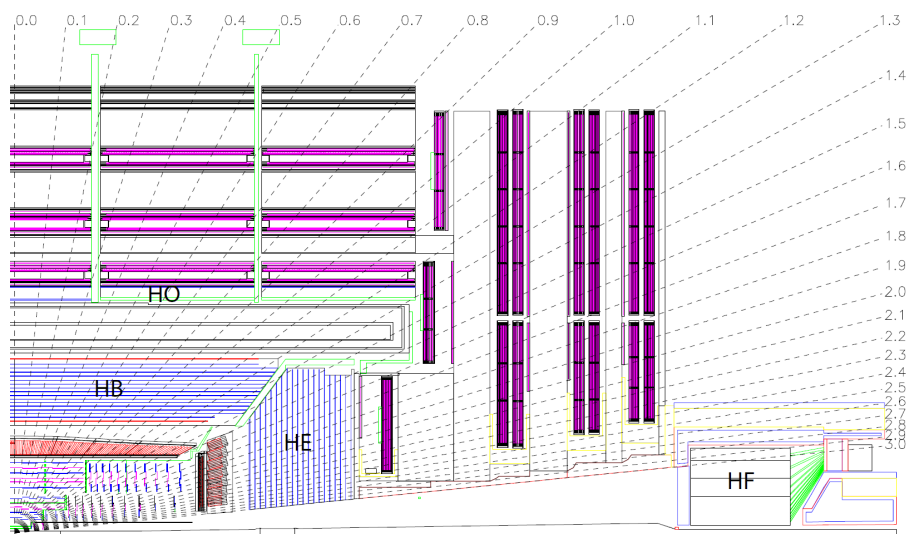
Figure 1.6: Longitudinal view of the CMS detector. [2]

The barrel (see pictures in Figure 1.7) and the endcaps are made of repeating layers of brass absorber and megatiles of plastic scintillator. Secondary particles produced in the absorber generate scintillation light in these tiles. Wavelength-shifting (WLS) fibres then shift the signal towards longer wavelengths. The signal

is finally channeled through optical fibres to the readout boxes where it is detected with hybrid photodiodes (HPDs).
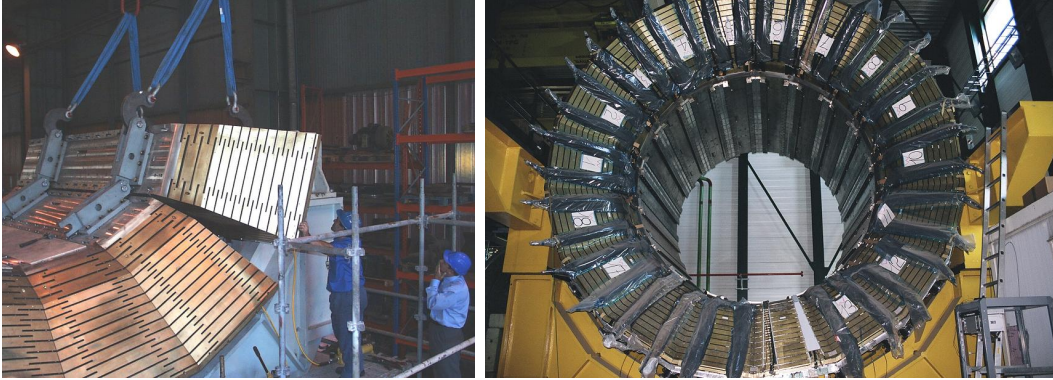
Figure 1.7: Hadron barrel calorimeter assembly (left) and when ready for insertion into the magnetic coil (right). [3, 4]

This central calorimetry (HB and HE) is complemented by a tail-catcher: the outer barrel HO. Finally, two hadronic forward calorimeters (HF), positioned at both ends of CMS, measure the particles coming from the interaction point with a shallow angle. Because of its forward location, HF must be very resistant to radiation and therefore this calorimeter is based on quartz fibres.

Muon chambers The last layer of the detector are muon chambers. These chambers are located inside the flux-return yoke that serves as an absorber for the identification of muons. Similarly to the previous layers, this muon system is divided into a barrel region and two endcaps. In the barrel region, because of the low muon rate and uniform magnetic field, standard drift tube (DT) chambers were selected. These chambers are organized into 4 stations interspersed among the steel yoke (see Figure 1.8). Contrary to the barrel, both endcap regions present higher muon rates together with higher background levels and non-uniform magnetic field. Therefore, the endcap muon system is based on cathode strip chambers (CSCs). These detectors identify muons with fast response time, fine segmentation, and good radiation resistance. They provide robust pattern recognition for rejection of non-muon backgrounds.
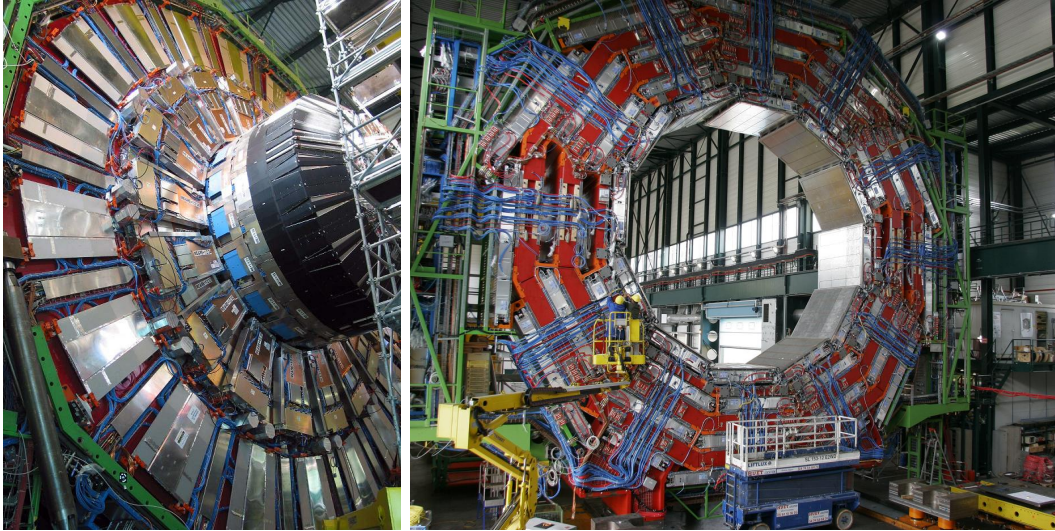
Figure 1.8: Endcap muon chambers with CSC (left) and barrel muon chambers with DT (right). [5, 6]

A complementary trigger system consisting of resistive plate chambers (RPCs) was also added in both the barrel and endcap regions. These RPCs provide a fast, independent, and highly-segmented trigger which improves the muon momentum resolution.

1.4   Improving the calorimeters performances

The key parameter of calorimeters is their precision and most of the research performed in this field aims at improving it. This precision is determined and limited by fluctuations since calorimeters are based on physical processes that are inherently statistical[7]. In the case of electromagnetic (em) calorimeters, the mechanisms of interactions makes it possible to detect them with high precision [8]. In a homogeneous detector, the energy resolution is indeed only determined by the shower leakage fluctuations and instrumental effects. When the detector size becomes a limitation (e.g. in space applications), sampling em calorimeters have to be considered. For these ones, the sampling fluctuations (determined by the sampling fraction and frequency) dominates the two previous factors.

Hadron calorimeters are affected by the same factors listed for em calorimeters. Among these sampling fluctuations are the most important. The first reason is due to the fact that the paths of hadrons in matter are longer and therefore the sampling geometry is often adopted to keep realistic detector dimensions. Sampling fluctuations are in addition larger for hadrons, typically by a factor of two [7], which further degrades the detector resolution. Contrary to em particles, spallation protons, which dominate hadronic shower signals, may indeed traverse several active calorimeter layers. Additional fluctuations result from the nuclear reactions involved in hadron-matter interactions. Nucleons from nuclei can be released and their binding energies are usually undetected. Fluctuations in this *invisible* energy form the ultimate limit to what is achievable in terms of hadronic energy resolution. Another additional reason for energy resolution degradation in hadron calorimeters is due to the higher sensitivity of most common detectors to em particles as compared to non-em particles and unfortunately both are produced in hadronic showers. The exact number of each is unpredictable because the same particles do not always generate the exact same shower. As a result, large non-Poissonian fluctuations in the response of the detector are observed [9]. Correcting these fluctuations in the em fraction of the shower (fem) is the key to improve the energy resolution of hadron calorimeters. This correction also enhances the linearity of the system since the average em shower fraction is energy dependent. Several approaches exist, here comes a review of each.

1.4.1 Compensating calorimeters

In compensating calorimeters, fluctuations in the fem can be ignored by design. The sampling fraction of these calorimeters have been precisely tuned in order to deliver equal response to the em and non-em shower components: e/h=1. Their performances are however limited since good em showers detection resolution requires a high sampling fraction (ideally 100%) whereas good hadronic shower detection resolution requires this fraction to be small (typically 2.3% in lead/plastic scintillator calorimeters [10, 11]). For this reason, compensating calorimeters still force the users to decide what showers detection (em or non-em) they want to favor. In addition, since these calorimeters rely on the contribution of neutrons, they require large detector volumes, which is rarely affordable.

1.4.2 The Particle Flow (PFlow) approach

This method combines the calorimeter information with advanced tracking measurements. The tracking system is used to reconstruct the four-momentum of every single particle of all events recorded in the detector. This particle identification is then used to correct the energy measurements of the calorimeters. CMS is actually using the PFlow technique to improve its calorimetry measurements. For this method to be fully effective, the detector should however present a high granularity (much higher than CMS) in both longitudinal and lateral segmentation [12]. The maximum level of performance is achieved when all energy deposits can be perfectly associated with the correct particles. Therefore, in practise, the limiting factor in PFlow calorimetry is not the calorimetric performance but the possible confusion between two particles [13]. In recent years, high granularity PFlow calorimetry made a lot of progress. In the context of the proposed International Linear Collider (ILC)[14], the CALICE collaboration [15] proposed advanced PFlow sampling calorimeter designs based on silicon tungsten sandwiches [16, 17]. This highly segmented calorimeters have however a huge number of channels and might present complex engineering problems to extract the signals and enable effective pattern recognitions.

1.4.3 The Dual-Readout approach

While the PFlow method uses the particles tracks to separate em from non-em interactions, the Dual-Readout Method records two separate signals (dual readout) of the active layer in order to estimate the fraction of the energy carried by em particles. The delicate choice of the two complementary estimators originated from prototype studies for the HF calorimeter of the CMS experiment [7]. In this calorimeter, based on quartz fibers, the non-em shower component is indeed suppressed by a factor 5 [18]. Although strongly non-compensating, these quartz fibers turned out to be a very good estimator of the em interactions occurring in the detector! The signals recorded in these quartz fibers are actually based on Cherenkov light generation. This characteristic light is emitted when a charged particle passes through a dielectric medium of high refractive index (the particle speed becomes greater than the phase velocity of light in that medium). Spallation protons produced in hadronic showers through nuclear reactions are usually not sufficiently relativistic to produce Cherenkov light. On the other hand, electrons and positrons from the em shower component are relativistic down to a fraction of 1 MeV [9]. The amount of light in the quartz fibers is thus a measure of the energy carried by em component of the shower development. The Cherenkov light is therefore a natural threshold for discrimination of the em and non-em particles.

Based on theses observations, the DREAM collaboration built a prototype equipped with both quartz fibers and scintillating (these ones measure the total energy deposition) embedded in a brass matrix (acting as absorber). The hadron showers generate signals in both types of fibers and by measuring these signals simultaneously, one learns how much energy was deposited in the calorimeter and what fraction of that energy was carried by π^0s and ηs. R. Wigmans and his group initiated a set of real conditions test with high energetic muons [19], electrons [20], and hadrons [8]. The results showed that this method worked very well: hadronic signal linearity was restored, the response functions became Gaussian, and the energy resolutions improved considerably, especially at the highest energies [21].

1.4.4 A novel type of dual-readout

The original design of the DREAM calorimeter is based on a sampling calorimeter. For this reason, its resolution, although improved by fem correction, is limited by sampling fluctuations. The concept of a dual readout can also be applied to homogeneous detectors based on bulk scintillating crystals. In order to read both scintillation and Cerenkov signals, several properties of Cerenkov light can be exploited. As opposed to the isotropic scintillation light, Cherenkov light is directional. The signals also differ from the point of view of timing: Cherenkov light is prompt whereas scintillation light decays exponentially. Finally, both lights have different emission spectra. All three different discriminations were tested by the group of R. Wigmans [22] and also in our group [23]. Although these tests demonstrated that dual-readout principles can effectively be applied to a homogeneous design, one limitation has to be considered : the non-negligible coupling between Cerenkov and scintillating signals. The excitation spectrum of most common scintillators is indeed overlapping the continuous Cerenkov emission spectrum. This means that some Cerenkov signal can be absorbed by the luminescent centers and be read as scintillation light. None of the different discrimination techniques is unfortunately able to correct for this effect. To circumvent these limitations, P. Lecoq proposed an alternative to these approaches, combining their relative merits and limiting their drawbacks [24, 25]. With the proposed approach it is possible to conceive detector blocks made of trunks of *cables* constructed from heavy inorganic scintillating crystal fibers, as illustrated in Figure 1.9.

By selecting scintillating materials activated by a doping ion, instead of self activated scintillators, it would be possible to mix both doped and undoped fibers of the same material, which would then behave respectively as scintillators and Cerenkov radiators [26]. The detector obtained would then be dense enough to avoid the necessity of a passive absorber (thereby excluding sampling fluctuations). Besides, this system would be capable of disentangling the em and non-em components of a shower with a uniform radiation length, Moliere radius and interaction length (details on these values can be found in the next chapter). In addition, the fiber geometry allows some flexibility in the choice of detector

geometry. With a hexagonal fiber section a minimum dead space is achieved. The light produced by each type of fiber can then be collimated by diffractive optics onto silicon photomultipliers. Both sides of the detector block can be read out in order to further improve the quality of the signal by correcting for the depth of interaction of the impinging particle.
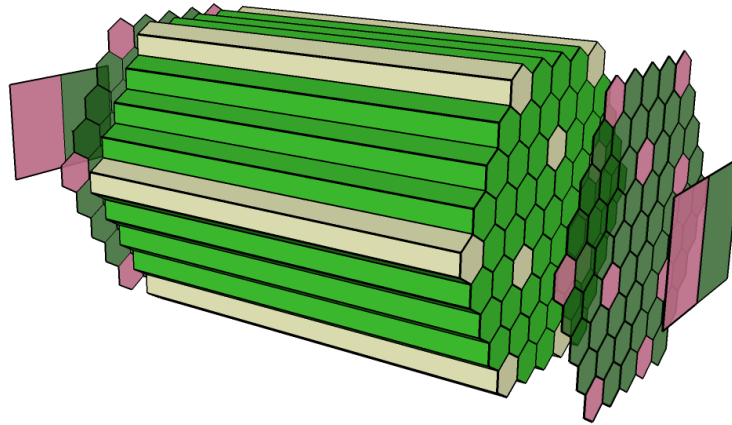
Figure 1.9: Design of a dual readout calorimetry concept based on meta-crystals.

Lutetium Aluminium Garnet (LuAG) appeared to be a good candidate as host material [23, 27] because it combines a high density (high stopping power), a high refraction index (strong Cerenkov signal) and good doping capabilities (fast and intense scintillation). Besides, this material shows good mechanical and chemical properties that favor shaped crystal growth.

1.5 Scope of this thesis

This thesis focuses on the type of dual-readout calorimetry described in previous section. The thesis is organized as follows:

The next chapter will first review the important physical principles that were only shortly mentioned in this chapter. The experimental methods to characterize heavy inorganic scintillating crystals will be described in chapter 3. The effects of the Cerium doping concentration and the use of Hafnium and Scandium as co-dopant on the light output and the timing properties of garnets of Lutetium and Aluminum (LuAG) will be studied. We will then show in chapter 4 that the choice of the growth method induces significant differences in the nature and concentration of traps in LuAG. In chapter 5, the effect of the fiber geometry on the light collection will be studied and the importance of growing fibers with high quality surfaces will be emphasized. Single-crystalline fibers of LuAG grown by the micro-pulling down technique will be characterized in chapter 6 and tests performed with high energetic particles will be discussed in chapter 7. The last chapter finally summarizes the thesis and provides an outlook to future activities.

The work was performed, in the frame of the Crystal Clear Collaboration [28], both at the European Organization for Nuclear Research (CERN) in the PH-CMX-DS section and at the *Laboratoire de Physico-Chimie des Matériaux Luminescents* (LPCML). This mixed research unit under the responsibility of both the French National Centre for Scientific Research (CNRS) and the University Claude Bernard Lyon 1, recently merged with two others to form the Institute of Light and Matter (ILM, UMR5306).

Chapter 2

Theoretical background

By providing a short review of the physical background, this chapter sets the basis for the good understanding of the next chapters. We will focus on three important aspects of particle detection based on scintillators. First, we will address the physics of particles interaction with matter, then we will present the process of generation of the scintillation light and subsequently the Cherenkov effect.

2.1 Calorimetry

As mentioned in the previous chapter, an incident particle initiates a shower of secondary particles when interacting with the material of a calorimeter. The shower develops and its products generate signal by passing through the sensitive material of the calorimeter. Before describing the shower development, we will first review the different type of interactions involved.

2.1.1 Electron and positron interaction with matter

Impinging electrons and positrons can be deflected from their trajectory by the electric field of the detector atoms. This deceleration of the particle occurs in the Coulomb field of the nucleus and results in the emission of an electromagnetic radiation. The radiation losses due to this effect, the so-called *bremsstrahlung*, can be expressed in the case of relativistic electrons (E≥1 MeV) as [29]:

$$-\left(\frac{\mathrm{d}E}{\mathrm{d}x}\right)_{\text{brems}} \approx 4\alpha N_a \frac{Z(Z+1)}{A}r_e{}^2 \ln\frac{183}{Z^{1/3}}\ E \tag{2.1}$$

with Z, A the atomic number and atomic weight of the detector medium, and r_e the electron radius. α and N_a are the fine-structure and Avogadro constants respectively.

We can define a radiation length X_0 as:

$$X_0 = \frac{A}{4\alpha N_a Z(Z+1)r_e{}^2\ \ln\left(183\ Z^{-1/3}\right)} \approx 180\frac{A}{Z^2} \tag{2.2}$$

Equation (2.1) then rewrites into :

$$-\left(\frac{\mathrm{d}E}{\mathrm{d}x}\right)_{\text{brems}} \approx \frac{E}{X_0} \tag{2.3}$$

These radiation losses thus increase linearly with the particle energy and the energy deposition follows an exponential law.

When passing through matter, electrons and positrons can also lose energy by *excitation* and *ionization* of bound electrons. In the second process, incident particles transfer enough energy to the atomic electrons to free them from the atom. The soft (less energetic) electrons/photons produced are used in detectors for signal generation.

The mean ionisation losses (also called collision losses) for a charged particle is given by the Bethe-Bloch formula, which can be written for electrons as:

$$-\left(\frac{\mathrm{d}E}{\mathrm{d}x}\right)_{ion} = K\frac{z^2}{\beta^2}\frac{Z}{A}\left[\ln\left(\frac{2m_e c^2 \beta^2 \gamma^2}{I}\right) - \beta^2 - \frac{\delta}{2}\right] \tag{2.4}$$

with $K = 4\pi N_a r_e^2 m_e c^2 \approx 0.307 MeV g^{-1}cm^2$, $\beta = v/c$, $\gamma = 1/\sqrt{1-v^2}$, δ a correction factor taking into account charge density, m_e the electron mass, I and z the mean excitation energy and the charge number of the detector atoms.

From formula (2.4), we see that three regimes can be distinguished. For non-relativistic particles, the energy losses through ionization are dominated by the $1/\beta^2$ term. At low energy, the particle stays longer in the neighborhood of the electrons of the detector atoms and therefore transfer more energy to them. Increasing the energy reduces this energy transfer until a plateau is reached. In this region ($\beta\gamma \sim 3 - 3.5$), the losses become constant, regardless of the particle type. Particles with energy in this range are called *minimum ionizing particles* (MIPs). Then, at high (and very high) energies ($\beta \approx 1$), the logarithmic term in $\beta\gamma$ yields a slow rise of the ionization losses (relativistic rise due to the expansion of the electric fields).

Other sources of energy losses, such as Møller and Bhabha scattering and positron annihilation do not contribute significantly to the total particle energy loss [30]. The relative weight of the Bremsstrahlung and ionization contributions depends on the particle energy. This is illustrated in Figure 2.1 for electrons interacting with Lutetium Aluminium Garnet (LuAG). This material, which has been selected for the concept of meta-crystals for dual-readout calorimetry, has a radiation length X_0 of about 1.41 cm. On the graph, instead of showing the energy loss of the particle, the stopping power of the detector is displayed. It is indeed more common to refer to the energy absorbed (or deposited) in the detector. The *stopping power* for electrons is defined by:

$$\frac{\mathrm{d}E}{\mathrm{d}x} = -\left(\frac{\mathrm{d}E}{\mathrm{d}x}\right)_{brems} - \left(\frac{\mathrm{d}E}{\mathrm{d}x}\right)_{ion} \tag{2.5}$$

From the graph, we can observe that the ionization process is predominant at low energies whereas losses through bremsstrahlung are more important at high energies. The separation between both regions is given by the *critical energy E_c*. This energy is often defined as the energy where both ionization and bremsstrahlung contributions are equal. One can estimate its value with [32]:

$$E_c \approx \frac{800}{Z + 1.2} \tag{2.6}$$
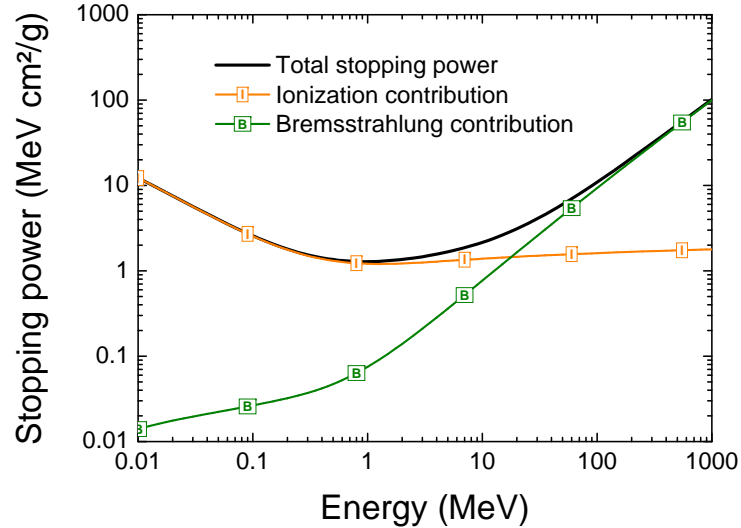
Figure 2.1: Linear stopping power of LuAG (Lu$_3$Al$_5$0$_{12}$) for impinging electrons as computed from [31].

The critical energy of LuAG lies around 12.5 MeV.

2.1.2 Photon interaction with matter

The interaction of photons with matter are based on displacement or production of electrons and holes in the vicinity of detector atoms. Three types of interactions exist and their relative importance depends on the photon energy.

The first type of interaction is the so-called *photoelectric effect.* In this process (see Figure 2.2 for a sketch of each interaction), an electron from the detector atom is freed upon absorption of the photon:

$$\gamma + atom \rightarrow e^- + atom^* \tag{2.7}$$

This effect is dominant at low energies (E$\lesssim$ 100 keV) where the total absorption of the photon is favored. The probability for a photoelectric interaction to occur, also called photoelectric cross-section (σ_{pe}), can be estimated for photon

of energies much larger than the binding energy by:

$$\sigma_{pe} \sim \frac{Z^4}{E} \tag{2.8}$$

Photoelectric effect is thus favored in dense material. To obtain the complete attenuation curve due to the photoelectric effect, absorption edges have to be taken into account, as depicted in Figure 2.3.
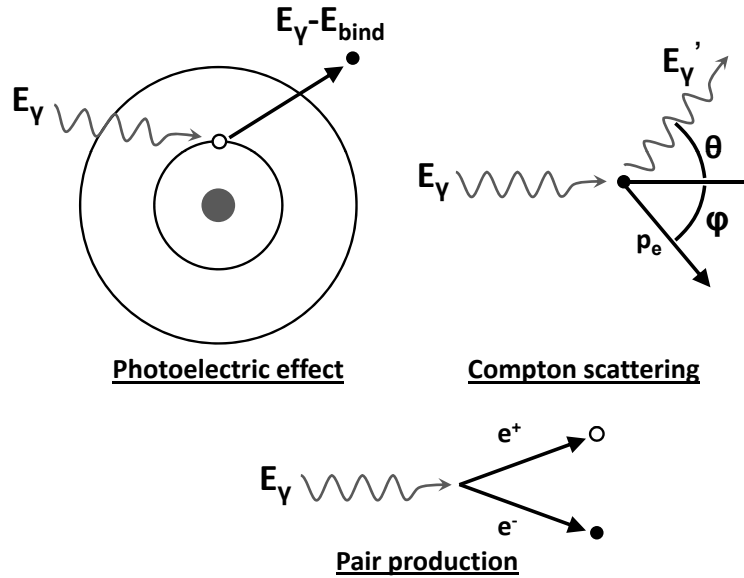
Figure 2.2: The three types of photon interactions with matter.

The second type of interaction is called *Compton scattering*. The incoming photon is inelastically scattered on an electron of the detector atoms:

$$\gamma + atom \rightarrow (\gamma)' + e^- + atom^* \tag{2.9}$$

On the contrary to the photoelectric effect, this only concerns quasi-free electrons. Although the photon only transfers part of it energy, this energy is enough to free the electron (so-called *Compton electron*) from its shell. The photon leaves the vicinity of this atom with a different angle and a lowered energy. Further interactions of this photon with the detector are possible.

At high energies, the Compton cross-section is given by:

$$\sigma_{cpt} \sim \frac{\ln{(\epsilon)}}{\epsilon} \qquad \text{with } \epsilon = \frac{E}{m_e c^2} \tag{2.10}$$

It is noteworthy that both types of excitation leave holes in the core shells of the detector atoms (see equation 2.7 and 2.9) . The de-excitation of these atoms leads to the generation of additional soft photons/electrons (through X-ray fluorescence and Auger effect) when electrons from other shells are filling these gaps.

Finally, in the electromagnetic field of the detector atoms, if their energy exceeds $2m_e c^2 = 1.02$ MeV, the impinging photons can also be converted into an electron-positron pair. The cross-section of the *pair production* is given at low energies (thus low screening) by:

$$\sigma_{pair} = 4\alpha r_e^2 Z^2 \left(\frac{7}{9} \ln 2\epsilon - \frac{109}{54} \right) \tag{2.11}$$

At high energies, the screening is complete and therefore σ_{pair} gets constant:

$$\sigma_{pair} = 4\alpha r_e^2 Z^2 \left(\frac{7}{9} \ln \frac{183}{Z^{-1/3}} - \frac{1}{54} \right) \approx \frac{7}{9} \frac{A}{N_A} \frac{1}{X_0} \tag{2.12}$$

The pair production is not favored at low energies with respect to photo-electric absorption and Compton scattering ($\ln(E)$ versus $1/E$) but it becomes predominant at high energies (E$\gtrsim$ 10 MeV). The detailed repartition of the three types of interactions as a function of the photon energy is provided for LuAG in Figure 2.3. Instead of plotting the respective cross-sections, the mass attenuation coefficient is provided. It is defined as:

$$\frac{\mu}{\rho} = \frac{N_A}{A} \sigma_{tot} \cong \frac{N_A}{A} \left(\sigma_{pe} + \sigma_{cpt} + \sigma_{pair} \right) \tag{2.13}$$

From the graph, we see that the maximal penetration of the photons is achieved in the energy region dominated by Compton scattering (between 3 and 10 MeV). In this region, attenuation lengths around 4 centimetres are observed for LuAG. At lower energy, the photons only penetrate a few micrometers of

matter before being absorbed and converted into photoelectrons. Above 10 GeV, photon attenuation lengths tend to a constant value around 2 centimetres.
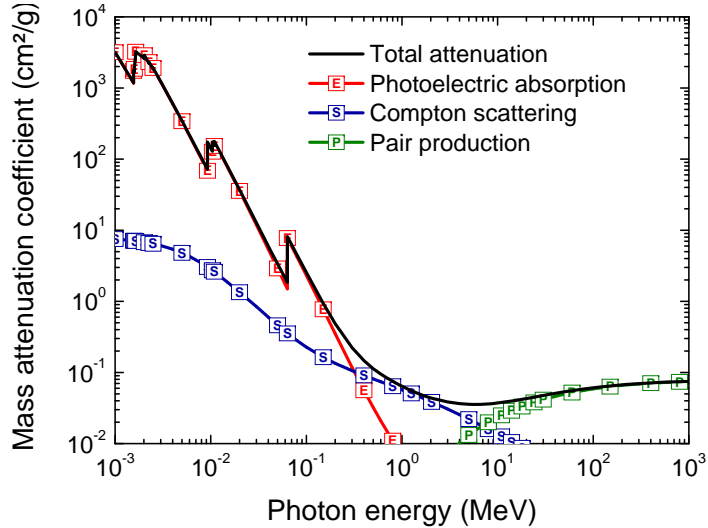
Figure 2.3: Mass attenuation coefficient in LuAG ($Lu_3Al_5O_{12}$) as a function of photon energy as computed from [33].

For high energies (where pair production is dominating), we can define the mean free path λ_{pair} before conversion of the photon. Interestingly, this value is linked to the bremsstrahlung radiation length X_0 (defined in equation 2.2):

$$\lambda_{pair} = \frac{A}{N_A \sigma_{pair}} \approx \frac{9}{7} X_0 \tag{2.14}$$

This relation shows that photons penetrate slightly further in matter as compared to electrons/positrons. Besides it also indicates that X_0 is a meaningful choice of unit for characterizing the electromagnetic shower containment in a calorimeter.

2.1.3 Electromagnetic showers

Electromagnetic showers are initiated by high energy electrons, positrons and photons. The high energy electrons and positrons generate high energy photons through bremsstrahlung. These high energy photons then either undergo materialization via the pair production process or produce Compton electrons. These additional electrons and positrons then radiate new photons which again undergo pair production or Compton scattering. This phenomenon, often referred to as a multiplicative shower or cascade shower, continues until the energy of the secondary particles reaches the critical energy. Then the final stage of the multiplication process takes place: the soft photons interact via the photoelectric process and the soft electrons, including the photoelectric electrons, dissipate their energy through collisions. At this stage, the energy has been transferred to the material and the active layer ensures the conversion into a readable signal.
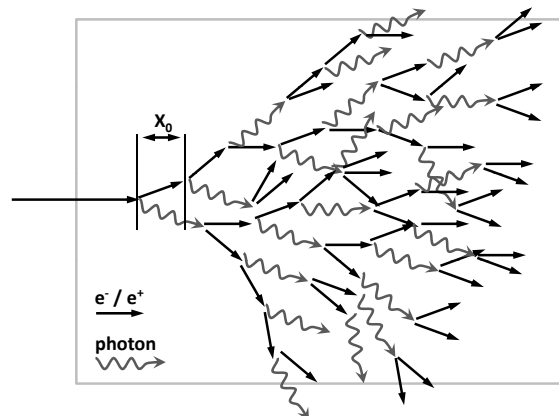
Figure 2.4: Sketch representing the development of an electromagnetic shower.

The shower development is a pure statistical process that can only be efficiently modelled with Monte-Carlo simulations. Nevertheless, a simple model can be considered to describe the average development of the shower:

While $E > E_c$, every X_0:

– an electron loses $E/2$ and generates a new photon via bremsstrahlung,
– a photon generates an electron/hole pair.

When $E < E_c$, electrons lose all their energy through ionization.

Example For a photon of energy E_0:

– At X_0, there is (e^-e^+) with $E_0/2$ each
– At $2X_0$, there is $(e^-\gamma)$ and $(e^+\gamma)$ with $E_0/4$ each
– At $3X_0$, there is $(e^-\gamma)$, (e^-e^+), (e^-e^+) and $(e^+\gamma)$ with $E_0/8$ each
– ...
– At tX_0, there are $N(t) = 2^t$ particles with $E(t) = E_0/2^t$ each.

The shower ends when $E(t) = E_c$, which means:

$$t_{max}\,[X_0] = \frac{\ln\left(\frac{E_0}{E_c}\right)}{\ln 2} \tag{2.15}$$

A more advanced model show that the longitudinal development of the shower follows actually a Γ-distribution [30]. The maximum of the distribution t_{max} and the 95% containment of the shower $L_{EM}(95\%)$ are expressed as:

$$t_{max} = \ln\left(E/E_c\right) + t_0 \quad with \quad t_0 \;=\; -0.5 \text{ for } e^-$$
$$+0.5 \text{ for } \gamma$$
$$L_{EM}(95\%) = X_0\left(t_{max} + 0.08Z + 9.6\right) \tag{2.16}$$

Due to multiple scattering of electrons by the electric field of the nuclei, the shower develops also in the transverse direction. In general, 90% of an electromagnetic shower energy is contained within the so-called Molière radius R_M:

$$R_M = X_0\frac{E_s}{E_c} \quad with \quad Es = \sqrt{\frac{4\pi}{c}}\left(m_ec^2\right) = 21.2\text{MeV}. \tag{2.17}$$

For instance, when a 1 TeV electron enters in LuAG, the maximum of the distribution is achieved after 15 cm but 35 cm are needed to contain 95% of the em shower. Along the development of the shower, most of secondary particles deviated laterally from the shower axis by less than 2.4 cm.

2.1.4 Hadronic showers

Contrary to electromagnetic particles, hadrons interact with nucleons of the detector nuclei through inelastic collisions. This results in the production of a wide spectrum of secondary particles which in turn undergo a variety of interactions. The most abundant are the lightest particles: π^+s, π^-s and π^0s [34]. The last type of pions, which account for about 30%, decay into photons and therefore create electromagnetic showers. Part of the hadronic shower detection is therefore based on the same mechanism than those described in previous section. The secondary particles that do not interact electromagnetically undergo strong interactions that involve, among others, nucleus excitation, nuclear fission and production of hadrons. These processes do not unfortunately all yield detectable signals. Ionizing particles (40-60 % of the shower), such as spallation protons, α particles and nuclear fragments yield ionization tracks in the detector but neutrons, which account to about 15%, are more difficult to measure. Another part (around 30%) of the energy deposition is also invisible to the detector: the binding energy of nuclear break-up and recoil fragments. These three possible mechanisms of interaction do not generate the same detector signal and are therefore creating large fluctuations in the hadronic response.
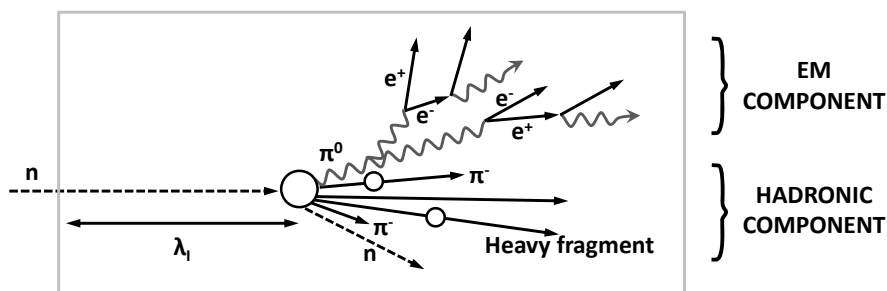
Figure 2.5: Sketch representing the development of a hadronic shower produced by a high energetic neutron.

Hadronic showers are characterized by a particle multiplicity that rises logarithmically with the incident particle energy. Similarly to electromagnetic showers, it is possible to define a characteristic interaction length λ_I which governs the longitudinal development of hadronic showers. The length is actually related

to the mean distance that separates two consecutive nuclear interactions. It can be expressed as:

$$\lambda_I \left[\text{ g cm}^{-2} \right] = \frac{A}{N_A \rho \sigma_{inel}} \text{cm} \approx 35 A^{1/3} \tag{2.18}$$

where σ_{inel} is the cross section of a proton inelastic interaction.

The longitudinal profile of the energy deposition of a hadronic shower can be parametrized by a convolution of a Γ-function (as in em showers) and a descending exponential (accounting for the purely hadronic component) [35]. From experimental data, the position t_{max} where the shower distribution is maximal and the position $L_{EM}(95\%)$ insuring 95% shower containment can be approximated by:

$$
\begin{aligned}
t_{max} \left[\text{in } \lambda_I \right] &= 0.2 \ln \left(E/E_0 \right) + 0.7 \quad with \quad E_0 = 1 \text{ GeV} \\
L_{EM}(95\%) &= \lambda_I \left(t_{max} + 2.5 \lambda_I E^{0.13} \right)
\end{aligned}
\tag{2.19}
$$

For LuAG, for instance, $\lambda_I \approx 16.5 X_0$: 95% of the hadronic shower is thus deposited after 192 cm. This value is thus 5.3 times higher as compared to em showers.

The e/h ratio mentioned earlier (section 1.4), which is the calorimeter parameter quantifying the differences in detection between em and non-em showers, does not depend on energy and is determined by its operation principle and its construction. It can be derived indirectly by the ratio e/π of the signal of an incident electron to the signal produced by the shower of an incident charged pion of same energy. The relation between the two ratios is given by:

$$\frac{e}{\pi}(E) = \frac{e/h}{1 + (e/h - 1) fem(E)} \tag{2.20}$$

where fem is defined as the average fraction of energy which contributes to the electromagnetic component of a hadron shower. This function has been studied theoretically and can be approximated by the expressions [9]:

$$fem(E) = 1 - \left(\frac{E}{E_0}\right)^{m-1} \qquad \text{or also} \qquad fem(E) = k \ln\left(\frac{E}{E_0}\right) \qquad (2.21)$$

where E_0, m, k are free parameters in the range E_0: 0.7-1 GeV, m: 0.8-0.9, k: 0.1-0.15.

2.1.5 Energy resolution of calorimeters

Energy resolution for em calorimeters Several factors have to be taken into account when estimating the resolution of electromagnetic calorimeters. The first one is intrinsic to the detector and is determined by the statistical fluctuations of the deposited energy and its conversion into the detectable signals. Another contribution is governed by the statistical fluctuation in collection of the photons (photostatistics). Finally, if a sampling calorimeter is considered, sampling fluctuations add to the two first ones. These three factors scale at high energies as $E^{-1/2}$:

$$\left(\frac{\sigma(E)}{E}\right)_{EM} \approx \frac{1}{\sqrt{E(\text{GeV})}} \left[\underbrace{0.7\%}_{intrinsic} \oplus \underbrace{\frac{1}{\sqrt{n_{pe}}}}_{photostatistics} \oplus \underbrace{15\%\sqrt{\frac{d}{X_0}}}_{sampling} \right] \qquad (2.22)$$

where n_{pe} is the number of photo-electrons and d is the absorber thickness. In addition, leakage energy further degrades the energy resolution:

$$\left(\frac{\sigma(E)}{E}\right)_{leakage} \approx (1 + 4f_L) \left(\frac{\sigma(E)}{E}\right)_{f_L=0} \qquad (2.23)$$

where f_L is fraction of energy escaping the calorimeter without detection.

Energy resolution for hadron calorimeters Equations 2.22 and 2.23 are also valid for hadron calorimeters, the intrinsic and sampling factors are however larger: they are roughly of 45% and 35% respectively (instead of 0.7% and 15%). The intrinsic contribution is much more important because of the invisible fraction (neutrons and nuclear break-up and recoil) of the energy that is dominated by large fluctuations. The sampling contribution is also larger because hadrons interaction lengths are longer, they are therefore more affected by the sampling structure. Unfortunately this contribution can rarely be neglected (on the contrary to em calorimeters) since hadron calorimeter designs usually favor sampling to reduce the cost and obtain a compact size.

In addition, hadron calorimeters also have a constant term in the energy resolution originating from the dependence of the detector response on the type of particle being measured:

$$\left(\frac{\sigma(E)}{E} \right)_{e/h \neq 1} \sim \left| \frac{e}{h} - 1 \right| \tag{2.24}$$

This contribution adds around 20% of fluctuations [30] to the terms scaling with $E^{-1/2}$. The advantage of compensating calorimeters is precisely to cancel out this contribution. This type of calorimeter is therefore of highest interest at high energies, where the constant term is dominating the other contributions.

In the majority of calorimeters, the observed signal in limited by the energy deposited by the shower particles in the sensitive material. This process is often referred as the dE/dx technique. Calorimeters based on scintillating materials (mechanisms discussed in the next section) uses this technique for instance. In section 2.3, we will present the Cherenkov effect which can also be used in calorimetry. Cherenkov-based calorimeters also use light as detecting signal but the principle of operation is differs from the dE/dx technique.

2.2 Process of scintillation

Regardless of the type of interaction involved, the mechanism which ends the shower development is based on collision loses. The secondary electrons generated in the last stage of the shower lose their energy through inelastic scattering with electrons from the detector matrix until their energy falls below the ionization threshold (twice the band gap). The shower process thus ends with a significant number of electrons in the lower part of the conduction band (see Figure 2.6).
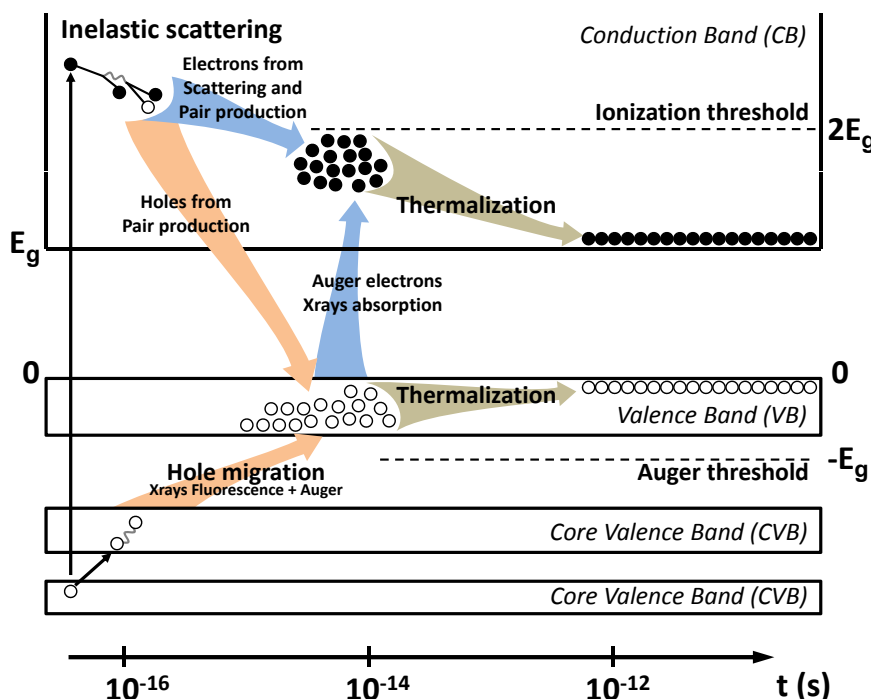
Figure 2.6: Electrons and holes generation and migration during the shower development.

Moreover, during the cascade process, most of the electrons freed from the atoms (through photoelectric and Compton effect or ionization) leave holes in the core shells of the detector atoms. These atoms then de-excite when electrons from the upper shells are filling the gaps in the core shells. This results in a hole migration towards the valence band. It is noteworthy that this hole migration is accompanied by the generation of X-ray fluorescence and Auger electrons.

The final step that ends this chain of events initiated by the impinging particle and thereby brings the crystal matrix back to equilibrium is the recombination of these electrons and holes. To make this possible, the electrons and holes first respectively migrate to the bottom of the conduction band and top of the valence band. This is achieved, in the case of an ordered material like a crystal, by a coupling of the electrons/holes to the lattice vibration modes and emission of phonons. After this electrons and holes thermalization, the recombination can start. This process consists in an energy transition with emission of either photons (radiative recombination) or phonons (non-radiative recombination, energy dissipation through heat). While bolometers measure the energy of the latter ones, scintillating calorimeters are sensitive to the photons. Higher energies will lead to a larger number of secondary particles, which in turn will lead to a larger number of recombination and thus yield more light. The different ways for an electron from the bottom of the conduction to recombine radiatively with a hole from the top of the valence band are illustrated in Figure 2.7. To complete this picture, the trapping of the charge carriers should be mentioned, these will be described in section 2.2.5.
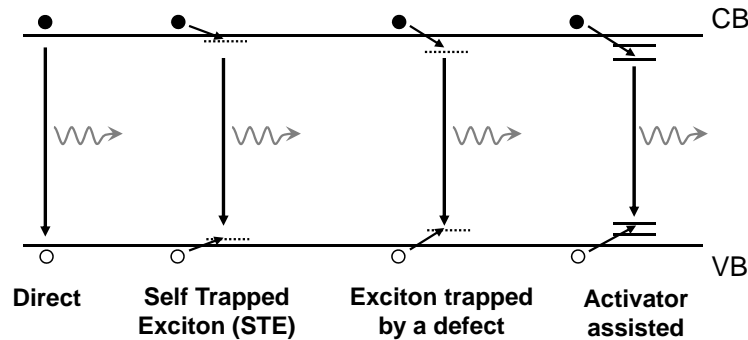
Figure 2.7: Sketch representing the different electron-hole recombinations: direct, based on a self-trapping of the exciton (STE), based on a trapping of the exciton in the vicinity of a defect and assisted with an activator (doping center).

2.2.1 Direct recombination

The simplest recombination process is obtained, among others, in semiconductors with direct bandgap. For them, we have:

$$e + h \quad \Rightarrow \quad h\nu \tag{2.25}$$

The process of recombination is more favorable when the energy of the electrons and the holes have sufficiently decreased. At this point, they usually bind together to form an exciton, which in turn can recombine radiatively:

$$e + h \quad \Rightarrow \quad ex \quad \Rightarrow \quad h\nu \tag{2.26}$$

The radiative recombination can occur either through self-trapping of the exciton (STEs) or trapping of the exciton in the vicinity of a structural defect of the matrix (mainly V_k centers). These two trappings are usually favored, as compared to a direct recombination, since they lower the exciton energy.

2.2.2 Dopant luminescence

A large part of scintillators are so-called extrinsic. This means that the crystal matrix does not intrinsically present (sufficient) scintillating properties. Radiative recombinations can however be favored with doping elements that will act as luminescent centers. These activators are most frequently rare earth ions because of the parity and spin-allowed transition $4f^{n-1}5d \rightarrow 4f^n$. Moreover, for most scintillators, the ground state $4f$ and the lowest of the excited levels $5d$ lie in the band gap. Recombination through this doping centers are therefore favored from the point of the view of the energy. The mechanisms of extrinsic scintillation are:

$$
\begin{aligned}
A + e^- + h^+ &\quad \Rightarrow \quad A + ex \quad \Rightarrow A^* \Rightarrow A + h\nu \\
A + e^- + h^+ &\quad \Rightarrow \quad A^+ + e^- \Rightarrow A^* \Rightarrow A + h\nu \\
A + e^- + h^+ &\quad \Rightarrow \quad A^- + h^+ \Rightarrow A^* \Rightarrow A + h\nu
\end{aligned}
\tag{2.27}
$$
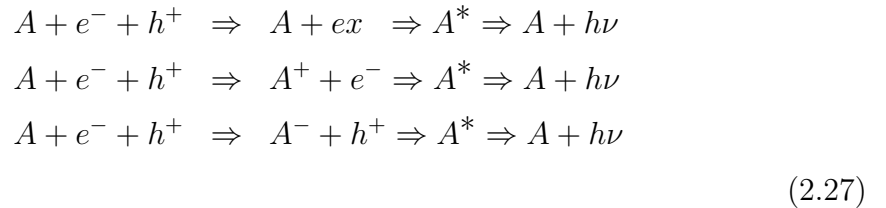
The first mechanism is based on the exciton quenching by the activator leading to an energy transfer. This supposes the energy of the electron and the hole to be low enough to form an exciton. In most frequent situations, because of the very different mobility of the charge carries (around $10^{-3}\text{cm}^2\text{s}^{-1}$ for electrons and around $10^{-4}\text{cm}^2\text{s}^{-1}$ for holes [36]), the mechanism is a two step process: one of the charge carrier de-excite by ionizing the activator and subsequently the other carrier de-excites (second and third mechanism).

Lutetium Aluminum garnets, for instance display much more efficiency when Cerium (Ce) ions are inserted in the matrix. Ce is the rare earth element with second lowest atomic number, its electron configuration is $|Xe|4f^15d^16s^2$. Depending on the crystal growth conditions, Ce can either be tri- or tetravalent. While Ce^{4+} recombination are non-radiative, Ce^{3+} doping leads to fast and intense scintillation.

The transition favored is $4f^05d^1 \rightarrow 4f^15d^0$. In LuAG, both the ground state $4f^1$ and the $5d$ orbitals are split into two spin-orbit components. The difference in energy E_A between the d and f configurations of Ce^{3+} depends strongly on the host material. For LuAG this value lies around 2.3 eV, the energy of the excited state of the activator is thus significantly lower than the band gap of the host material (around 8.3 eV [37]). This is an advantage because the quenching of the Ce^{3+}-luminescence is not favored (excited levels do not fall into the conduction band). Besides, fulfilling $E_A \leq E_g$ ensures a good extraction of the scintillating photons (the crystal matrix is almost transparent at this wavelength).

2.2.3 Charge-transfer luminescence

Charge-transfer luminescence has been observed for instance on Yb^{3+} containing compounds [38]. In Yttrium Aluminium garnets doped with Ytterbium (YAG:Yb), the scintillation process involves both di- and trivalent Yb ions. Charge carriers de-excite through Yb^{2+} but instead of recombining in the vicinity of this atom, they are transfered to Yb^{3+} ions where the recombination occurs. In such a process, where initial and final states are different, selection rules for transitions are loosened, thereby enhancing transition probability.

2.2.4   Cross luminescence

In previously described mechanisms, the photon emission occurs during a transition between the conduction band and the valence band. This transition is usually favored since, for most scintillators, all core bands are below the Auger process threshold ($=CB$-$2E_g$) and therefore holes can migrate to the valence band and subsequently recombine with the electrons that reached the bottom of the conduction band.

Other crystals, like BaF_2 for instance, have their uppermost core band above the Auger threshold (see Figure 2.8). For this reason, the holes left in this band upon excitation cannot migrate through Auger effect. They can however be filled by electrons from the valence band since the energy separating these bands is rather low. In most of the cases, this recombination is radiative. This type of luminescence is called cross luminescence since the recombination of the primary hole is not done with the electron ejected in the conduction band. Actually, contrary to the fast recombination VB to CVB, the recombination of this primary electron is done through a much slower mechanism. A two component emission is therefore observed for BaF_2 (a very fast emission and a significantly slower one).
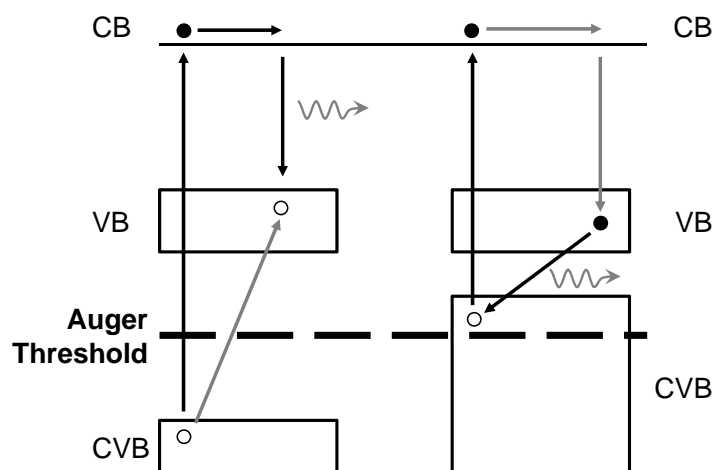
Figure 2.8: Direct luminescence (left) versus cross-luminescence (right).

2.2.5 Signal losses in scintillator-based calorimeters

One source of signal loss in scintillator-based calorimeters was already mentioned earlier: non-radiative recombinations. These recombination always compete with those yielding scintillation light. While the choice of the growth technique and the band gap engineering can make non-radiative recombinations less probable, they cannot in general be completely excluded. Another type of energy loss occurs upon thermalization of the charge carriers.

Charge carrier trapping Luminescent centers such as Ce^{3+} are efficient hole traps but since the recombination occurs through these centers the trapping actually favors the recombination. There are however other sources for electron or holes trapping: structural defects in the crystal matrix. In LuAG for instance, the antisite defects induced by the substitution of a Lutetium with an Aluminium atom in the lattice forms a very efficient electron trap [39]. This electron trapping then competes with the Ce^{3+} centers and their respective concentration in the lattice will determine which effect is dominant.
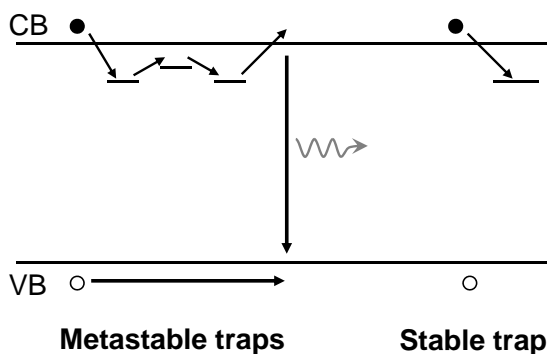
Figure 2.9: Metastables and stable electron traps.

In general, two types of traps can be distinguished: metastable and stable traps (see Figure 2.9). While stable ones will trap the charge carries for a long period, meta-stables traps will only delay the signal restitution. Actually in calorimetry, stables are not inducing too much signal loss. Only the first particles will be detected less efficiently. Once these traps filled (after a certain irra-

diation), they do not longer play any role. On the contrary, meta-stables traps can significantly alter the signal collection. If the lifetime of the trap is slightly longer than the acquisition time, the trap emptying might indeed contribute to a different signal collection triggered on a distinct particle.

The charge carrier escape from the trap is temperature dependent. Thermal energy will indeed allow the charge carrier to reach again the conduction band and subsequently recombine radiatively. Thermally stimulated luminescence (TSL) is an efficient investigation tool for the study of traps. This technique is described and applied on several LuAG samples, as described in Chapter 4).

Thermal quenching   A configurational coordinate diagram (see Figure 2.10) is a way to model the conditions for luminescence of a centre. Such a diagram displays the energy levels as a function of the mean inter-atomic distance (Q).
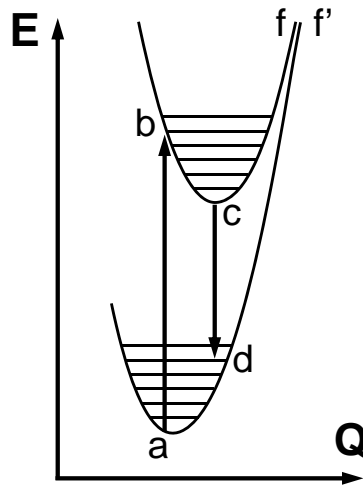
Figure 2.10: Configurational coordinate diagram of a luminescence centre.

In general, the luminescence centre is brought from its ground state to an excited state ($a \rightarrow b$) upon excitation. The state c is then reached with energy dissipation through phonons. Once in c, the luminescent center can de-excite radiatively ($c \rightarrow d$) but it can also transit at higher energies if the energy curves intersect or approach each other. This transition (through f and f') is called

thermal quenching and results in a non-radiative recombination. It therefore competes with the emission process and is responsible for an extra signal loss.

Concentration quenching When the concentration of activator is increased in the crystal matrix, more and more interactions in between these luminescent centers become possible. The excitation energy can therefore travel over a long distance in the solid [40]. Increasing this distance results in a high probability for the charge carriers to meet a quenching site where the energy is lost non-radiatively. This phenomenon is called concentration quenching. For most scintillators, it becomes effective at concentrations of few atomic percent. The emitted scintillation is usually faster but less intense.

All these effects add up and as a consequence most scintillators generate much less signal as compared to the energy initially transfer to the material. For illustration, we can compute the ratio of the energy of the generated light to the incoming particle energy for LuAG:Ce. This crystal generates not more than 60 000 photons when excited with a gamma photon of 1 MeV [41]. Since most of the photons are emitted with a wavelength close to 520nm (2.4 eV), this ratio is roughly:

$$\frac{E_{detected}}{E_{particle}} \approx \frac{60000 \times E_{photon}^{emitted}}{E_{particle}} \lesssim 15\% \tag{2.28}$$

Scintillation involves a significant amount of mechanisms (from the shower generation to the relaxation, thermalization, transfer and eventually radiative recombination of the charge carriers). A certain set of parameters can be studied in order to quantify and compare the properties of several types of scintillators. These parameters will be presented in the next chapter for Lutetium Aluminium garnets.

Before closing this chapter, we will briefly describe another important effect that yields a different calorimeter operation principle: the Cherenkov effect.

2.3 Cherenkov effect

Detectors based on scintillation light are sensitive both to hadrons and electromagnetic particles. For some applications (particle identification for instance) it is highly useful to only measure one of them. Among the detectors dedicated to the detection of electromagnetic particles, those based on the Cherenkov effect are receiving a lot of interest. We will first explain the physics of its generation and then we will discuss its advantages in calorimetry.

Although the velocity of particles cannot exceed the velocity of light in vacuum, it is possible to approach this limit, provided the particles have enough energy. On the other hand, the velocity of light in a medium of refractive index $n > 1$ is given by:

$$(v_\phi)_{light} = \frac{c}{n} \tag{2.29}$$

As a consequence, particles can travel faster than the phase speed of light if:

$$\beta = \frac{v}{c} > \frac{1}{n} \tag{2.30}$$

For a particle of a given mass, it is possible to express this threshold in terms of energy. The velocity of a particle and its energy are linked through:

$$E = m_{eff}c^2 = \frac{m_0 c^2}{\sqrt{1 - \frac{v^2}{c^2}}} = \frac{E_{rest}}{\sqrt{1 - \beta^2}} \tag{2.31}$$

where E_{rest} is the energy of the particle at rest. The kinetic energy corresponding to the Cherenkov threshold $(KE)_{che}$ can thus be expressed as:

$$(KE)_{che} = (E - E_{rest})_{che} = E_{rest} \left[\frac{1}{\sqrt{1 - (\beta_{che})^2}} - 1 \right] \tag{2.32}$$

The fact that particles can travel faster than the speed of light becomes of high interest for charged particles. These particles polarize the neighboring atoms

when travelling through matter. In most of the case, this polarization is arranged symmetrically around the particle path and therefore, although each individual atom behaves as an electric dipole, no large scale dipole field is observed [29]. However, at high velocities, above the Cherenkov threshold namely, the particle in motion travels faster than the speed at which it interacts with its environment. The symmetry in the atoms polarization is then broken (see Figure 2.11). The integrated dipole field is no more vanishing and the dipole moment leads to the formation of a wave front (see Figure 2.12). This results in the emission of a characteristic electromagnetic radiation, called Cherenkov radiation.

$$\beta < 1/n \qquad\qquad \beta > 1/n$$
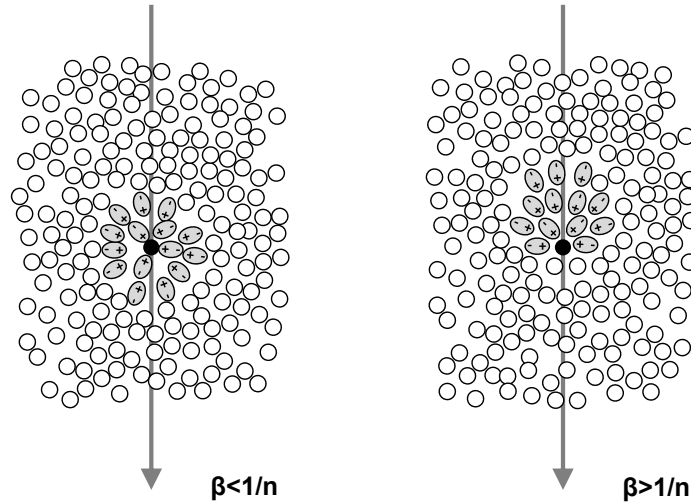
Figure 2.11: Interpretation of the Cherenkov effect [29].

Cherenkov light is emitted in the forward direction at a characteristic angle θ_{che} with respect to the track of the charged particle. It can be computed as follows: during Δt, the particle travels the distance $\Delta t\,\beta c$ whereas the photon moves by $\Delta t\,c/n$ (distances AB and AC respectively on Figure 2.12). The Cherenkov angle is thus obtained by:

$$\cos\left(\theta_{che}\right) = \frac{AC}{AB} = \frac{\Delta t\,c/n}{\Delta t\,\beta c} = \frac{1}{n\beta} \qquad (2.33)$$

41

We observe that the Cherenkov angle increases with the particle velocity and is maximum for relativistic particles ($\beta = 1$).
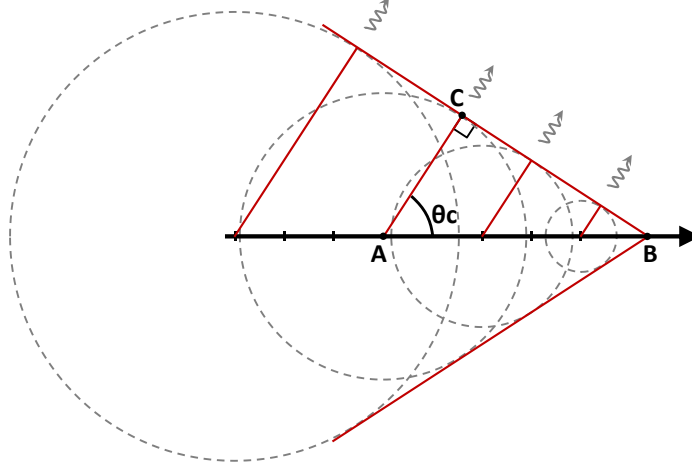
Figure 2.12: Sketch for computation of the Cherenkov angle (with $n = 1.84$)

The number of Cherenkov photons emitted with wavelengths between λ_1 and λ_2 per unit path length is given by:

$$\frac{\mathrm{d}N}{\mathrm{d}x} = 2\pi\alpha z^2 \int_{\lambda_1}^{\lambda_2} \left(1 - \frac{1}{n(\lambda)^2)\beta^2}\right) \frac{\mathrm{d}\lambda}{\lambda^2} \qquad (2.34)$$

The spectrum of emitted Cherenkov photons thus exhibits a $1/\lambda^2$ dependence. As a consequence, most of the Cherenkov photons are emitted in the UV range. Cherenkov photons are not emitted in the X-rays range because in this region the index of refraction is $n = 1$, and therefore the condition for Cherenkov emission cannot be fulfilled [29].

Neglecting the dispersion of the medium ($\mathrm{d}n/\mathrm{d}\lambda = 0$), we obtain:

$$\frac{\mathrm{d}N}{\mathrm{d}x} = 2\pi\alpha z^2 \left(1 - \frac{1}{(n\beta)^2}\right) \left(\frac{1}{\lambda_1} - \frac{1}{\lambda_2}\right) \qquad (2.35)$$

This expression can be rewritten with equation 2.33. For singly charged particles $(z = 1)$, we finally obtain:

$$\frac{\mathrm{d}N}{\mathrm{d}x} \approx 491.3 \; \sin^2(\theta_{che}) \left(\frac{1}{\lambda_1} - \frac{1}{\lambda_2} \right) \tag{2.36}$$

We can now estimate these parameters for Lutetium Aluminum garnets. For this material, the maximum (for $\beta = 1$) Cherenkov angle is equal to:

$$\theta_c = \cos^{-1}\left(\frac{1}{1.84} \right) = 57° \tag{2.37}$$

The number of photons emitted within 180 nm (corresponding to the absorption edge of LuAG) and 800 nm per unit length is:

$$\frac{\mathrm{d}N}{\mathrm{d}x} \approx 1390 \; ph \; cm^{-1} \tag{2.38}$$

In order to estimate the number of Cherenkov photons that can be collected, the photon detection efficiency (PDE) of the photodetector must be taken into account. Most detectors indeed present a poor detection in the UV and NIR. For UV-enhanced silicon photomultipliers (UV-SiPMs), the number of photons detected (PDE estimated from [42]) is:

$$\frac{\mathrm{d}N}{\mathrm{d}x} \approx 182 \; phe \; cm^{-1} \tag{2.39}$$

where *phe* is the number of photons detected. To obtain the correct number of Cherenkov photons, this value has to be multiplied by the track length of the particles above the Cherenkov threshold (not necessarily related to the crystal length).

We can also estimate the Cherenkov energy threshold for LuAG (formula 2.32):

$$E_{che} = \begin{array}{ll} 97.7 \text{ keV} & \text{for } e^- \\ 26.7 \text{ MeV} & \text{for } \pi^- \\ 179.5 \text{ MeV for protons} \end{array} \tag{2.40}$$

This difference in energy thresholds makes Cherenkov light well suited for particle-identification purposes. In hadronic showers, light particles will stay relativistic over a longer path than heavy hadrons. This results in a larger contribution from the electromagnetic particles to the Cherenkov signal. The dual readout method presented by the DREAM collaboration uses this approach to estimate the electromagnetic fraction.

Although the Cherenkov signal is weaker than the scintillation signal, it is characterized by a prompt emission. Therefore, when timing becomes critical, this can be a decisive advantage over scintillation. Scintillation involves indeed many actors in the signal generation and as a consequence, in addition to extra signal losses, the signal is not immediate.

Chapter 3

Properties of Lutetium Aluminium garnets (LuAG)

We mentioned in section 1.4.4 that Lutetium Aluminium garnets (LuAG) are good candidates for dual-readout calorimetry based on a meta-material concept. The properties of these garnets, widely studied in the past ten years, will be presented in this chapter. Although we will show in the next chapter that the choice of the growth technique influences the properties of LuAG, the experimental characterization was based here on samples grown by the vertical Bridgman technique, as described in [43, 44]. They were provided by A.G. Petrosyan from the Institute for Physical Research in Ashtarak, Armenia.

The different characterization techniques will be provided in a first part (sections 3.1 to 3.4). The aim is to provide the experimental background necessary for the second part (section 3.5) where the influence of the doping concentration, as well as the addition of co-doping centers will be discussed.

3.1 Photoluminescence

We have seen earlier that the luminescent centers have an important role to play in the last stage of the particle detection process. These centers are in competition in the electron-hole recombination process. Scintillation light is obtained when the radiative recombination is triggered with impinging energies much higher than

the band gap. This type of luminescence, often referred as radio-luminescence (RL), is based on an energy transfer from the matrix to the luminescent centers. Since they are located within the band gap of the host matrix, these centers can also interact with photons of energies lower than the band gap. This type of luminescence, usually based on UV or visible excitation light, is referred as photo-luminescence (PL).

3.1.1 Energy levels in LuAG

When the energy of the impinging photon is higher than the band gap ($\lambda <$ $150nm$) band-to-band excitation occurs. For photons of lower energies, the host matrix should in principle be transparent. In practice, the onset of transparency is not observed before $\lambda \sim 180$ nm. The absorption observed in the 150-180 nm region (6.9-8.3 eV) has been attributed to the exciton absorption [37]. In cases of strong coupling of electrons or holes to the crystal lattice, a carrier may be self-trapped in its own lattice distortion field [45]. When this carrier gets bound to its antagonist, the resulting electron-hole pair is generally described as a self trapped exciton (STE). In the case of LuAG, the STE has two excited levels that lead to an absorption band peaking at 7.1-7.3 eV [37]. The excited levels lie below the band-gap since the trapping of the exciton decreases its energy. The recombination of this STE is accompanied in the case of LuAG by a characteristic emission spectrum peaking at around 250 nm (4.96 eV). The STE can also be localized around a defect of the matrix. In LuAG the main source of defects are anti-site defects (AD) caused by Lu cations occupying the octahedral sites of Al cations: Lu_{Al}^{3+}. The concentration of these defects in the host matrix can account for up to 0.5 at.% according to [46]. STE localised around AD defects can be excited with lower energies (typically 6.9 eV) and their emission lies between 3 and 5 eV. Both processes are responsible for the *intrinsic* emission of LuAG. But this luminescence does not meet the requirements of the concept of calorimetry studied in the frame of this thesis. The emitted light is indeed predominantly in the UV region (250-400 nm) and, in addition, the recombination mechanisms involved are too slow ($\sim 2\mu$s, see section 3.3) for being used in high energy physics with high repetition rates.

The matrix of LuAG is therefore usually doped with rare earth elements such as Yb, Pr or Ce. The latter is the one that receives special interest for high energy physics. Ce^{3+} luminescence is characterized by an emission band peaking at 520 nm that corresponds to the $5d-4f$ transitions (see Figure 3.1). Pr^{3+} doping is not investigated here because of the poor UV detection efficiency of standard photo-detectors. Recent developments in SiC photodiodes might however change this decision because of their 230-350 nm detection window. Besides, if the operation of these photo-detectors in the avalanche mode is made possible, their excellent radiation hardness gives them a significant advantage.

The different luminescent processes observed in LuAG are summarized in Figure 3.1. The typical excitation and emission energies are also provided.
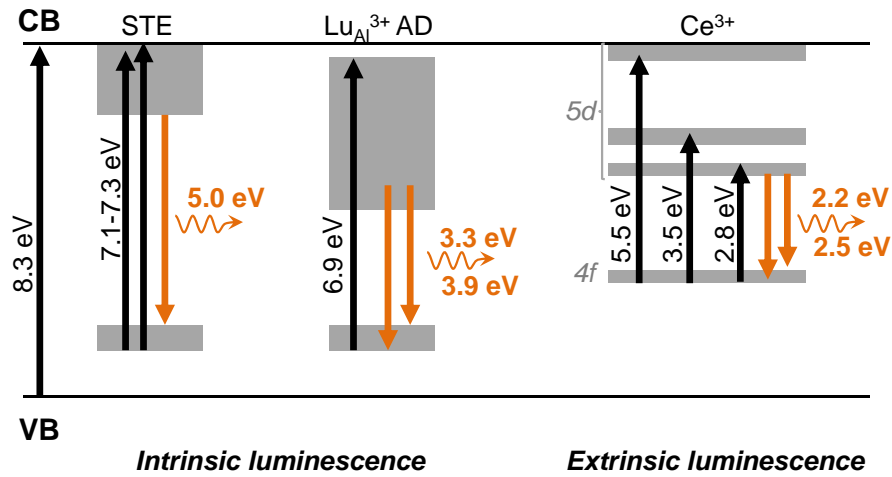
Figure 3.1: Diagram of energy levels for LuAG showing the self trapped exciton *STE* (left), the perturbed STE localized at an antisite defect (middle) and the extrinsic Ce^{3+}-related luminescence (right).

3.1.2 Spectrofluorimetry

The energy levels of a set of LuAG crystals were investigated with a spectrofluorimeter[1]. The working principle of this device is illustrated in Figure 3.2. A light source (typically based on Xenon), is used to generate photons over a spectrum as wide as possible (in our case: $200nm \leq \lambda \leq 800nm$). Two monochromators are used for selecting both the excitation and the emission wavelengths. It is then possible to measure an emission spectrum of a crystal for a selected excitation wavelength. And, reciprocally, it is also possible to get an excitation spectrum when measuring at one particular emission wavelength.
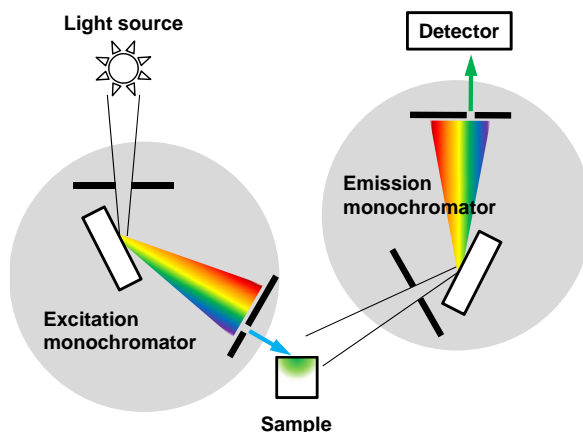
Figure 3.2: Working principle of a spectrofluorimeter.

We started by computing an emission-excitation map of the sample. This mapping can be useful when studying a sample that absorbs and emits on wide spectra of wavelengths. The contour plots for an undoped LuAG and a Cerium doped one are provided in Figure 3.3.

On the undoped sample, we observe a very weak emission of UV light corresponding to the exciton emission. At 200 nm (lower bound of the spectrofluorimeter), only the tail of the excitation band is probed. Wavelengths around 180 nm (unreacheable here) would lead to higher signals. This same region is also distinguishable on the Cerium doped sample but the main features observed are

---

[1]Perkin Elmer LS 55
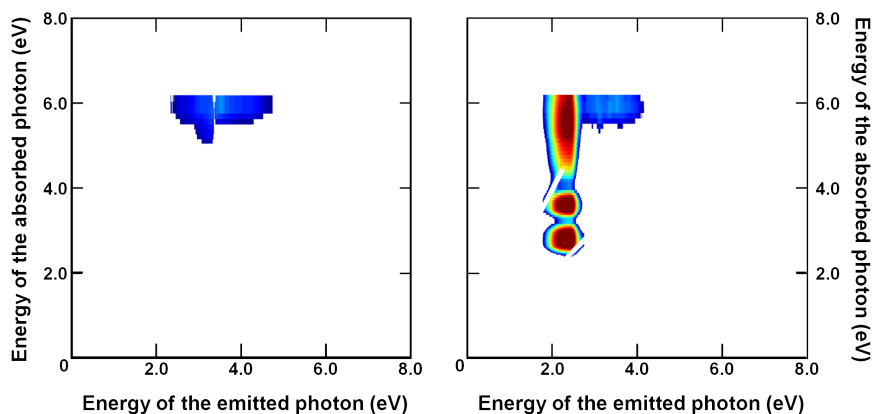
Figure 3.3: Emission versus excitation mapping of undoped (left) and Cerium doped (right) samples of LuAG.

the three absorption bands of Ce^{3+}. These correspond to the transitions from the $4f$ to the $5d$ levels. After the absorption of the incident photon, the recombination of the electron-hole pair is accompanied by a transition from the lowest $5d$ to the two upper levels of $4f$ (only transition that is parity allowed) as described in Figure 3.1. Although only a set of transitions are allowed, rather broad bands are visible. This effect which is due to electron-phonon coupling is emphasized at higher temperatures.

3.1.3 Excitation and emission spectra

In order to have a more quantitative discussion, the emission-excitation maps were integrated over the emission (respectively excitation) regions in order to obtain the excitation (respectively emission) spectra. They are displayed in Figure 3.4.

On the graph, the scale being linear (logarithmic on emission-excitation maps), the UV emission of the Cerium doped LuAG is not visible anymore. As a matter of fact, the relative intensity of the intrinsic emission (200-475 nm) and the Cerium emission (475-700 nm) is an indication of the amount of dopant added to the LuAG matrix. This approach is only possible at low concentrations where non-linear effects are not too important. There are more accurate techniques to estimate this value, one of them will be presented in the next section.
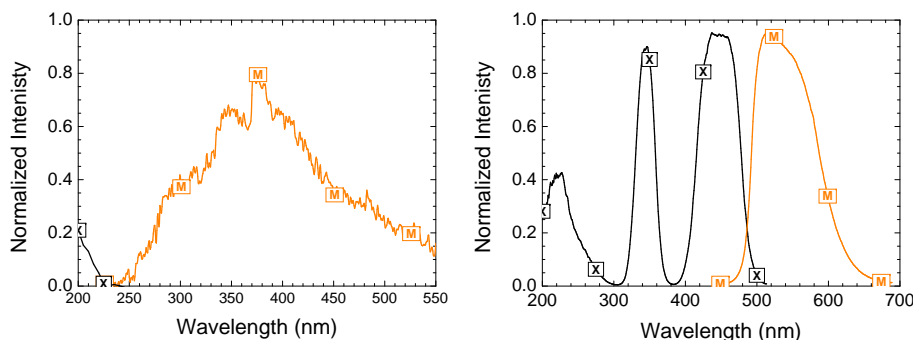
Figure 3.4: Emission (M) and excitation (X) spectra of undoped (left) and Cerium doped (right) samples of LuAG.

It is also important to highlight the fact that the emission spectrum overlaps the excitation band of lowest energy. This will play a role in the propagation of the light: some of the light emitted by the luminescent centers will be reabsorbed by others. This additional absorption, commonly referred as *self-absorption* will result in a shift of the emission spectrum towards the red end for samples with high doping concentrations and/or large dimensions.

3.2 Light transmission

Another aspect of the scintillating crystal characterization is the study of its light transmission. The approach is similar to the one that leads to a the excitation spectra. The important difference in this case is the ability to quantify the amount of light absorbed/transmitted.

3.2.1 Transmission setup

The working principle is illustrated in Figure 3.5. A monochromatic beam is sent on a beam splitter. The non-deviated beam (B_1) is sent through the sample whereas the second beam (B_2) coming out of the splitter does not interact with the sample. Both beams arrive on a photodetector that computes their respective intensities. A beam chopper then cycles through 3 modes: beam (B_1), no beam, beam (B_2). The acquisition window where no beam is sent on the detector allows

computing the noise value (P_0). The computer interface that acquires the signals subsequently computes the ratio $(B_1 - P_0)/(B_2 - P_0)$ which is proportional to the light losses induces by the interaction of the light with the sample. A measurement performed without the sample then provides a normalization factor which sets the value corresponding to 100% transmission.

Transmission measurements were performed with a parallel beam, perpendicular to the sample faces. This condition makes indeed the analysis easier (angle of all photons assumed to be 0°). Experimentally this is achieved by collimating the light rays with UV lenses. Since transmission measurements probe the bulk of the material, it is important to make sure that the beam is sufficiently smaller than the cross section of the sample in order not to interact with the edges. With help of an adequate pinhole, surface effects can then be neglected.
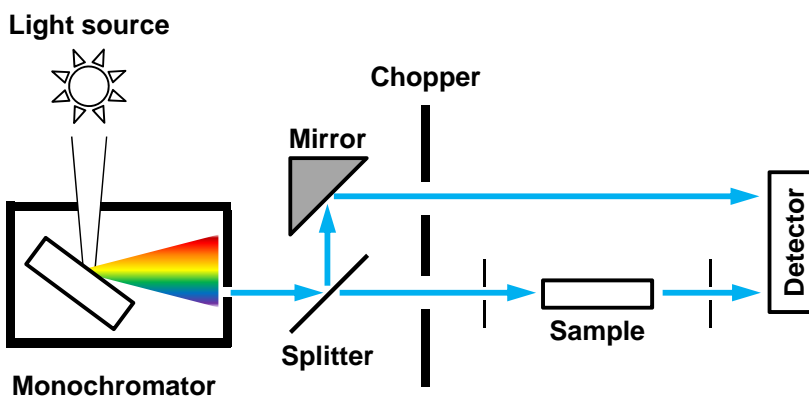
Figure 3.5: Working principle of the transmission bench.

The objective of transmission measurements is to determine the interactions of the photons with the crystal. In general, these interactions will change the direction of the photon (in case of scattering) or generate another photon with a randomized angle (in case of photo-luminescence processes). As a result, by limiting the solid angle of the collected photons, only the photons that are not interacting with the sample are being measured (i.e. the transmitted part of the light). For this purpose, another pinhole is inserted after the exit face of the crystal.

The transmission curves of the samples previously measured in photoluminescence, are provided in Figure 3.6. As expected, the Cerium doped sample shows a drop of the transmission around 345 nm and 450 nm as compared to the undoped sample. It is the region where the incoming photons are absorbed by the Cerium and re-emitted with an angle that only allows a very weak signal collection by the photo-detector. The amplitude of the transmission drop is depending on two factors: the Cerium concentration and the length of material encountered by the photons. This is basically equal to the number of Cerium sites on the path of the photon multiplied by the probability of photon absorption when encountering one site. For this particular example, the doping concentration is rather low (0.1 at.%) and the sample is measured transversally so that the light only interacts with 2 mm of material. Under these conditions, the probability of interaction is not that high. We will see later that increasing both the length and the doping concentration leads to transmission curves with significant drops in the Cerium absorption bands.
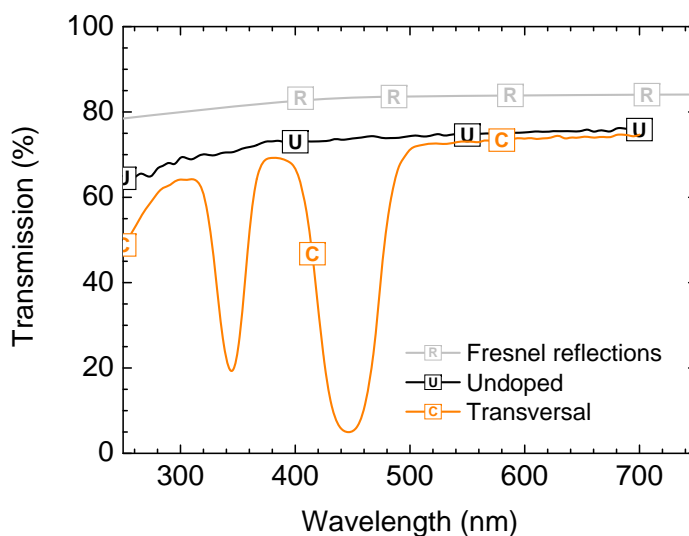
Figure 3.6: Transmission measurement of an undoped (U) and Cerium doped (C) sample of LuAG. Losses due to Fresnel reflections (R) are provided based on [47].

3.2.2   Theoretical transmission

In the case of a perfect crystal that shows no defects in the matrix (no bulk scattering), that does not present any impurities, and has perfectly polished surfaces, the only light losses that have to be considered are the losses due to the bulk absorption and the Fresnel reflections. The latter ones are due to the change in index of refraction at the interface ($n_{LuAG} \approx 1.84$ and $n_{air} \approx 1$). When light is encountering such an interface, only part of it is transmitted, the remaining part is reflected. At an interface between two media (1) and (2), the part of light transmitted and reflected at normal incidence are defined with Fresnel coefficients (t and r respectively):

$$ r = \left(\frac{n_1 - n_2}{n_1 + n_2} \right)^2 \qquad \text{and} \qquad t = 1 - r \qquad (3.1) $$

As a result, at normal incidence, a LuAG - air interface transmits 91.3% of the light. In a transmission measurement, there are two of these interfaces (entry and exit faces) and therefore multiple bouncing can occur as depicted in Figure 3.7. The total light transmitted through the sample is then called the *transmittance*. Along the same line, the part reflected back and the part lost are called the *reflectance* and the *absorptance* respectively.
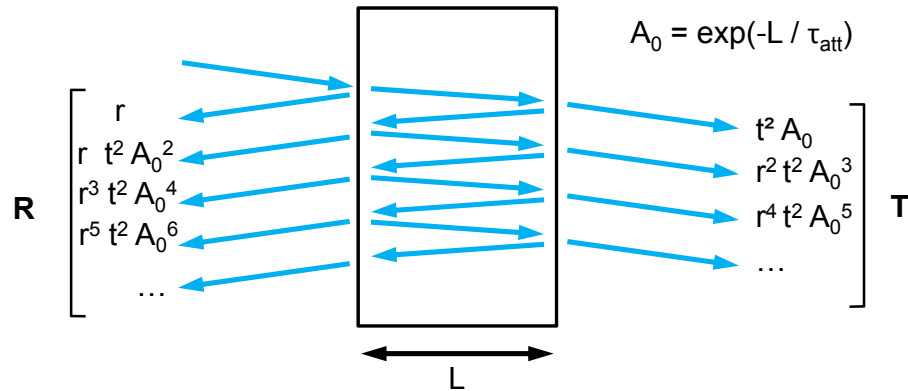
Figure 3.7: Sketch illustrating the contribution to the transmittance (T) and the reflectance (R).

Due to Fresnel reflections, the amount of light crossing the two interfaces directly (T_1) is equal to t^2. If we include the absorption of the material, this can be expressed as:

$$T_1 = t^2 exp(-L/\tau_{att}) = t^2 A_0 \tag{3.2}$$

where L is the length of material crossed by the photons and τ_{att} is the attenuation length of this material. By summing the contribution on the multiple bouncing rays, the transmittance can then be expressed as:

$$T_\infty = \frac{t^2 A_0}{1 - r^2 A_0} = \frac{T_1}{1 - r^2 A_0} \tag{3.3}$$

In practice, even when neglecting material absorption, $T_1 = 99.2\%$ T_∞. Multiple bouncing thus does not modify significantly the value of the total transmittance.

Using equations 3.1 and 3.3, we find a theoretical transmittance for a LuAG crystal of good optical quality ($\tau_{att} >> L$) of 83.3% (with $n_{LuAG} = 1.84$). The value of the index of refraction actually depends on the wavelength. Using values from [47, 48], we obtained the theoretical transmittance as a function of wavelength. This curve is provided in Figure 3.6.

3.2.3 Normalized transmission

Experimentally, we observed a transmission in the red end of the spectra significantly lower than this theoretical value. If only the material absorption is taken into account, an attenuation length of around 1.7 cm is consequently obtained. Given the optical quality of the samples, this value is significantly underestimated. Two reasons can explain this: surface effects and the dimension of the probing beam. In the formula given above, we did not include any surface contribution due to not strictly polished faces. Also the sample probed had lateral dimensions of 2 mm whereas the beam size is estimated to be between 1.7 and 1.8 mm (the value is wavelength dependent). As a result, a perfect alignment of the beam in

the center of the crystal is rather complex and additional transmission/absorption can be measured.

In practice, because of these alignment issues, relative measurements were considered instead. All the crystals being measured in the same configuration, it is possible to normalize transmission curves to the value of their transmission in the red end. This does not allow comparison of their bulk absorption neither an estimation of the Fresnel losses but this provides a convenient comparison of their impurities, either wanted (luminescent centers) or unwanted (non-strictly purity of the raw material for instance). Besides, since the crystals have dimensions of 2x2x8 mm^3, it is possible to measure the transmission through 2 and 8 mm of material. The corresponding curves are shown in Figure 3.8 for both undoped and Cerium doped samples.
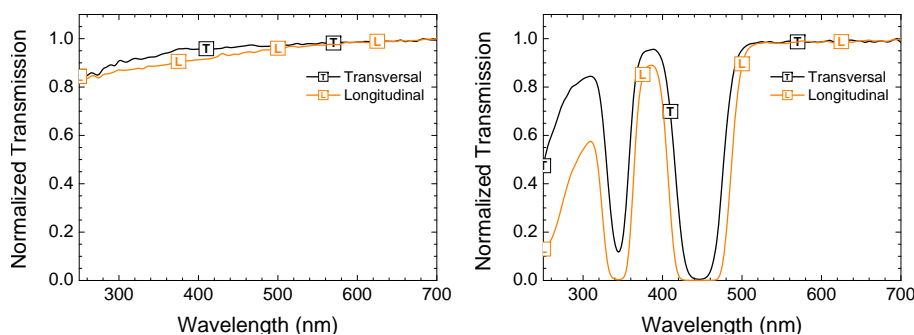
Figure 3.8: Longitudinal (L) and transversal (T) transmission curves of undoped (left) and Cerium doped (right) samples of LuAG.

For the undoped sample no significant changes in transmission are visible when increasing the sample length. On the other hand, as expected, the sample doped with Cerium presents transmission drops in the absorption bands of the Cerium which are more pronounced when the length increases. It is worth noting that computing the ratio of the longitudinal and the transversal transmissions is an indication of the transmission caused by 6 mm of material. More importantly, with this ratio, under the assumption that lateral and longitudinal faces are of equal quality, the Fresnel losses then cancel out.

3.2.4 Cerium absorption

By computing the ratio of the undoped and the Cerium doped curves previously described, we can estimate the light loss induced by the Cerium sites. This is obviously only valid if the host matrix of a Cerium doped sample can be considered as similar to the one of a undoped sample. We will here assume this assumption to be valid. From this ratio, we can then compute the attenuation coefficients α_{att}^{Ce} and attenuations lengths τ_{att}^{Ce} through:

$$\alpha_{att}^{Ce} = -\frac{1}{L} \ln \left(\frac{T_{Cerium}^{norm}}{T_{Undoped}^{norm}} \right) \qquad \text{and} \qquad \tau_{att}^{Ce} = \frac{1}{\alpha_{att}^{Ce}} \tag{3.4}$$

where L is the length of material considered, equal to 6 mm in our case. T_{Cerium}^{norm} and $T_{Undoped}^{norm}$ are the normalized (to the red end) transmissions of Cerium doped and undoped samples respectively. These attenuation coefficients are wavelength dependent, as shown in Figure 3.9.
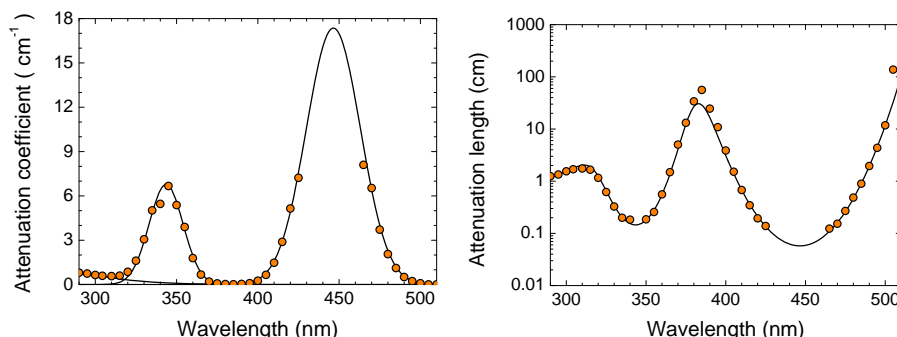
Figure 3.9: Attenuation coefficients (left) and lengths (right) induced by Cerium doping in LuAG as a function of wavelength.

On the attenuation coefficient curve, the points corresponding to the Cerium absorption bands are not visible. These points are not reliable since the transmission measured lies in the experimental error. This error is estimated to be around 1%, as a consequent any value above $\alpha_{lim} = -\ln(0.01)/L \approx 8\ cm^{-1}$ has to be considered as irrelevant. Nevertheless, a Gaussian fit easily recovers the missing part of the curve. These Gaussian fits, which correspond to the Cerium

absorption bands, are also an important indication of the doping concentration. The amplitudes of the Gaussian peaks (at 345 and 450 nm) are indeed directly proportional to the Cerium concentration. By comparison to a reference sample, this is a convenient way to estimate the Cerium concentration of any sample.

The two first techniques presented up to now are useful to characterize the host matrix and the luminescent centers from the point of view of the photons wavelength. No considerations have been taken into account regarding their timing properties. This aspect will be covered in the next section.

3.3   Timing properties

We mentioned in the previous chapter that, given the complexity of the energy conversion mechanisms, the generation of the scintillation light is not prompt. As a matter of fact, the emission of scintillation light can be modelled with help of a combination of an exponential rise and decay [49]:

$$f(t) = A_0 \exp\left(-\frac{t - t_0}{\tau_{decay}}\right)\left(1 - \exp\left(-\frac{t - t_0}{\tau_{rise}}\right)\right) \qquad (3.5)$$

where τ_{rise} and τ_{decay} are the rise and decay constants of the scintillating crystal which respectively model the excitation and de-excitation processes occuring in the crystal. Typically values range from hundreds of picoseconds to a few nanoseconds and tens of nanoseconds to some microseconds, for the rise and decay respectively.

In order to study the time response of the crystal, the energy impinging the material should present some delimitations in time. This has some implications on the amount of light collected. In the previous setup, the excitation light is continuous and it is fairly easy to have enough signal for read-out. On the other hand, when studying the timing properties, the excitation should be as short as possible. At the same time, to maintain an acceptable readout signal, they should be as intense as possible. Therefore lasers are a good choice since they can be operated in a pulsed mode with pulse duration from a few nanoseconds down to a few femtoseconds. The energy can be in the range of the UV-blue (2-7 eV), the

VUV (30-60 eV) or the XUV (400-600 eV) as in [50]. Higher energies (around 20 keV) can also be reached with laser-triggered X-rays tubes as in [51, 52].

The choice of energy is actually not innocent since it determines what mechanisms are involved during the energy conversion and this will have consequences on the time properties measured. For instance, if the energy chosen lies around 5.5 eV, only the Cerium sites will be excited. On the other hand, if the energy is close to band gap 7-8 eV, then both the exciton and Cerium luminescence will be probed. This result in different de-excitation and consequently is very likely to lead to different decay constants. Moreover, these decay values can also be altered by quenching mechanisms when the energy increases. For what concerns the rise time of the scintillator, differences can be observed for energies higher than the band gap. The excitation mechanism is indeed changing when the energy increases. For instance, the thermalization of the electron-hole pairs ($E \gtrsim 10$ keV) and the shower processes ($E \gtrsim 1$ MeV) will play a role. And it is very likely that the rise time further evolves at very high energies.

In the frame of this thesis, a VUV laser was used to investigate the fine details of the time properties of some samples of LuAG grown by different techniques (results discussed in next chapter). However, for the characterization presented in this chapter, another approach was followed. Here only the decay time was considered (less restrictive on the time resolution) and the measurement were based on γ-photons of 662 keV produced by a radioactive source (Cs^{137}). The advantage of a γ source is that the entire energy is contained in one photon. On the other hand, the conversion only leads to a relatively low amount of photons.

3.3.1 Photomultiplier tubes

The detection of the photons was based on a photomultiplier tube (PMT). The working principle of this photodetector is illustrated in Figure 3.10. Such a device has a window (usually made out of quartz for good UV transparency) covered with a photosensitive compound (usually a bialkali such as Sb-K-Cs). When a photon hits this so-called photocathode, an electron is generated through photoelectric effect. This photo-electron is then focused on a set of dynodes (typically 10) with help of an electrode. The geometry of these dynodes, their relative

alignment and the voltage applied in between, is optimized in order to favor electron multiplication. Due to this voltage separating the dynodes, each electron that hits a dynode generates a set of secondary electrons.
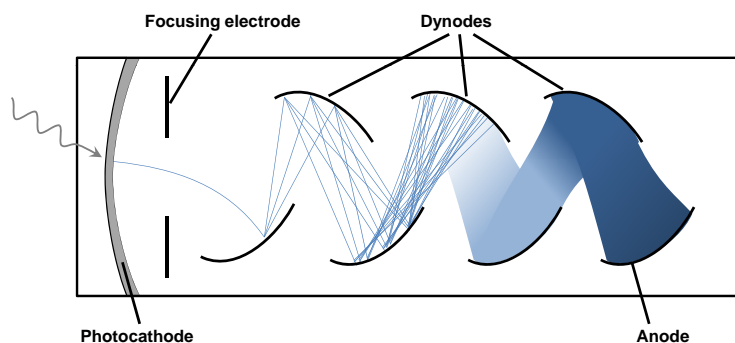
Figure 3.10: Working principle of a standard photomultiplier tube.

Through these processes, from one single photo-electron, 10^6 to 10^7 electrons are collected at the anode. By reading out the current flowing in between the first dynode and the anode, we then obtain a charge of about 1.6 pC. If we connect an oscilloscope, the integral of the signal from the PMT then is around 80 pVs (charge multiplied by R=50Ω). This in turn means that a signal in tens of mV should be readable over the duration of the PMT response (2-5 ns). This value is usually higher than the electronic noise background (a few mV) and therefore PMTs are widely used for their detection resolution that goes down to the detection of a single photon.

3.3.2 Acquisition techniques

One convenient way to readout the crystal response is to record directly the pulse shape acquired with an oscilloscope. A PMT indeed generates a gaussian signal for each individual photon generated during the scintillation process. This will lead to a characteristic pulse as illustrated in Figure 3.11. In the beginning of the pulse, the density of photons is high enough to form, through pile-up, a quasi-continuous curve. On the other hand, after 600 ns, the density of photons is too

low and the arrival of discrete photons does not allow the direct visualization of the exponential decay. It is however possible to record a set of pulses (100-1000) and sum them all, thus improving the statistics. The limitation of this technique is its time resolution. Since the single electron response (*SER*), sort of building block of the entire pulse, has a duration of a few nanoseconds, the rising part of the scintillating pulse will not be measurable with this technique.

To improve the resolution of timing measurements based on γ-rays excitations, it is possible to apply the *single photon counting* technique. In that case, the arrival time of single photons is measured against a fast reference. Since only one photon is measured at the time, all photons are equally probable and, after enough γ-interactions, the entire spectra can be reconstructed. It is actually the same principle than the one based on oscilloscope traces except that, with the single photon counting technique, the building block has no width. The only relevant limit in the time resolution is thus the time jitter of the start signal coming from the reference. This value can be reduced down to a few hundreds of picoseconds.
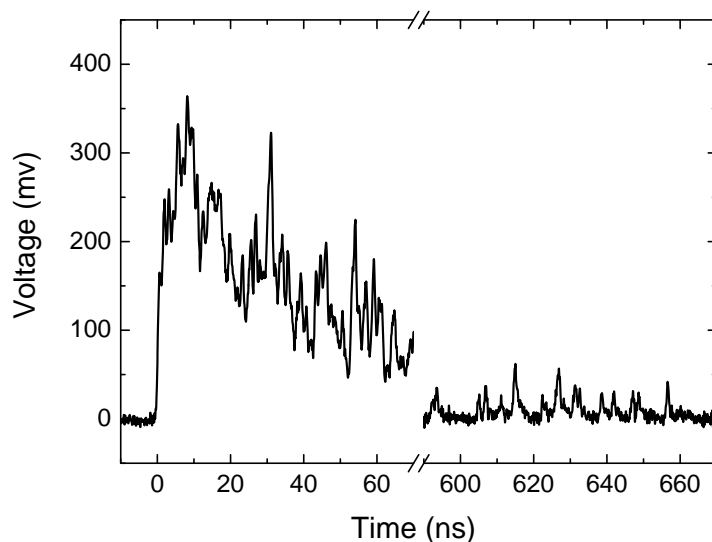
Figure 3.11: Single pulse induced by a 662 keV γ-ray interaction in LuAG:Ce.

3.3.3 Time properties of LuAG

The measurements were based on γ interactions of 511 or 662 keV, acquired in the single photon counting and pulse averaging modes. We have seen in section 2.3 that the Cherenkov threshold is lower than 100 keV for electrons. The interaction of the considered γ-rays can therefore lead to electrons (through either Compton or photo-electric effects) which are relativistic enough to generate Cherenkov light.
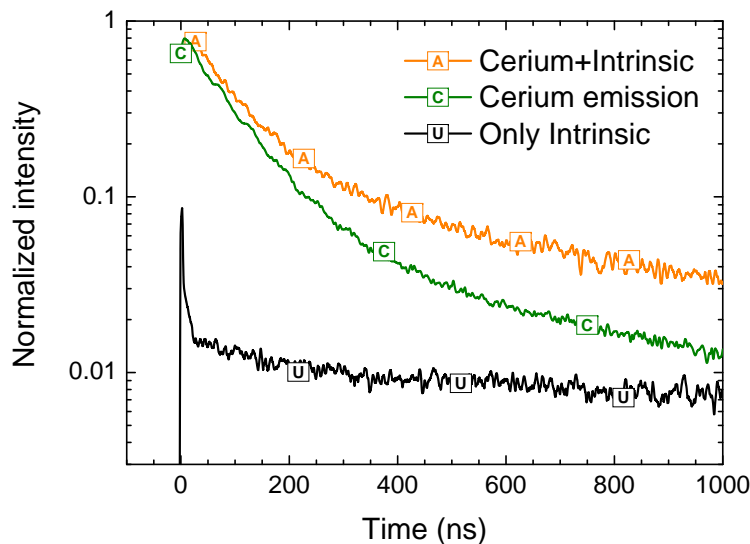
Figure 3.12: Pulse shape of an undoped sample (U), a Cerium doped sample integrated on all wavelengths (A) and the same sample integrated only in the Cerium emission spectra (C).

The scintillation pulses of undoped and Cerium doped LuAG are provided in Figure 3.12. As expected the time profiles of the undoped and doped samples differ significantly. The undoped sample presents a very sharp contribution attributed to Cherenkov photons. In addition a slow component ($\tau \approx 2.2$ μs) is visible which was attributed to the intrinsic exciton-related emission. The Cerium doped sample on the other hand does not show any Cherenkov signal. This can be explained with two reasons: the scintillation is much more intense when Cerium is inserted in the matrix and a certain part of the Cherenkov photons can be absorbed by the Cerium sites. The fastest decay constant observed

61

lies between 70 and 100 nanoseconds. Two other slower components (≈ 300 ns and 3μs) are also visible. Earlier results [50] proved that LuAG:Ce luminescence yields photons up to 300 μs. This tail of slow light was assigned to self-trapped excitons and to excitons localized around antisite defects [37, 39, 46].

In Cerium doped samples, this slow light is not only emitted in the UV since re-absorption of intrinsic emission by the Ce^{3+} is possible. In order to show this, the Cerium doped sample was also measured with a green filter. This allowed restricting the acquired time response to the light emitted by the Cerium sites (see curve C in Figure 3.12). We observe that the relative intensity of the slow component, although significantly lower, is still non-zero.

The decay curves of LuAG will be studied in more details in the next chapter. It will be highlighted that the growth technique is influencing the density of defects, thus leading to different time profiles. We will end this overview of the characterization techniques with the measurement of the light yield.

3.4 Light output

The light yield is a crucial parameter for a scintillator: for a given energy deposited inside the crystal, how much photons do we obtain? A light yield is typically expressed in photons per MeV. It is important to define properly what photons are being considered. The reason for this lies in the multiple steps needed for the generation of a signal. The first step has been described in the previous chapter: the conversion, by the crystal, of a certain amount of energy into low energy photons. This initial number of photons per unit energy is called the *absolute light yield* of the crystal.

This amount of photons is, in almost all cases, much higher than the number of photons that effectively generate a signal in the photodetector. Most of scintillators are indeed chosen to be dense and this criteria implies the refractive index to be high. Besides, in the frame of this particular type of calorimetry, high refractive indexes are also needed for optimized detection of the Cherenkov light.

However, a crystal with high refractive indexes such as LuAG ($n = 1.84$) restricts the amount of light that can exit through its faces. The condition for a photon to escape depends on its angle with respect to the normal of the exit surface and the difference in index of refraction of interface. The condition is fulfilled if the impinging angle is lower than the critical angle θ_c:

$$\theta_c = \sin^{-1} \left(\frac{n_{out}}{n_{crystal}} \right) \tag{3.6}$$

When a crystal is dry coupled (presence of an air layer) to the detector, the extraction cone is 32.9° . It is possible to increase it to 50.0° by using optical grease (typically $n_{out} = 1.41$). Since the scintillation light is emitted isotropically, a larger extraction cone means that the number of photons exiting the crystal increases. Therefore the number of photons arriving on the detector depends on the configuration in which the crystal was measured (e.g. the choice of coupling medium). Any choice of setup will actually modify the number of photons *measured* per unit of energy. Another important parameter is the environment of the crystal: what is placed around the crystal? Is there a coating or a wrapping? Are the photons rerouted inside the crystal when exiting through another face?

The reliable variable is the absolute light yield since it only depends on the scintillation properties of the crystal. Many studies have been dedicated to the measurement of this absolute light yield and it turned to be far from trivial [53]. Although the determination of the absolute light yield is of high interest to understand the limits of scintillation light, relative measurements are, in most cases, sufficient to characterize the material. The idea in that case is to select one setup for all the measurements and minimize the sources of deviations.

3.4.1 Geometrical considerations

All the samples investigated in the frame of this chapter had dimensions of $2 \times 2 \times 8$ mm^3. This allows two configurations: the crystal lying horizontally or standing vertically on the PMT window. In order to maximize the number of photons extracted, the face of the crystal in contact with the PMT window was covered with

optical grease[1] and Teflon tape[2] was used to cover the other faces. The efficiency of Teflon tape as a diffusive reflector was demonstrated earlier [54]. The vertical configuration, illustrated in Figure 3.13, was selected for sample comparison. This setup is a good compromise between number of photons extracted and repeatability of the measurement (experimental error around 12%). The horizontal configuration extracts between 45 and 60 % [55] more light but the experimental error is much higher since covering the small lateral faces with Teflon in a repeatable way is rather difficult.
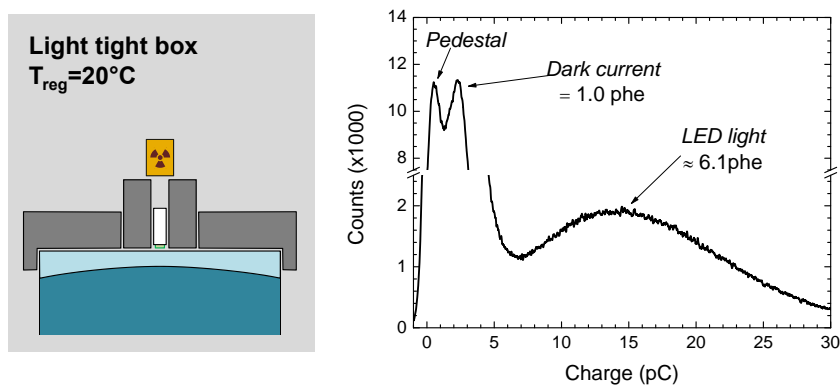
Figure 3.13: Setup for the measurement of the light output (left) and calibration methods based on single electron response and LED-triggered Poissonian distribution centered around 6.1 phe (right).

3.4.2 Calibration

The measurement of the number of photons was based on PMT signals. We mentioned in section 3.3.1 that one single photo-electron generates a charge of around 1.6 pC. By computing the area of the scintillating pulses and comparing the obtained value with the value of the single electron response (SER), we can obtain the number of photo-electrons contained in the pulse. An example of charge spectrum is provided for illustration in Figure 3.13. The difficulty is then to determine this calibration factor with the best resolution since it will have a

---

[1]Rhodorsil paste 7
[2]RS thread seal tape 12mm$\times$75μm

major contribution to the experimental error. The SER was determined here with two techniques. The first technique takes profit from the dark current of the PMT. Because of the high voltage supplying the tube, spontaneous thermally-assisted emission of an electron is possible. This electron will undergo the multiplication chain and lead to a charge which is statistically very close to the SER. The probability to emit two electrons simultaneously is indeed very weak.

The second approach was based on the detection of light generated by a pulsed LED. By changing the value of the current flowing in the LED, the number of photons emitted can be tuned. The response of the PMT can then be obtained for several values of LED current. Since both the PMT and the LED are governed by Poisson statistics, the number of photons can be extracted from the statistical distribution of the pulses. More advanced models also include after-pulsing and noise contributions, as discussed in [56].

This careful calibration is usually performed once, together with a reference measurement. The reference measurement can be selected to have a high number of photons and therefore reduce the amount of time necessary for the calibration, which then becomes applicable in a routine measurement. For this reference measurement, we selected a crystal of Lutetium Yttrium Aliminum perovskite (LuYAP) tucked into a Teflon holder that tightly fits the diameter of the PMT. Since the crystal is never removed from its holder, minimal deviations are observed (less than 3%). Each set of measurement was preceded by this reference thereby allowing compensating the fluctuation of the PMT gain. Since a major source of fluctuation is temperature, the box containing the setup was in addition set at a regulated temperature of 20°C for all measurements.

3.4.3 Quantum efficiency

To obtain, from the number of photo-electrons, the number of photons that where sent on the detector, the quantum efficiency of the photocathode has to be taken into account. The wavelength dependent curve is provided in Figure 3.14 for the PMT[1] selected for these measurements.

---

[1]XP2020Q from Photonis
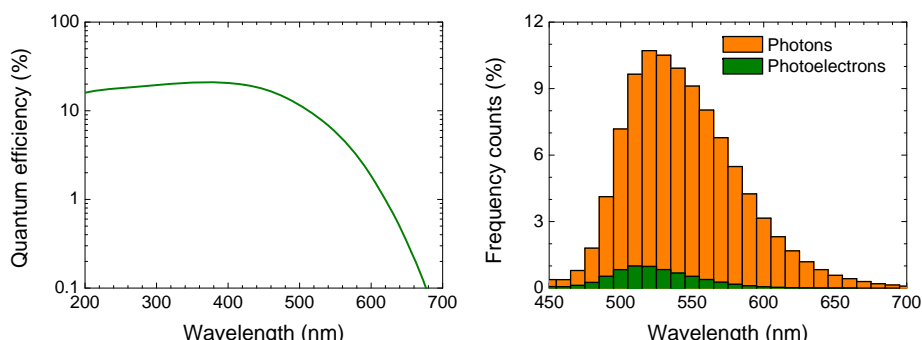
Figure 3.14: Quantum efficiency of the photocathode of a XP2020Q (left) and distribution of the photons and respective photoelectrons for LuAG:Ce (right).

A maximum efficiency of 22% is observed with photon wavelength close to 400 nm but the efficiency quickly drops after 500 nm. By convolving the emission of the sample with this curve, we obtain the average quantum efficiency for the photons emitted by the crystal.

The average quantum efficiency was found to be around 18.5% for an undoped LuAG and around 6.0% for a Cerium doped sample.

3.4.4 Integration time

Another important aspect of the light yield computation is the selection of the adequate time window. The area of a pulse is computed over a certain range and, since the crystals present a non-negligible slow component, the selection of the integration time will affect the number of photons computed. For our purposes, the time window was set to the maximum value of the acquisition device which is 4.1 μs. This choice was made in order to integrate the maximum number of photons. Obviously, in this case, no separation is performed between the fast and the slow components. Nevertheless, this information is easily obtained by comparison of the pulse shapes of the crystals (see section 3.3).

3.4.5   Light output setup

In the frame of this thesis, the pulse area was computed with a desktop digitizer[1]. This device has a build-in trigger that is based on both low and high frequency filters designed to cancel noise fluctuations. The triggering method is based on a so-called *delta function* (see Figure 3.15 for illustration) which behaves as a constant fraction discriminator. A baseline identification (see *baseline* curve on graph) is also performed. Finally, after baseline substraction, the signals are integrated over a certain time window (see *gate* curve on graph).
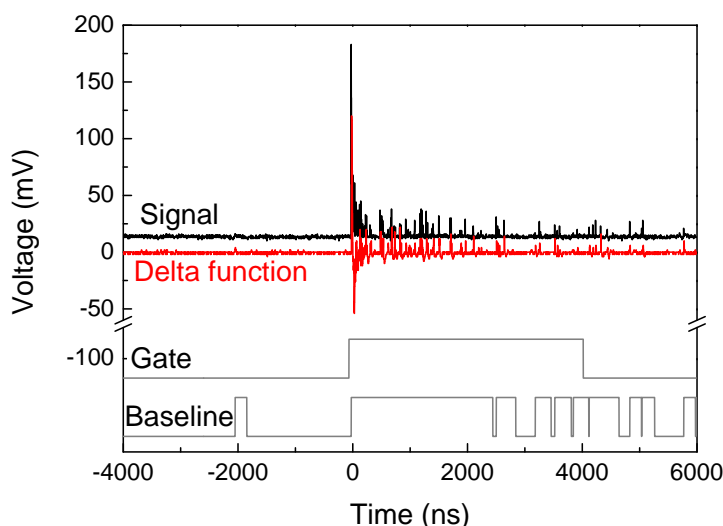
Figure 3.15: Processing of the scintillation pulses as performed by the digitizer.

3.4.6   Charge spectra

We mentioned earlier that scintillation is a statistical process. The probability of interaction of a γ-ray via photo-electric or Compton effects are indeed intrinsically statistical. In order to separate these two different mechanisms, we build a histogram out of the areas of each individual pulse acquired. Figure 3.16 provides an example of charge spectra obtained with the reference crystal of LuYAP. A photopeak, corresponding to the full absorption of the γ-ray, is

---

[1]CAEN DT5720, 12 bits 250 MS/s

clearly visible, well-distinguished from the Compton continuum. In addition, some back-scattered peaks are noticable. These are due to γ interactions with the environment of the crystal, (i.e., shielding of the radioactive source, metallic parts of the box, etc).
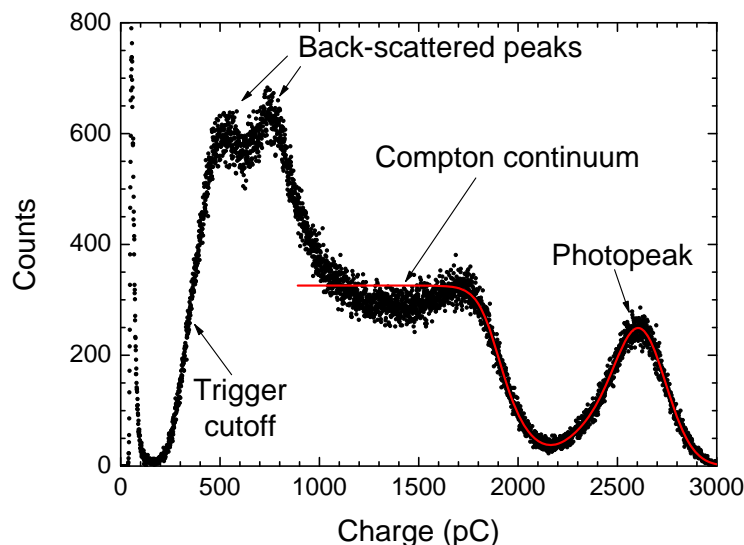
Figure 3.16: Charge spectra of the reference LuYAP crystal.

The area of the photopeak with respect to the one of the Compton continuum is function of the stopping power of the material and the geometry of the sample. For instance, a crystal with small stopping power which in addition present small dimensions is, on the contrary to the samples studied here, not very likely to present any distinguishable photopeak. For an accurate determination of the light output it is important that this peak is present. Since a photo-electric interaction absorbs the entire energy, it is convenient to use this feature for calibrating the light output. The Compton continuum and the photopeak can be fitted with:

$$f(x) = A_{pp} e^{-2\left(\frac{x-x_{pp}}{w_{pp}}\right)^2} + \frac{A_{cpt}}{\sqrt{1 + (x/x_{cpt})^{w_{cpt}}}} \tag{3.7}$$

where A_{pp}, x_{pp} and w_{pp} are the amplitude, position and full-width at half-maximum (FWHM) of the Gaussian photopeak. Likewise, A_{cpt}, x_{cpt} and w_{cpt} are the amplitude, position and steepness of the Compton continuum.

In this particular measurement, the photopeak of the reference is centered at 2614 pC. The corresponding amount of photoelectrons (phe) was determined (through calibration) to be equal to 1170 for 622 keV γ-rays. We then obtain a SER equal to 2.23 pC.

3.4.7   Light output of LuAG crystals

Charge spectra were also acquired for a sample of LuAG:Ce ($\sim$0.09 at.%) both in vertical and horizontal configurations. The charge spectra are provided in Figure 3.17. From the position of the photopeak, we obtain the number of photoelectrons (phe) based on the value of the SER. Dividing by the quantum efficiency, we obtain the number of photons (ph). The light output is finally obtained by normalizing to the energy of the source.

The values obtained are summarized in the following table:

	vertical	horizontal
Charge (pC)	1900	2930
Number of phe	850	1310
Number of photons	14 600	22 500
Light ouput (ph/MeV)	22 000	34 000
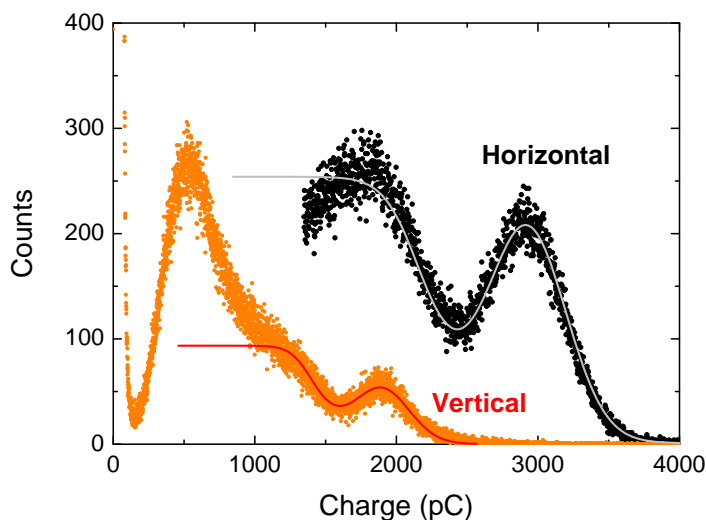
Figure 3.17: Charge spectra of a Cerium doped LuAG crystal.

We are thus able to extract up to 34 000 photons per MeV of incoming energy. This value is significantly higher than the ones obtained in [55] especially for this rather low doping concentration. It is important to remember that the light ouput was computed here on a time window of 4.1 μs. When such a long integration time is considered, the number of photons equals values of Lutetium oxy-orthosilicate, Lu_2SiO_5 (commonly refered as LSO) measured in the same configuration [57]. But, contrary to LuAG, LSO is emitting this light in less than 100 ns which is a decisive advantage. Nevertheless, theoretical computations, based on the Bartram Lempicki model, announce an absolute light yield for LuAG:Ce close to 60 000 photons/MeV [41]. This shows the high potential of LuAG and explains the number of attempts to "speed up" the slow light.

The different experimental methods, which were previously explained for a selection of samples, were applied to the entire set of samples. The next section will discuss in more detail the effect of inserting Cerium doping centers as well as co-activators in the LuAG matrix.

3.5   Study of the properties of LuAG:Ce

In this section, the light output and the timing properties will be discussed as a function of the concentration of Cerium. The importance of co-doping centers in YAG and LuAG matrices was recently demonstrated [41, 58, 59, 60]. For what concerns LuAG:Ce, it was shown that the insertion of Ga^{3+} significantly decreases the amount of slow light [61]. As a complement to these studies, the use of Hafnium and Scandium as co-dopant was investigated. We remind that all the crystals investigating here were grown using the vertical Bridgman technique by A.G. Petrosyan from the Institute for Physical Research in Ashtarak, Armenia.

3.5.1   Samples studied

The discussion will be based on two batches of LuAG:Ce with different values of Cerium concentration as well as three batches with Hf and Sc co-doping. More details on these samples can be found in Table 3.1.
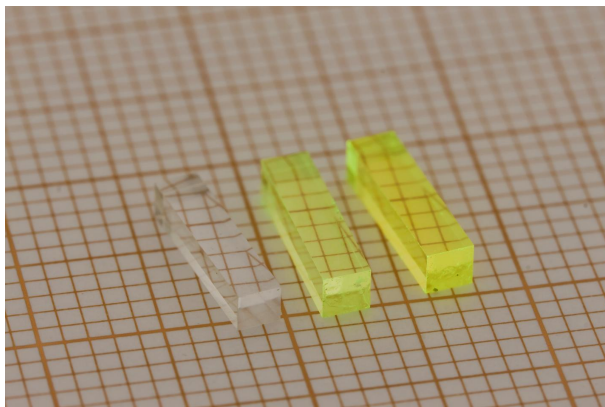
Figure 3.18: Crystals of LuAG ($2\times2\times8$ mm^3) with no doping (left) and with 0.1 (middle) and 0.5 (right) at.% of Cerium doping.

Reference	Crystal ID	% Ce	% Ce corrected	Co-doping
Batch1	2011	0.09	0.09	-
	2013	0.00	0.00	-
	2015	0.08	0.08	-
	2016	0.18	0.18	-
	2017	0.36	0.26	-
	2018	0.55	0.44	-
Batch2	2609	0.08	0.15	-
	2610	0.15	0.28	-
	2611	0.44	0.41	-
	2612	0.50	0.59	-
Hf30	2198	0.10	0.13	30ppm Hf
	2201	0.30	0.21	30ppm Hf
	2202	0.40	0.30	30ppm Hf
Hf45	2222	0.20	0.23	45ppm Hf
	2223	0.20	0.27	45ppm Hf
Sc	2632	0.25	0.28	1.5 % Sc
	2633	0.42	0.38	1.5 % Sc
	2634	0.65	0.61	1.5 % Sc

Table 3.1: List of samples.

3.5.2 Cerium concentration

As mentioned in section 3.2.4, the Cerium absorption, computed from transmission measurements, can lead to a reliable estimator of the concentration of dopant in the host matrix. Values of Cerium concentration were already estimated by the producer based on the method described in [44]. A second estimation was nevertheless performed based on both longitudinal and transversal measurements. As discussed earlier, this technique does not depend on surface effects and is in addition weakly dependent on the saturation of the transmission curve. The Cerium absorption coefficient obtained at the maximum of the $5d - 4f$ absorption band, plotted against the Cerium concentration estimated by the producer, is provided in Figure 3.19.
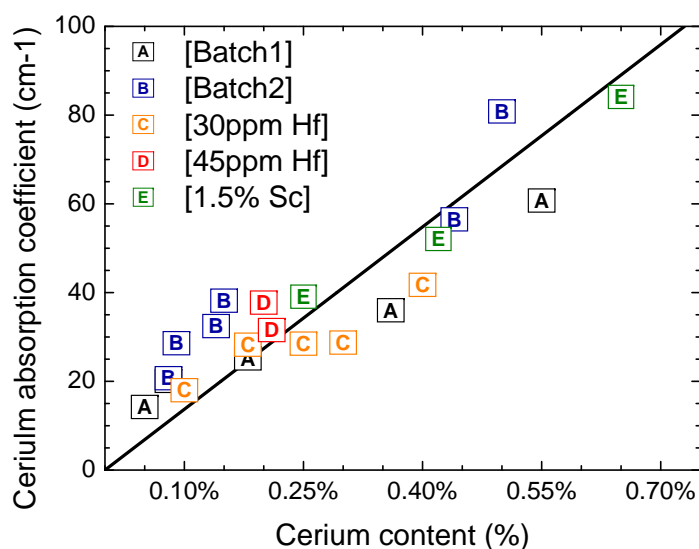
Figure 3.19: Cerium absorption coefficient at 450 nm versus Cerium doping concentration as measured by the producer.

A linear fit then leads to the following empirical formula:

$$[\text{Ce (at.\%)}] = \frac{\alpha(5d - 4f)}{k} \quad \text{with} \quad k = 137 cm^{-1} \tag{3.8}$$

This value is in agreement with the values obtained in [44]. Some sample to sample deviations are however visible and therefore we decided to correct for

these fluctuations. The effective Cerium concentration obtained from the Cerium absorption through (3.8) is provided in Table 3.1.

3.5.3 Transmission curves

We verified that no significant change in the photon interactions are visible when co-doping centers are added to the host matrix. In Figure 3.20, the transmission curves of four LuAG:Ce crystals are provided. These crystals had a similar Cerium concentration (≈ 0.3 at.%).
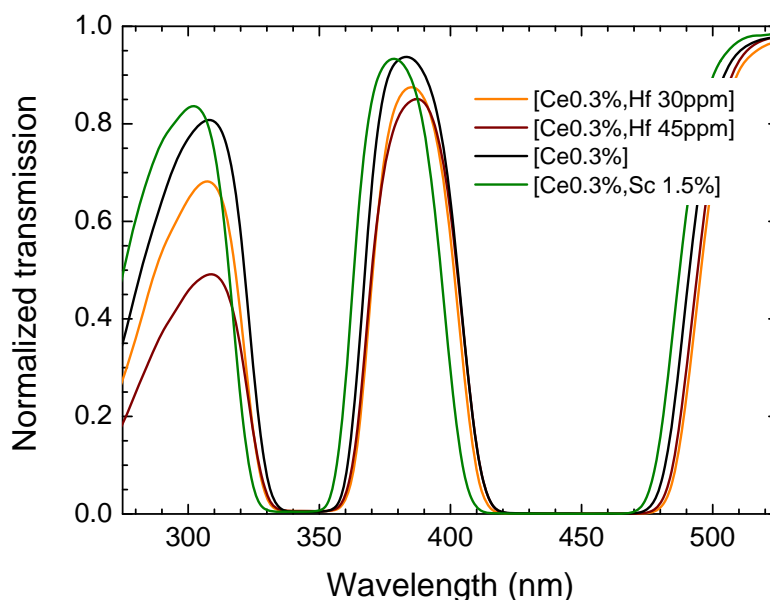
Figure 3.20: Normalized transmission curve for Cerium doped crystals and effect of Hf and Sc co-activators.

We observe that the Hafnium co-dopant seems to slightly affect the overall UV transmission, especially for a concentration of 45 ppm. The insertion of Scandium on the other hand seem to slightly shift the Cerium absorption bands towards higher energies. However no extra absorption regions are visible which is our major concern. The objective of a co-dopant is to improve some properties (timing in this case) while keeping others parameters untouched.

3.5.4 Light output

The light outputs of all LuAG:Ce samples were measured in the vertical configuration (as in Figure 3.13) over a time window of 4.1 μs. The values are plotted against the Cerium concentration in Figure 3.21.
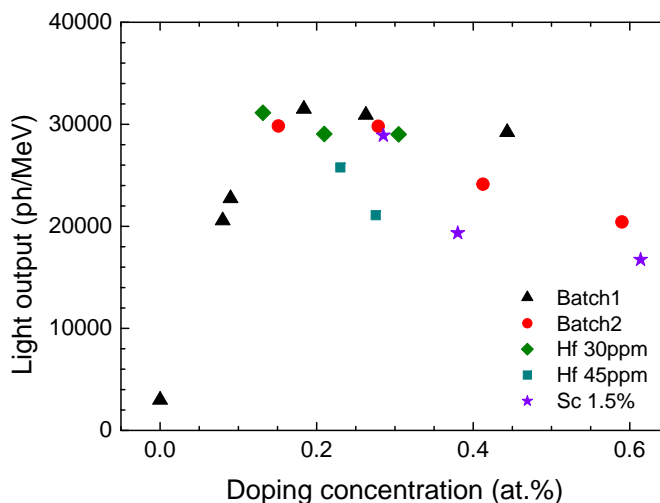
Figure 3.21: Light output versus Cerium concentration.

Samples with no Cerium show a light output (in this particular configuration) of around 3000 photons per MeV. These photons are the result of the intrinsic scintillation of the matrix and are thus emitted in the UV region. When the Cerium concentration increases, an initial rise of the number of photons is visible. The fact that the number of photons generated increases is due to the increase of the probability of recombination at the Cerium sites. This results from a higher number of radiative recombinations with respect to the non-radiative ones. We note however that quickly, around 0.2 at.%, a maximum is reached. When the doping concentration further increases, the number of photons emitted then decreases resulting of the quenching mechanisms. The Cerium concentration becomes indeed high enough to favor exchange of carriers in between luminescent sites. This increase in the mobility of the carriers will in turn lead to a higher probability that non-radiative traps are found on the path of these carriers. From one batch to another, the dependence of the light output on the Cerium concentration can vary. This can be attributed to the quality of the raw materials.

Crystals with 30 ppm of Hafnium co-doping show a very similar behavior as compared to previous samples. The effect on the scintillation light generation appears to be negligible. When the co-dopant concentration is increased to 45 ppm, a lower number of photons emitted is however observed. Whether this is a drawback or an advantage will be determined based on the decay time of these crystals. We especially want more light in the first part of the pulses. Therefore if the crystal is significantly faster then, even with a weaker light output at 4 μs, it is not excluded that the density of photons in the first 500 ns is actually higher.

The use of Scandium as co-dopant leads to a light loss in this time window for high Cerium concentration but no obvious changes in the light output are visible when the concentration is lower than 0.3 at.%.

3.5.5 Timing properties

We provided in the previous section the number of photons emitted in the first 4 μs, in order to investigate the density of photons in time, the average pulse (see section 3.3.2) was subsequently computed for all samples. The pulse shapes obtained were then fitted with a three component exponential. The fitting curves, normalized to their maximum, are provided in Figure 3.22.
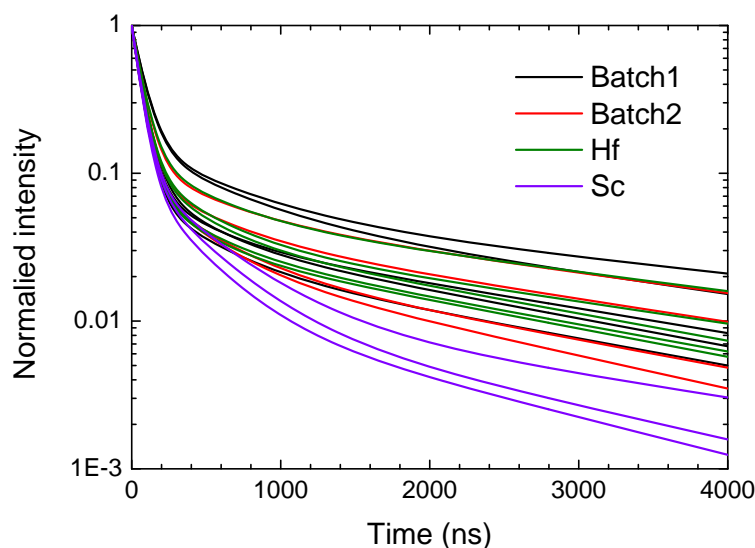
Figure 3.22: Normalized pulse shapes.

The raw data is not provided here since it did not allow multiple curves to be displayed (due to noise oscillations in the pulse shapes). From the graph we observe that the samples co-doped with Scandium present a noticeably faster decay as compared to LuAG:Ce and LuAG:Ce,Hf samples.

The relative weight of each of the three components were also plotted against the value of the decay constants. The relative weight w_i is defined as the ratio of the area under the component i and the area of the entire pulse; it thus writes as follows:

$$w_i = \frac{A_i \tau_i}{A_1 \tau_1 + A_2 \tau_2 + A_3 \tau_3} \tag{3.9}$$

where A_i and τ_i are the amplitude and decay constant of component i.

In Figure 3.23, the size of the points is proportional to the Cerium concentration. This emphasizes the fact that the decay constants get lower as the Cerium concentration increases. The weight of the slow component is also decreasing with the Cerium concentration. This is again consistent with quenching mechanisms.

For calorimetry purposes, where collisions have high repetition rates, a lower amount of slow light would be of great help. The idea is to minimize the pile-up of all the scintillation pulses that could occur when the crystal is hit by another particle while still emitting light triggered by previous events. In this line of thought, higher Cerium concentrations seem to be favorable.

We note that the co-doping with Hafnium does not bring any significant modification in the pulse shape. This indicates, together with the fact that they show a light output similar to LuAG:Ce, that this type of co-dopant is of low interest for what concerns our crystals. On the other hand, Scandium co-doping seems to improve the timing properties of the crystals.

Figure 3.24 shows in more details the dependence of the relative weight of the component on the Cerium concentration. It is clearly visible that, while higher Cerium concentration leads to a higher photon density in the first part of the scintillation pulse, Scandium co-doping further increases this effect.
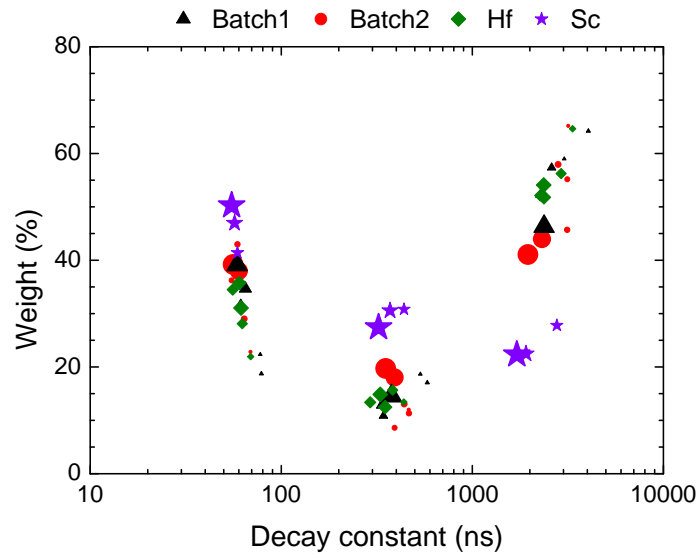
Figure 3.23: Weight of component versus its decay for Cerium doped LuAG crystals (batch 1 and 2) and with Hf and Sc co-doping.
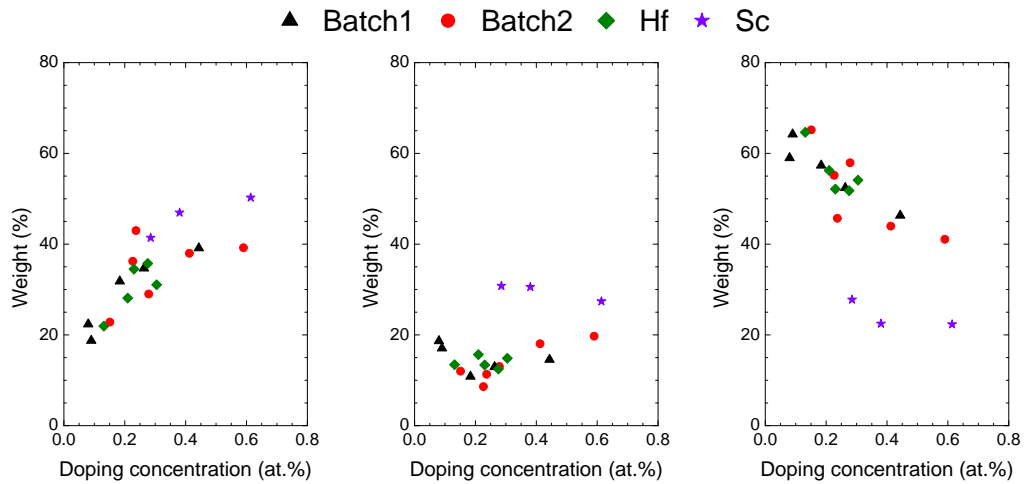
Figure 3.24: Weight of first, second and third decay component versus Cerium concentration for a set of LuAG crystals.

3.5.6 Light output for different integration times

In order to better separate the contribution of the slow and fast scintillation light, it is worth combining the information on the light output and the pulse shapes. This was already studied in [62] for LuAG:Ce samples. In this paper, the acquisition window was changed on the light output bench hardware in order to record several charge spectra with different gating times. We decided here to take profit from the pulse shapes instead. We know from the light output values the number of photons in the first 4.1 μs and in addition we know from the pulse shapes how they are distributed in time over this time window.

Reducing the gating time is thus synonym of computing a partial integral of the pulse. Figure 3.25 shows the values obtained for three different gating times: 180 ns, 1.2 μs and 6 μs, which correspond to three times the value of the respective decay constants.
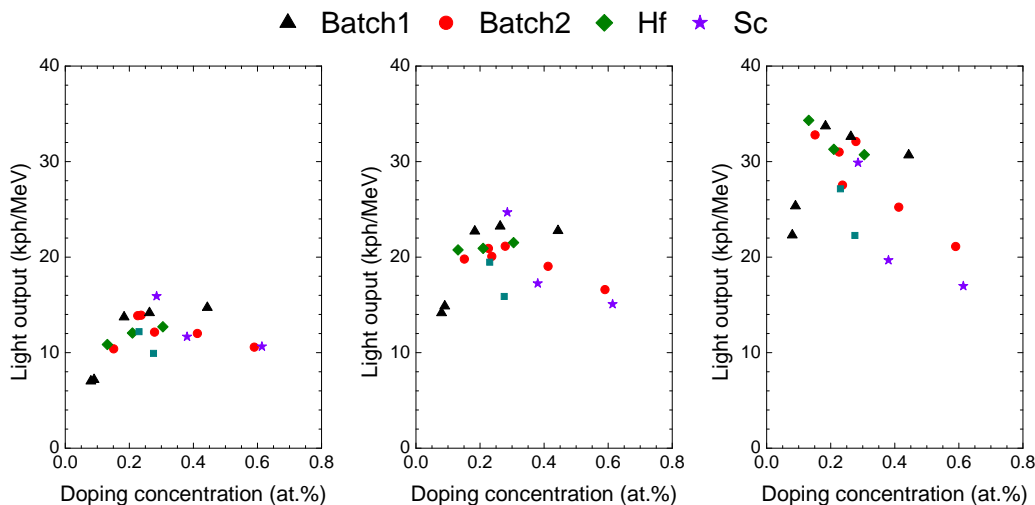
Figure 3.25: Light output of the LuAG crystals versus Cerium concentration for gating times of 180 ns (left), 1.2 μs (middle) and 6 μs (right).

The best results are thus obtained for Cerium concentrations higher than 0.2 at.%. At high concentrations, the light yield in the first 150 ns is not significantly higher but the slow component is noticeably quenched. The objective is to convert the slow light into fast light but, if this is not possible, decreasing the amount

of slow light while maintaining the amount of fast light is already an important step forward. High doping concentrations are very likely to alter the mechanical properties of LuAG matrices, especially in fiber geometries. For these reasons, too high Cerium concentration should not be considered. Scandium co-doping is then an interesting alternative since it outperforms non co-doped LuAG:Ce for lower Cerium concentration.

3.6 Energy resolution

From the charge spectra, it is also possible to estimate the energy resolution of the crystal defined as the ratio of the full width at half maximum and the position of the peak. In Figure 3.26, the energy resolutions of the LuAG samples are plotted against the number of photoelectrons collected in the measurement.
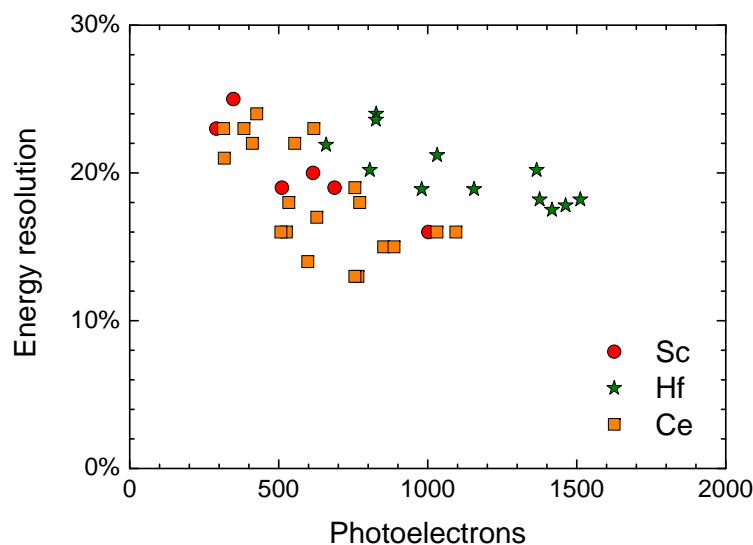
Figure 3.26: Energy resolution versus number of photoelectrons.

Photo-statistics contribute to the energy resolution with a $1/\sqrt{n_{phe}}$ term. This contribution is not sufficient to explain the behavior observed here. Among other contributions, light transport is very likely to be dominant: depending on the birth location of the photons, they do not have the same extraction efficiency.

We observe a rather large sample to sample fluctuation. We could not determine whether this was due to better intrinsic performances or better optical quality. The energy resolution of samples codoped with Scandium is very similar to crystals without co-dopant. On the other hand, Hafnium co-doping may induce some degradation of the crystal resolution.

The characterization work presented in this chapter demonstrates that LuAG is a good candidate for being used as host matrix in the frame of the fiber shaped dual-read out calorimetry studied in this thesis. Despite the progress brought by the use of co-dopants, as compared to other crystals (LSO namely), the timing properties of LuAG:Ce are not yet optimized. The fundamental reason for the selection of LuAG lies in its mechanical properties that allow more stable growths of fiber-shaped geometries.

Chapter 4

Growth technique dependent quality of LuAG

The quality of single crystals is very dependent on the equilibrium reached during the growth process. The LuAG crystals studied in the previous chapter were grown by the Bridgman technique. As shown in Figure 4.1, the melt is encapsulated in an ampoule and the thermal gradient applied maintains the lower part of the container at a cooler temperature as compared to the top. The slow motion of the ampoule towards lower temperatures initiates the crystallization and the growing crystal substitutes for the melt.

Bridgman   **Czochralski**   **Micro-pulling down**
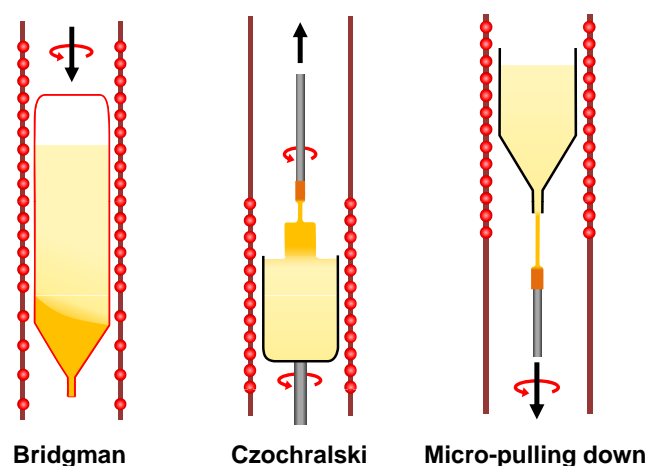
Figure 4.1: Crystal growth techniques. Sketch adapted from [36].

Another widely used approach, is the Czochralski process (see middle sketch in Figure 4.1). In this case, the temperature gradient at the phase boundary between the seed and the melt initiates the crystallization process. The crystal is then grown by slowly lifting the seed. This technique, based on larger melting zone, allows reaching the best equilibrium conditions. Lower defects concentrations in the matrix are thus expected.

The micro-pulling down technology (μPD) which allows the growth of single-crystalline fibers is illustrated in the right sketch of Figure 4.1. Before being brought in contact with a seed crystal, the melt passes through a nozzle of a few millimeters in diameter. Rod-like single crystals of the desired orientation and shape can be produced with high pulling rates. Typical diameters range from 300 μm to 3 mm. From the three techniques, the micro-pulling down technology is characterized by the narrowest melting zone. It is therefore more likely to generate a significant amount of stress in the host matrix.

This chapter aims at investigating these differences by studying the traps of LuAG samples grown by the three different methods. The approach was based on thermally-stimulated luminescence (TSL). During a TSL measurement, the sample is first irradiated (usually with X-rays) for a period sufficiently long to fill the traps with carriers. In a second stage, the temperature is increased in order to progressively release the carries from their traps as the thermal energy increases. Luminescence can then be observed if the recombination of the released carriers occurs radiatively. This chapter does not aim at providing theoretical background on TSL. Only some basic principles, needed for better understanding the results discussed, are provided here. An in depth presentation of TSL can be found in [63].

We investigated the following set of samples:

- 1 undoped LuAG sample grown by μPD (F_0)
- 1 Cerium doped (0.1 at.%Ce) LuAG sample grown by μPD (F_1)
- 1 Cerium doped (0.1 at.%Ce) LuAG sample grown by Bridgman (Bg)
- 1 Cerium doped (0.22 at.%Ce) LuAG sample grown by Czochralski (Cz)

Samples Bg and Cz have a square section equal to 2 by 2 mm² and sample F_0 and F_1 have a round section of diameter 2 mm. All samples were cut into slices of 1 mm thickness. Having similar geometries for all the samples is very important to allow sample to sample comparison. This is especially true for the thickness since it determines the thermal gradient observed in the material upon heating. The temperature regions where charge carriers are freed can indeed slightly shift if the thickness changes.

4.1 TSL below room temperature

In order to study the shallow traps responsible for the delayed recombinations of charge carriers, the temperature of the sample must be decreased significantly.

4.1.1 Setup description

The setup used for this work (see Figure 4.2) is the one of the Material Science department of the University of Milano Bicocca and was done in collaboration with the group of A. Vedda. The sample is inserted in a vacuum chamber (10^{-10} bar) and is coupled with Silver paint to a cold finger. The helium compressor which is connected to this cold finger allows reaching temperatures close to 10 K.
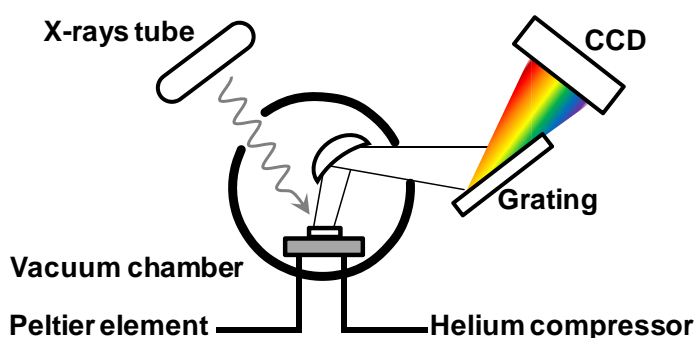
Figure 4.2: Setup of the TSL measurements performed below room temperature.

When the sample is cooled down, an X-rays tube supplied with 20 kV and 20 mA is irradiating the sample for durations between 30 seconds and 15 minutes

(depending on the intensity of the sample luminescence). After irradiation, a heating system is increasing the temperature back to room temperature at a constant heating rate of 0.1 K/s.

The luminescence photons emitted during the heating process are collected with a parabolic mirror and sent to a grating coupled to a nitrogen-cooled CCD camera which acquires a wavelength spectrum every 1.5 K. Each of these spectra were corrected individually for the background noise and the spectral sensitivity of the CCD. The background was estimated with a double exponential fit in the regions of the spectrum where no photons were emitted (see Figure 4.3).
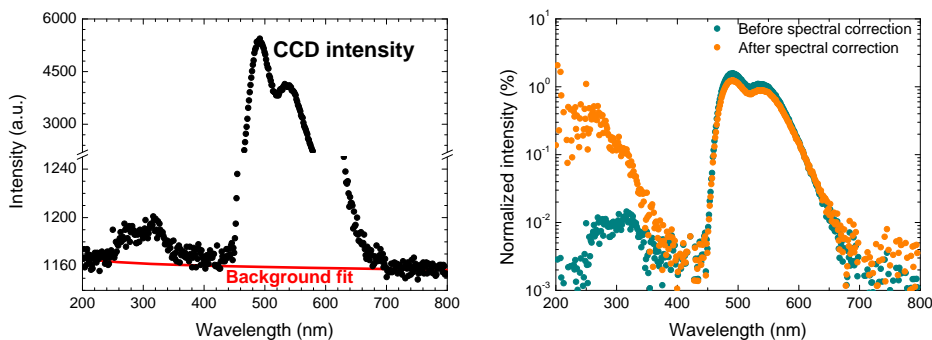
Figure 4.3: Background removal (left) and correction for spectral response of the CCD (right).

4.1.2 Contour plots

After a run such as the one described earlier, the luminescence photons acquired as a function of temperature are wavelength resolved. It is thus possible to study the TSL for different regions of the emission spectrum, separating for instance the intrinsic emission of the crystal from the Cerium emission. One convenient way to present the data are contour plots where the signal is plotted versus temperature and wavelength of emission. The contour plots of the samples grown by Czochralski, Bridgman and micro-pulling down are provided in Figure 4.4.

As expected, the undoped sample (F_0) shows a strong signal in the UV region. Some sharp peaks are observed between 550 and 720 nm which can be attributed
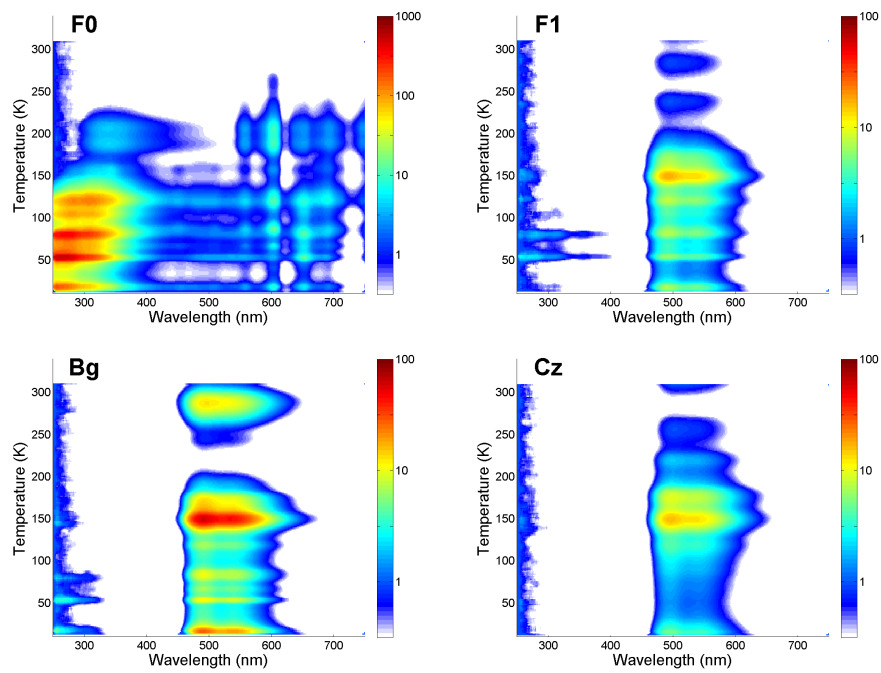
Figure 4.4: TSL contour plots of LuAG samples grown by micro-pulling down (F0 and F1), Bridgman (Bg) and Czochralski (Cz) as a function of temperature and wavelength. F_0 is undoped whereas other samples are Cerium doped.

to Europium impurities. The concentration of these impurities is two orders of magnitude lower than the exciton-related luminescence and can thus be neglected in the frame of this study.

The Cerium doped samples present intense luminescence in the 450-600 nm region. The intrinsic emission is also visible on samples F_1 and Bg. Its absence on the TSL contour plot of sample Cz can either be due to a higher concentration of Cerium or a better quality of the matrix (less Lu_{Al} antisites).

4.1.3 Emission spectra versus temperature

We integrated the contour plots on a few temperature regions in order to reveal the temperature dependency of the emission spectra of the samples. Figure 4.5 compares the emission spectra of an undoped sample and a Cerium doped one, both grown by μPD at different temperatures.
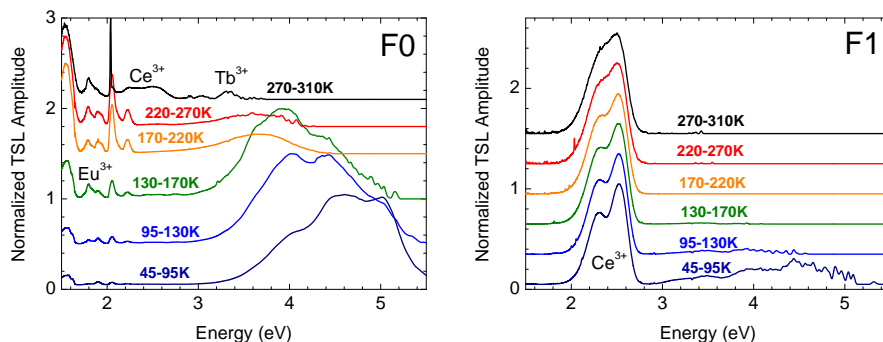
Figure 4.5: Emission spectra at different temperatures.

On the emission spectra of the undoped sample (F_0), the exciton-related emission bands are visible between 3.5 and 6 eV. We note that the intensity of these emission bands are temperature dependent. The emission at 5 eV is for instance much weaker above 95 K. For temperatures higher than 270 K the intrinsic emission is no more distinguishable. Traces of Ce^{3+}, Eu^{3+} and Tb^{3+} are noticeable instead.

As expected, the doped fiber (F_1) shows intense Cerium emission bands. Because of the reasonable doping concentration (around 0.1 at.%) exciton-related emission is nevertheless still distinguishable below 150 K.

4.1.4 Glow curves

Based on the emission spectra computed above, the contour plots were integrated on a set of wavelengths. We selected two regions for the samples doped with Cerium: 280-400 nm and 450-630 nm. The contour plot of the undoped sample was integrated on three regions since the two emission bands seem to present a slightly different behavior. The set of curves, so-called glow curves, are provided in Figure 4.6. These curves allow visualizing the temperature at which the carriers are released.
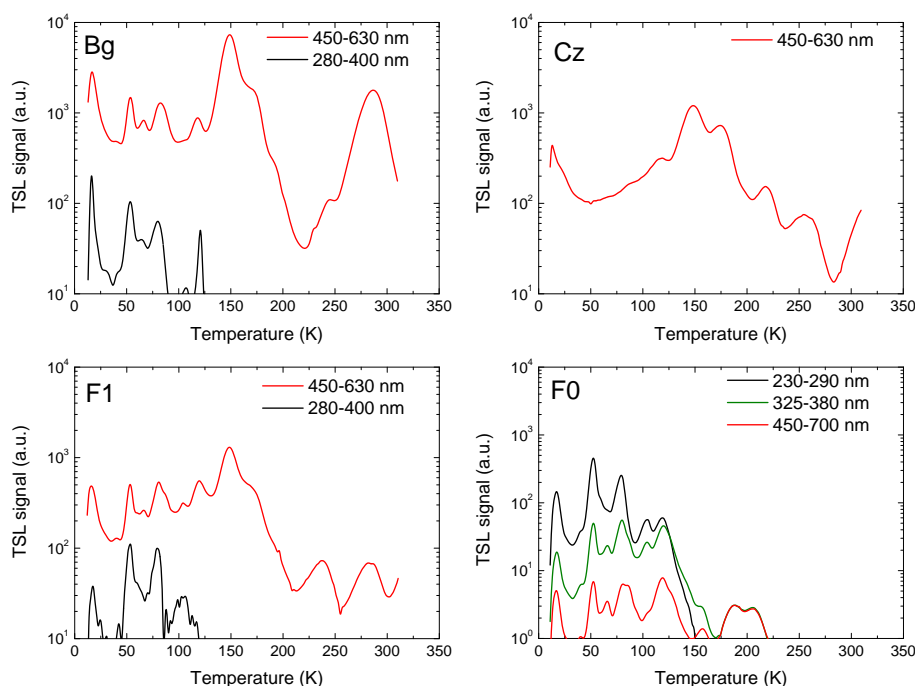
Figure 4.6: Glow curves of the four samples of LuAG for a set of wavelengths.

For the discussion, we will distinguish three different regions on the obtained glow curves : $T < 120$ K, $120 < T < 200$ K and T> 200 K.

From 10 to 120 K As already illustrated by the contour plot presented earlier, the sample grown by Czochralski (Cz) has no UV emission distinguishable from the noise. The other samples, on the other hand, present sharp UV luminescence peaks between 50 and 120 K. Interestingly these peaks are also observed when

the glow curve is computed in the 450-630 nm region (instead of 280-400 nm). We mentioned earlier that the intrinsic luminescence can partly be re-absorbed by the Cerium sites. The fact that the TSL peaks are observed on both regions of the spectra can be due to this self-absorption. We therefore suspect these peaks to be an intrinsic feature.

The broad featureless glow curve which is observed in this region instead for the sample grown by Czochralski was attributed to athermal tunneling. Charge carriers which are not supposed to be freed at these temperature can escape from the trap by tunneling effect. Athermal tunneling is characterized by a $1/t$ law [64]. This in turn means an inverse dependence with temperature since the heating rate is constant. Such time dependences were observed experimentally and discussed in [65]. This tunneling is visible on all samples. The sharps peaks present on samples F_0, F_1 and Bg are in fact superimposed to this tunneling pattern. We note that no tunneling pattern is observed when the glow curve is computed in the UV region. This most probably means that the tunneling is accompanied by a recombination of the charge carriers at the Cerium sites.

We can then conclude that the broad featureless pattern is likely to increase with Cerium concentration whereas the sharp peaks are likely to be independent of the doping concentration.

From 120 to 200 K In this region, no significant signal is visible in the UV whereas intense luminescence is observed between 450 and 650 nm when the sample is doped with Cerium. This is a hint that the charge carriers freed at these temperatures recombine at the Cerium sites. Earlier results [66] are in agreement with this assumption. In that paper it was shown that these TSL peaks are actually due to electrons being freed from Lu_{Al} antisites. It is very likely that these traps are also responsible for the tunneling observed at lower temperatures. This would imply a close spatial correlation of Lu_{Al} and Ce^{3+} sites.

From 200 to 310 K For these temperatures, the glow curves of the Cerium doped samples show two more peaks. The intensity of these peaks seems to be

dependent on the growth technique. As opposed to the two others, the crystal grown by Bridgman presents indeed an intense peak at 280 K.

4.1.5 Understanding the TSL peaks

The TSL peaks observed on the glow curve are due to the progressive emptying of traps. It is possible to investigate single traps by the so-called *partial cleaning* technique. This method is based on a partial heating up to a certain temperature (typically the position of the maximum of the peak). The sample is then quickly brought back to a lower temperature to *freeze* the charge carrier release. A TSL measurement is then performed starting from this temperature. Because of the pre-heating, the traps appearing at lower temperatures in the glow curve are expected to be empty (provided the TSL peaks are not too close). The rising part of the peak can then be accurately resolved, as shown in the inset of Figure 4.7. For this measurement, we selected the peak at 285 K since its intensity varies significantly depending on the growth technique.
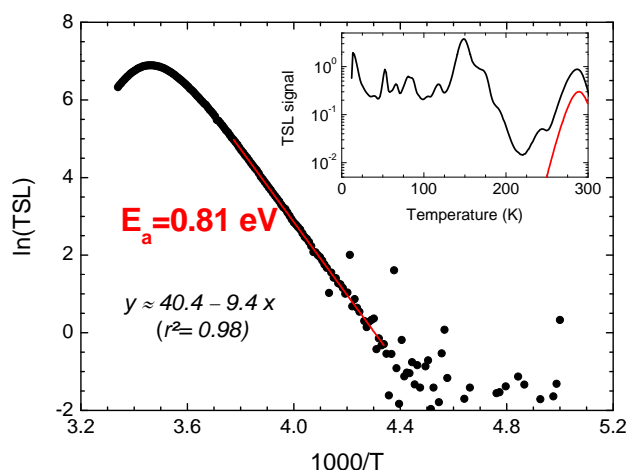
Figure 4.7: Partial cleaning of the 285 K peak.

From the rise part of the partially cleaned glow curve, it is possible to estimate

the activation energy of the trap E_a. The beginning of the partially cleaned glow curve can indeed be approximated to [63]:

$$I(T) = A_0 e^{-\frac{E_a}{kT}} \quad \text{with} \quad k = 8.62 \; 10^{-5} \; \text{eV.K}^{-1} \tag{4.1}$$

An Arrhenius plot, such as the one provided in Figure 4.7, is a convenient way for estimating the activation energy E_a. The activation energy of the trap leading to a maximum of emission at 285 K was found to be around 0.80 eV.

From the trap energy it is subsequently possible to compute the frequency factor and the lifetime of the trap. If we assume the kinetics of the charge recombination to be of order 1, the frequency factor is given by [63]:

$$S = \beta \frac{E_a}{kT_m^2} \exp\left(\frac{E_a}{kT_m}\right) \tag{4.2}$$

where T_m is the peak position and β is the heating rate.

From the frequency factor, the lifetime of the trap τ can also be computed through [63]:

$$\tau(T) = \frac{1}{S} \exp\left(\frac{E_a}{kT}\right) \tag{4.3}$$

The trap responsible for the TSL peak at 285 K, has a resonance factor of 1.5 THz which in turn lead to a lifetime at 25°C of around 30 s. It is noteworthy that this estimation of the lifetime is rather strongly dependent on the temperature, as shown in Figure 4.8.

For applications in calorimetry, this meta-stable trapping of charge carriers is too long to lead to a signal collection in a time windows of typically hundreds of ns. This results into a non-negligible amount of afterglow (carriers trapped are released during next runs).

In the frame of this thesis, we did not investigate all the peaks present on the glow curves. Other studies [67, 68] led to the computation of lifetimes of some other peaks. In Figure 4.9 the values computed at 25°C are displayed close to their associated TSL peaks. On the graph, the values labelled with ♣ and ♠ are
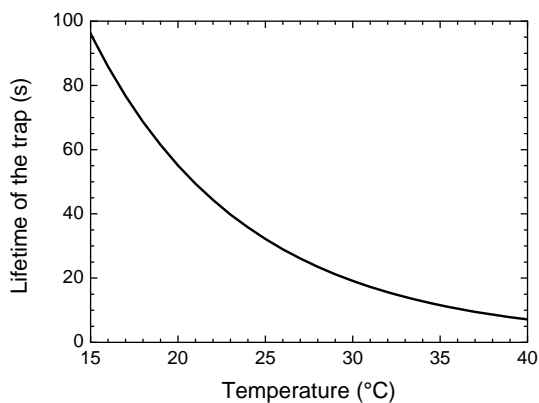
Figure 4.8: Illustration of the temperature dependence of the trap lifetime.

from [67] and [68] respectively.
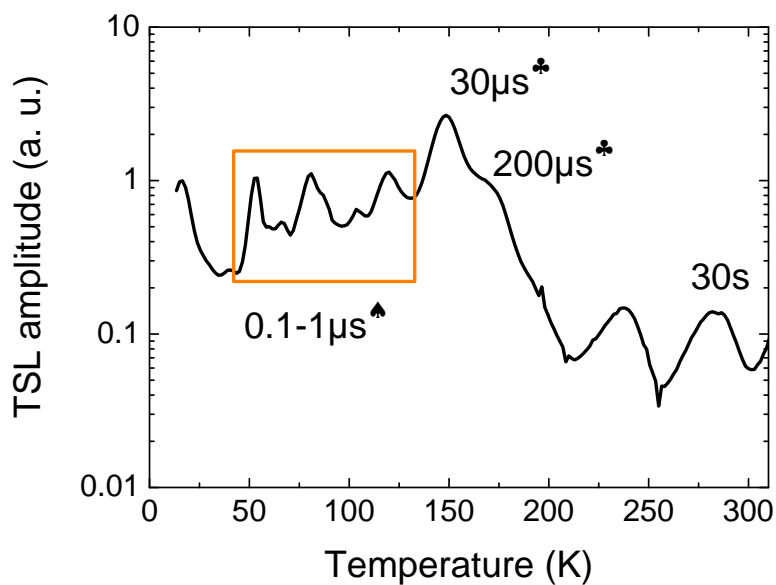
Figure 4.9: Estimation of the trap lifetimes corresponding to the TSL peaks observed below room temperature.

4.1.6 Sample to sample comparison

Since the TSL peaks described above are visible on the glow curves of all samples, we can assume that the traps are very likely to be present in all and that only their concentration is changing from one sample to another. A change in the TSL peak intensity would then reflect a change in concentration of the trap responsible for this peak.

In Figure 4.10, the glow curve are superimposed in order to allow direct comparison of the intensities of the peaks. We selected a linear scale in order to make the changes in intensities more readable. The total intensity of the glow curve is dependent on a few parameters, for instance: time of irradiation, exposure of the CCD, size of the sample. The peaks of the glow curves can then only be compared relatively to the others. On the graph provided, the curves were indeed normalized in an arbitrary way. In an attempt to guide the understanding of the contribution of the TSL peaks to the luminescence process, we provided some scaling factors for the lifetime (at room temperature) of the traps.
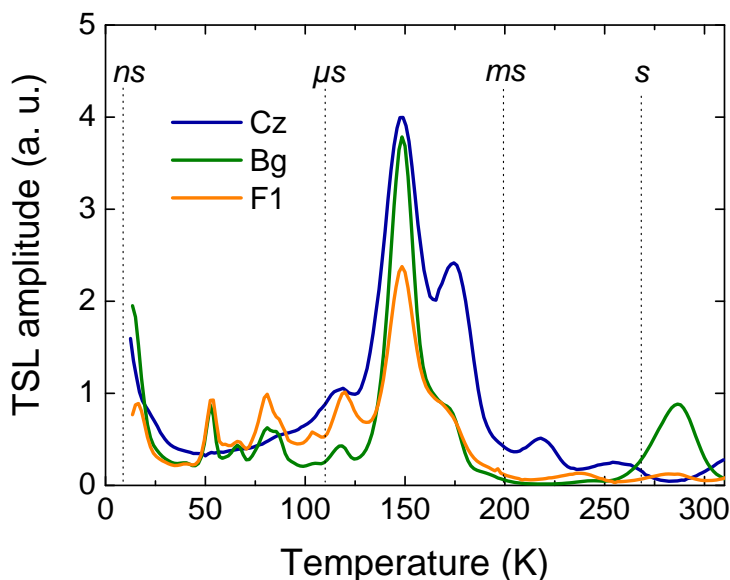
Figure 4.10: Glow curves below room temperature for four different LuAG samples.

The consequences of the traps on the emission of light in the scintillating crystal depends on its lifetime. On the glow curve, we previously distinguished three regions: $T < 120$ K, $120 < T < 200$ K and T$>$ 200 K. These regions do not have the same impact on the scintillation.

From 10 to 120 K The lifetimes of the traps emptied below 120 K are expected to be faster than 1 μs. They are very likely to be responsible for the slow component of the scintillation light presented earlier. In order to verify this, we measured the scintillation decay curve of samples Cz, Bg and F_1. The measurements were performed in two configurations: we first integrated the entire spectra of emission and in a second measurement, we acquired the decay curves with an optical filter only selecting photons emitted by the Cerium sites. These measurements were done in collaboration with P. Martin from CELIA in Bordeaux, France.

In Figure 4.11, these two decay curves are provided for sample F_1 (black and green curves). In addition, it is possible to determine the contribution of the intrinsic luminescence to the decay curve by subtracting these two curves (we then obtain the blue curve). Along the same line, the amount of intrinsic light re-absorbed by the Cerium sites can be estimated as well (orange curve).

We applied this approach to the three samples in order to be able to compare the timing properties of each contributor. The contour plots (Figure 4.4) tend to show that the TSL peaks are most probably not related to Cerium sites. For this reason, we decided to focus on the contribution of the intrinsic light. The intrinsic component of the decay curves obtained are provided in Figure 4.12.

The glow curves (presented in Figure 4.10) revealed the presence of a peak at 80 K which was estimated to have a lifetime between 100 ns - 1 μs. For samples F_1 and Bg, this peak was clearly visible, but it was absent from the glow curve of the sample grown by Czochralski. This observation is in agreement with the timing profiles presented in Figure 4.12. In the 100 ns - 1 μs range, the sample grown by Czochralski has indeed a different behavior as compared to other samples. This decay component, absent on Cz, was estimated to be around 600 ns.

Although of high interest, the exact decomposition of the decay curves into the respective contribution of the traps measured in TSL appears very complex.
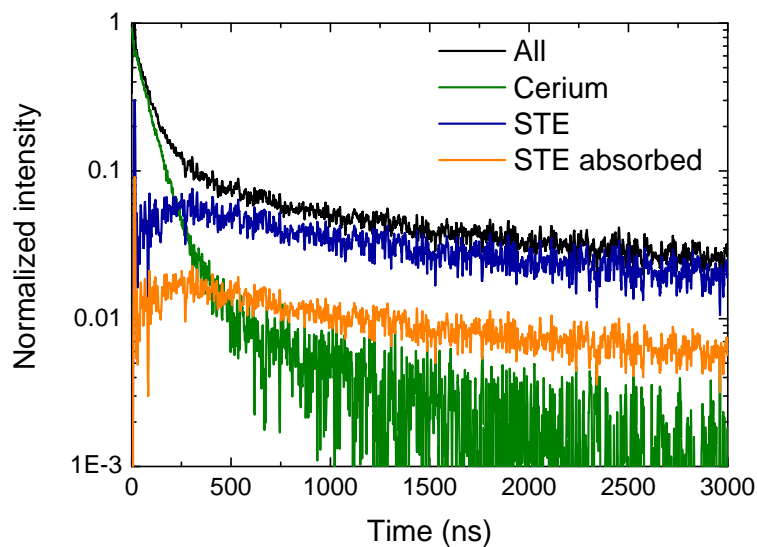
Figure 4.11: Decomposition of the scintillation decay curve of sample F_1 into three components caused by different recombination processes.
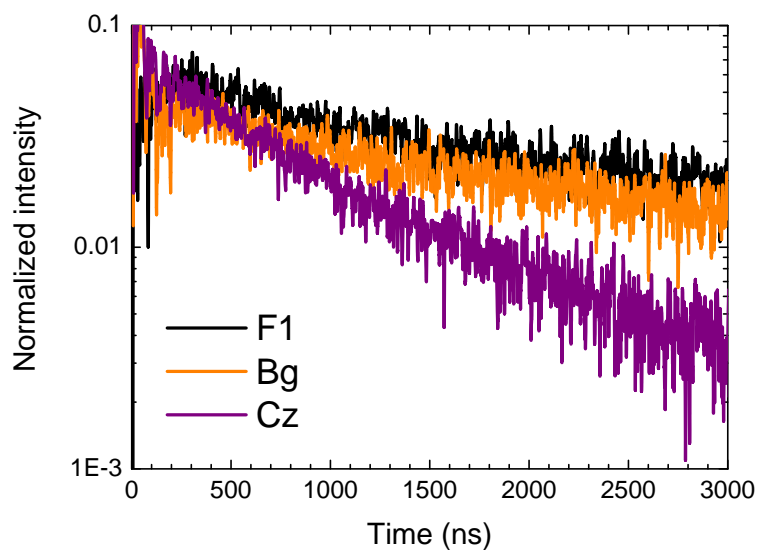
Figure 4.12: Timing profile of the intrinsic scintillation for samples grown by either μPD (F_1), Bridgman (Bg) or Czochralski (Cz) techniques.

Multiple peaks are indeed observed in the 10 - 120 K region. As a result, this slow light is actually expected to show a complex multi-component decay. This explains the difficulty to fit the decay curves measured experimentally. Some studies were based on three [69] or five [50] exponentials. Besides, since tunneling is suspected to occur, some authors tried to implement a $1/t$ law in addition [39].

Nevertheless, from the direct comparison of the pulse shapes we suspect that the traps leading to sharp peaks at 50, 80 and 120 K are responsible for the slow light observed experimentally. The sample grown by Czochralski seems to have a better crystallographic structures since the intensity of the peaks is considerably lower. It is not possible to exclude the possibility that the change in the decay curve is due to a higher concentration of Cerium. At higher dopant concentration, the emptying of the traps of higher energy through tunneling effect is indeed getting more important [39]. This decreases the influence of the intrinsic light but does not exclude any slow light since the tunneling itself follows a $1/t$ law.

Suppressing the slow component of the scintillation light turns out to be particularly complex. The insertion of co-dopants in the matrix as discussed in Chapter 3 could be more accurately studied if systematic TSL measurement are performed on each set of sample.

From 120 to 200 K The traps leading to TSL peaks in this region of the glow curves (see Figure 4.10) have lifetimes in the 10 μs - 1 ms range. This light is not visible for time windows such as the one considered for calorimetry (a few hundreds of ns). Lowering the density of these traps would favor the recombination based on shallow traps and thus induce more light in the considered time window. Growth techniques favoring equilibrium in the melting zone such as liquid phase epitaxy (LPE) succeeded for instance in reducing significantly the density of these traps [70]. In the micro-pulling down technology, the size of the melting zone is not favorable to reach equilibrium. It is nevertheless not excluded that careful engineering of the band gap with help of co-dopant as in [61] would decrease the impact of these traps.

From 200 to 310 K Above 200 K, two more peaks are visible on the glow curve. The last peak visible, at 285 K, was investigated in section 4.1.5 and the lifetime

of the associated trap was found to be in the range of tens of seconds. This implies that the peaks visible in this region of the glow curve are responsible for afterglow. This type of emission, although particularly useful for some applications (light 'storage'), is of no interest for calorimetry. Detectors based on scintillators which present an intense afterglow will indeed present random counts. The photons emitted in the range of seconds cannot indeed be attributed to their original event. To confirm the presence of this afterglow, we excited the samples with X-rays (tube powered with 20 kV and 20 mA) for 5 minutes. Immediately after stopping the irradiation, emission spectra were recorded during 15 minutes. Figure 4.13 shows the phosphorescence decay curves (integrated between 450 and 630 nm) for the three samples Bg, Cz and F_1.
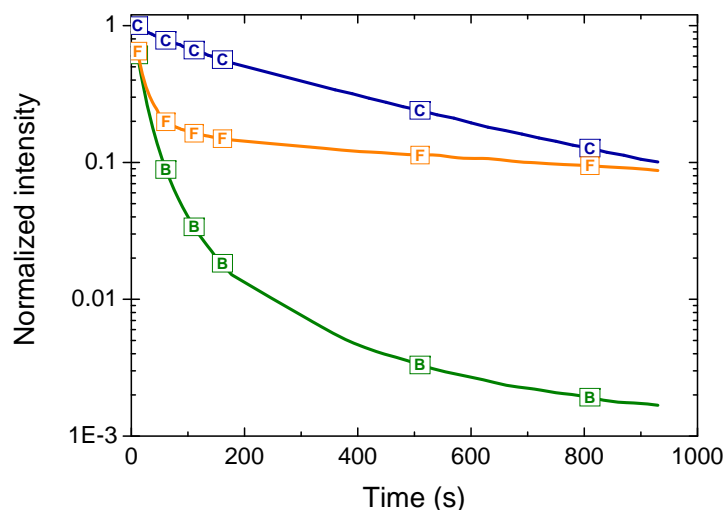
Figure 4.13: Phosphorescence decay curves of three samples grown by either μPD (F_1), Bridgman (Bg) or Czochralski (Cz) techniques.

In the first 100 seconds, the sample grown by Bridgman technique is emitting a significantly higher amount of photons as compared to the one grown by Czochralski. This repartition of the phosphorescent decay component is consistent with the relative intensity of the TSL peaks at 285 K (glow curve of Figure 4.10). The peak of the sample Bg was indeed especially higher than the one of the two other samples.

4.2 TSL above room temperature

The three samples still present a non-negligible amount of phosphorescence for times longer than 15 minutes. The extension of the TSL study to higher temperatures is an adequate tool to investigate the traps responsible for this afterglow.

4.2.1 Setup description

The setup used here is simpler than the one used for measurement below room temperature. The sample holder is enclosed in a light-tight box with a partial atmosphere of nitrogen (0.5 bar). This prevents oxidation to occur at high temperatures and ensures a good thermal contact and heat transfert. A heating plate heats the samples from room temperature to 500°C with a heating rate of 1°/s. The cooling is ensured by water flow. The luminescence photons are collected with a PMT [1]. The acquisition is thus not spectrally resolved. A band pass filter[2] centered at 400 nm was selected to allow measuring both the intrinsic and Cerium emission while reducing the black body radiations observed at high temperatures. The samples were first heated up to 500°C to empty the traps. Once cooled down, they were exposed for 1 minute to an X-Rays tube powered with 20 kV and 20 mA. A TSL scan was then performed from room temperature up to 500°C.

4.2.2 Glow curves

The glow curves are provided in Figure 4.14 for the three samples Cz, Bg and F_1, as well as for the undoped sample F_0. As for the TSL below room temperature, we provided on the graph some estimation of the order of magnitude of the trap lifetimes (at room temperature). Between 30°C and 100°C, an intense peak is observed for the samples grown by Czochralski and μPD. This peak is noticeably lower for the sample grown by the Bridgman technique. The estimation of the lifetime of the peak indicates that this difference in between samples should be visible on the phosphorescence curves displayed earlier.

---

[1]Model 9635QB from THORN EMI
[2]BG 12
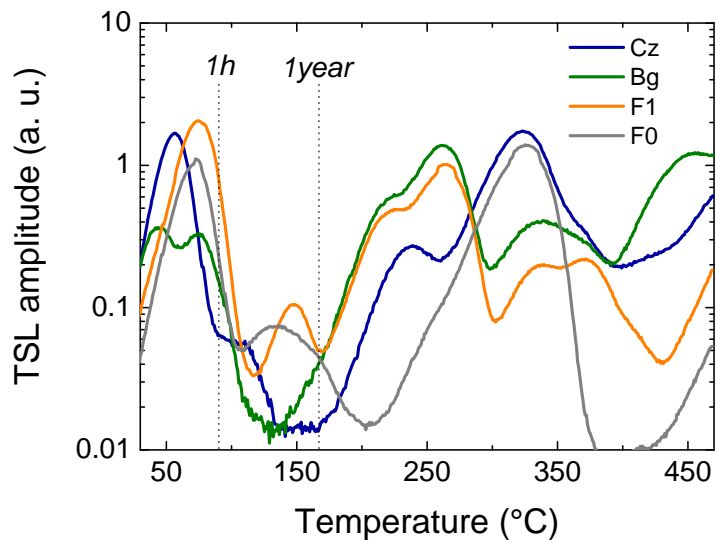
Figure 4.14: Glow curves above room temperature for four different LuAG sample.

We fitted the phosphorescence data with three exponentials. The decay parameters are plotted versus their relative weight in Figure 4.15. We observe that the relative intensity of the last component ($\approx$ tens of minutes), is consistent with the relative intensities of the TSL peak observed around 50°C.
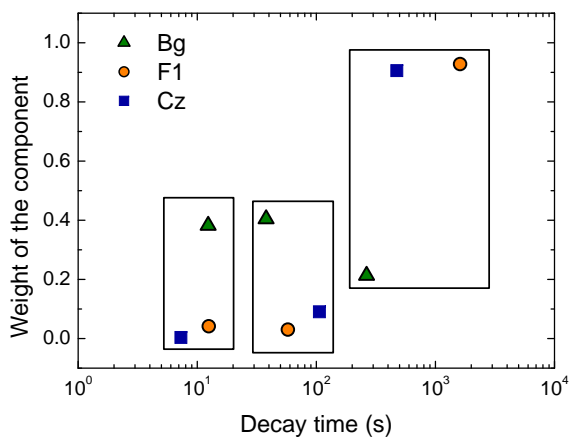
Figure 4.15: Relative weight and time constant of the phosphorescent decays.

On Figure 4.15, we observe that the relative weight of the first component (~ 10 s) is significantly higher for sample Bg whereas the last component is significantly lower as compared to other samples. Such proportions are observed on the glow curve for the peaks at 12°C (285 K) and 50°C. This confirm the assumption that these peaks are very likely to cause the afterglow observed experimentally. The second component ($\approx$ few minutes) is not accurately seen on the glow curves. The peak most probably occurs at temperatures close to room temperature and cannot be resolved with the setup used here.

Above 100°C, intense peaks are visible on the glow curve (see Figure 4.14). These peaks are not expected to play a role in the light emission process (the time constants are too large). They might play a role in the radiation hardness of the material. The peak at 150°C is especially suspected to lead to transmission losses for heavy radiation doses. Since this peak is higher for samples grown by micro-pulling down, these samples are expected to show higher radiation damages. On the contrary to the samples grown by Czochraslki and Bridgman, no annealing treatments were performed after the growth. Such treatments could actually improve these properties.

This finishes the chapter focusing on the intrinsic differences observed on LuAG samples grown by different techniques. The Czochralski process was expected to lead to the production of crystals with higher matrix quality. We showed that these samples turned out to have a faster scintillation decay. On the other hand, the afterglow was proven to be significantly better on samples grown by Bridgman. The size of the melting zone is thus not the only relevant parameter to be considered. The micro-pulling down technique, is *a priori* less favored from the point of view of matrix quality. Progress made in the suppression of the slow component and the after glow, as well as the improvement of the radiation hardness could however benefit to this technique as well. Even with lower crystal quality, the decisive advantage of μPD stays the direct production of fiber-shaped crystals. Such peculiar geometries are nevertheless very likely to significantly affect the propagation of the light. The next chapter therefore studies the effect of narrowing down the section of the crystals on the propagation of the light.

Chapter 5

Light propagation in fiber-shaped crystals

The concept of dual-read out presented in this thesis is based on scintillators shaped into fibers. For such a geometry, the propagation of the light is an important parameter to insure a good collection efficiency. Therefore we will study in detail the effect of narrowing down the section of the crystals. The content of this chapter has been published in [71].

5.1 Light propagation in crystals

Light propagation in scintillating crystals and especially the effect of the aspect ratio in the light collection was studied in earlier works. Most of these works were related to positron emission tomography (PET) systems oriented towards specific applications where high spatial resolution was required [72]. For these PET systems designed for small animals [73] and breast cancer imaging [72, 74], the size of the scintillators was therefore reduced down to a section of 2×2 mm^2. Surface effects, wrapping conditions and optical coupling were progressively optimized [75, 76, 77] and it was shown that, for such dimensions, provided the crystals present a good surface finish, the aspect ratio has little effect on the light collection [78].

When longer crystals are being considered, this effect is however no more negligible [79, 80, 81, 82]. To extend earlier publications to the peculiar aspect ratio considered for this project, we based our discussion on a set of crystals having a constant length (equal to 20 mm) and variable sections from 5.2×5.2 mm² to 1.4×1.4 mm². We also studied the importance of the surface finish on the light collection, as well as the influence of optical coupling and wrapping conditions. The experimental study is completed with Monte-Carlo simulations aiming at understanding the light losses observed.

5.2 Experimental procedures

5.2.1 Samples description

Since, in this chapter, we only study the changes induced by specific geometries, we selected a set of samples of Cerium-doped Lutetium oxyorthosilicate (LSO) instead of LuAG. This widely used scintillator presents indeed, in addition to a high light yield, an emission spectrum close to the quantum efficiency of standard PMTs. This thus increases the photostatistics, which is of special importance when dealing with samples of small section.

In order to minimize the effect of sample to sample fluctuations (differences in doping concentration, bulk quality, etc), the study was based on a large $(10\times20\times20\text{mm}^3)$ crystal of LSO. The top and bottom faces (section of $10\times20\text{mm}^2$) were polished mechanically using diamond grit. The final polishing stage was performed with 3 μm grain size. The crystal was then cut with a wire saw perpendicularly to the polished faces into sub-crystals with uniform length of 20 mm but various sections as described in Table 5.1. Each of the sub-crystals was subsequently polished starting with the big side (for asymmetric crystals). The second side to be polished was either adjacent or opposite (details given in Table 5.1). For crystals with three sides polished, the remaining unpolished side was the small one (in case of asymmetric crystals).

Width 1 (mm)	Width 2 (mm)	Average (mm)	Length (mm)	Polishing order
1.35	1.45	1.40	20.00	Adjacent
2.25	2.25	2.25	20.00	Adjacent
2.20	2.50	2.35	20.00	Adjacent
2.65	2.90	2.77	20.00	Adjacent
4.20	4.20	4.20	20.00	Opposite
4.25	5.20	4.70	20.00	Opposite
4.25	5.60	4.88	20.00	Opposite
5.20	5.20	5.20	20.00	Opposite
4.20	10.0	6.48	20.00	-
5.20	10.0	7.21	20.00	-
10.00	20.0	14.14	20.00	-

Table 5.1: Geometry of samples.

5.2.2 Light output measurements

The light output of the crystals was measured by coupling one of the initially polished faces to a PMT. Four different configurations were used for each sample: with/without wrapping and with/without optical grease. We used Teflon tape as a wrapping and silicon grease for optical coupling. Scintillation light was generated with a radioactive source (Cs^{137}) placed a few centimeters above the crystal so that the position of gamma rays emission stays the same and that they encounter the same length of material (20 mm). A mask was inserted around the crystal exit face in order to only detect the light exiting from this face. This prevents light from the lateral faces to reach the detector.

Since the γ-rays of the source were not tagged in time, the signals are acquired indifferently from the pulse resulting from the detection of the Cs^{137} source and from the detection of the natural radioactivity of the Lutetium. For the biggest samples, this Lu background becomes critical and it is necessary to properly subtract it in order to obtain accurate values of energy resolution (see Figure 5.1). In the absence of radioactive source, a broad region with energies up to 1017 keV is observed. This energy comes from three γ photons emitted simultaneously with the beta particles of Lu^{179} as described in [83]. Charge spectra were therefore acquired with and without radioactive source for the same acquisition time and the Lu^{179} background was removed off-line.
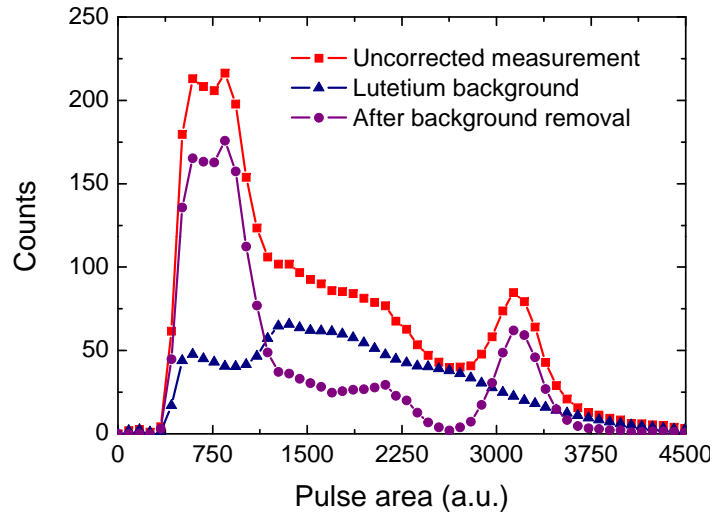
Figure 5.1: A 662 keV charge spectra of a typical LSO crystal as measured by the digitizer, the corresponding Lutetium background measured without the source and the pulse-area spectra after correction.

5.3 Experimental results

After correction for the Lu background, we extracted from the pulse area histograms the position and width of the photopeak. Since the set of crystals are from the same region of the ingot, we can assume the photo-conversion processes to be the same in all samples. Only selecting photoelectric events allows us then to consider the amount of photons generated in the samples to be constant. Since the γ-rays originated from the same location, their interaction path in the material is not significantly affect by the sample geometry. A change in the light output from sample to sample can therefore directly be imputed to a change in light propagation and/or collection in the crystal.

Figure 5.2 shows the variation of the light output and energy resolution as a function of the average width of the crystals. Since some of the samples were not strictly square, we define the average width as the square root of the area coupled to the detector. The plots present the data acquired for each crystal, measured in the four configurations described earlier (crystal naked, crystal naked with optical grease, Teflon wrapped crystal, Teflon wrapped crystal with optical grease).
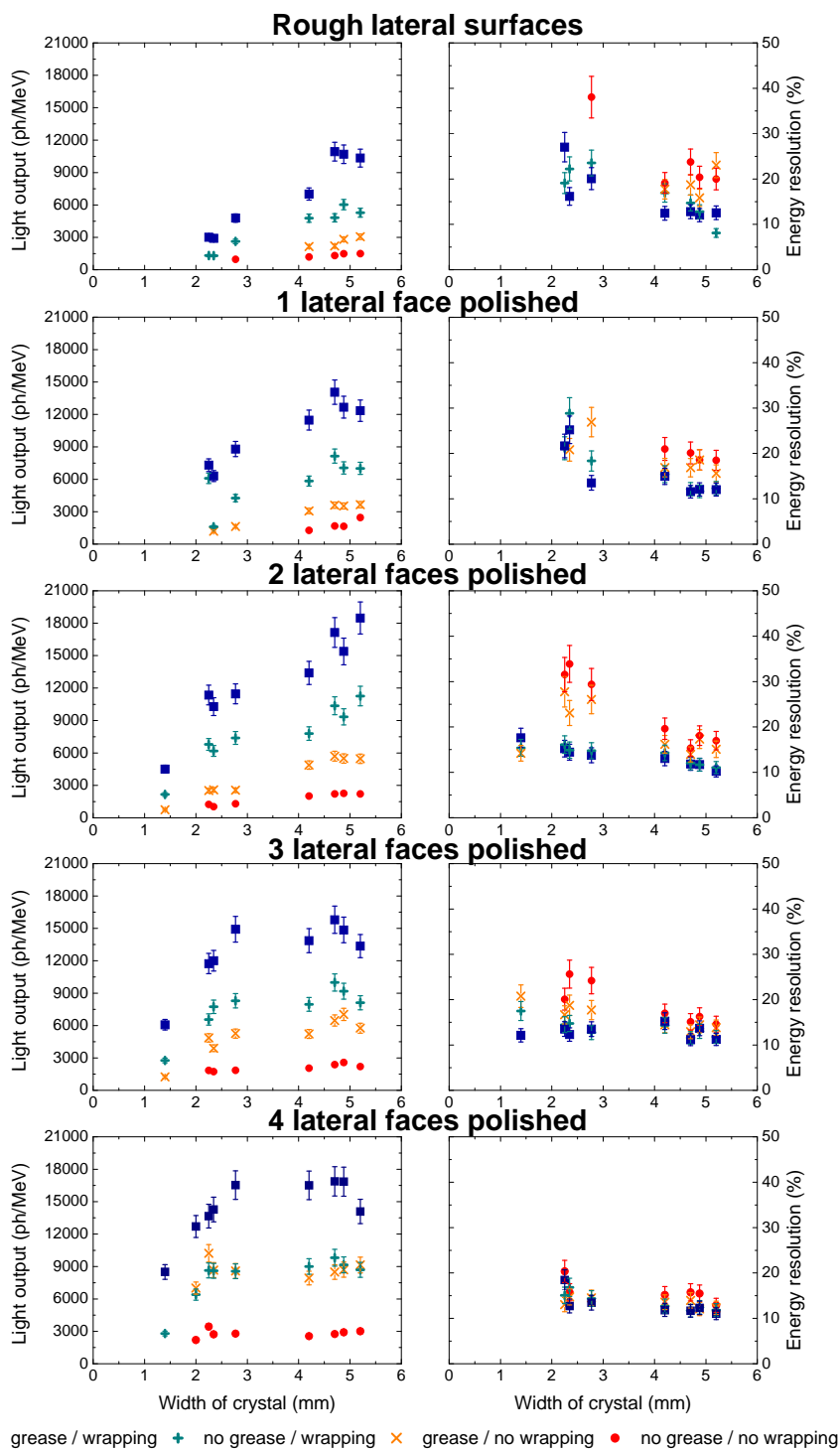
Figure 5.2: The light output (normalized to the γ-rays energy) and the energy resolution for the different samples with various surface textures measured with/without optical grease, with/without optical wrapping.

We remind here that the top and bottom faces (respectively opposite to the detector and in contact with it) are polished in all cases. The lateral faces were polished step by step: from no lateral face polished (top graphs) to all lateral faces polished (bottom graphs).

As expected the samples with rough lateral faces show an important decrease of the light output as the section of the crystal is decreased. A light yield of 3 000 ph/MeV was measured for a $2.25 \times 2.25 \times 20 \text{mm}^3$ unpolished crystal wrapped and coupled to the detector with optical grease whereas an unpolished crystal of $10 \times 20 \times 20 \text{mm3}$ measured under the same conditions had a light output of 18 000 ph/MeV (data not displayed on the figure). We see that the energy resolution is significantly poor if no wrapping is used. Furthermore, small samples did not show any distinguishable photopeak in the light spectra. Losses occurring when the photons interact with the rough surfaces explain this partially. We also note that, when wrapping and optical grease are used, polishing 3 or 4 laterals faces does not notably improve the light collection, as compared to the samples with two lateral faces polished. Furthermore, the three thickest samples present the best light collection with only two faces polished. However, without wrapping, as expected, polishing the third and fourth faces leads to better results also in energy resolution.

In order to emphasize the effect of optical grease and Teflon wrapping on the light collection, we plotted in Figure 5.3 the relative gain observed for each of them. This light gain is simply defined as the ratio of the light output for a given crystal measured in two configurations. Since heavy inorganic scintillators have a high refractive index (1.82 for LSO) the extraction cone in air is narrow (33°). Therefore coupling the crystal to the detector with optical grease (n=1.41) allows increasing the cone to 51°, which leads to a better light collection. Experimentally, we observed that the light gain with optical grease is independent of the aspect ratio of the crystal. When samples were wrapped with Teflon, this light gain is also independent of the surface finish, all samples showed 180% improvement in the light collection.

By contrast, in the case of samples measured naked, the light gain with optical grease increases with the number of polished faces: from 190% to 300% for samples with 0 and 4 lateral faces polished respectively. Theoretically, in the
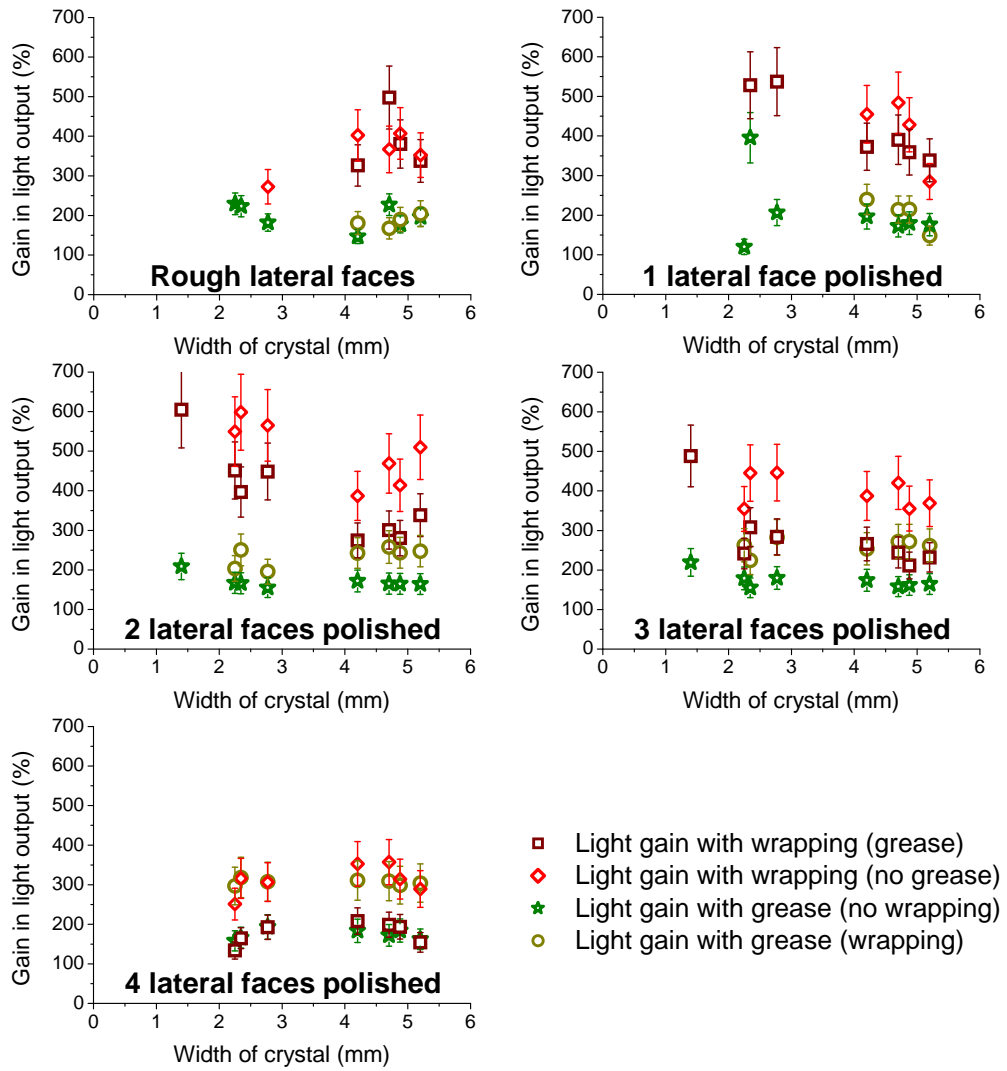
Figure 5.3: The gain in light output induced by the use of wrapping and grease (same data as in Figure 5.2 but normalized to the respective cases).

perfect case, the gain should be the ratio of the solid angles of the respective extraction cones. Since this ratio equals 2.24, two observations can be made. First, wrapping modifies the interface of the crystal because less light is collected than expected. And second, some other effects play a role in the light collection since, for a naked crystal, in which the total inner reflection is believed to be mirror-like, the light gain induced by the use of optical grease is higher than expected. It is noteworthy that the energy resolution is not significantly changed with optical grease.

The reflector aims at redirecting the light that is normally lost because it exited from a face not coupled to the detector. Experimentally, the light gain caused by its use depends on the surface finish. With rough lateral faces, a factor 3 to 4 can be gained in light output together with an improvement of the energy resolution close to a factor 2. With one lateral face polished, the light gain is highest for the thinnest crystals with an improvement of a factor 5. The light gain was even more obvious for thin samples having two lateral faces polished: e.g. 6 times more light with wrapping as compared to the naked case for the 1.4×1.4×20mm^3 crystal. This gain decreases however for thicker crystals, reaching a minimum for crystals 4×4 mm^2 cross section. Then the light gain rises again. Interestingly, the improvement in light collection of wrapping is even more pronounced when no optical grease is used. The wrapping also significantly improves the energy resolution. For crystals with 3 and 4 lateral faces polished, the light gain brought by the wrapping is lower: 260% and 210% respectively. We note that the light gain is again more important without optical grease.

In order to be able to explain these differences, it is necessary to appreciate what is changed in the light propagation when the sample has a different surface finish. Photon tracking simulation is a useful tool for achieving this.

5.4   Simulations

Simulations were run with a photon tracking Monte-Carlo program called LITRANI [84]. The crystal was simulated with optical properties fitted to the one observed experimentally (in particular attenuation length and index of refraction). In addition to the simple parallelepiped model, we designed sub-regions in the crystal in order to be able to vary locally the scattering properties of the material, hence differentiating bulk and surface features. The wrapping and optical coupling parameters were tuned to match those used experimentally as described in [54]. To establish the origin of the light collected by the detector, we saved, for each photon, its travelling time and the number of its interactions with the surfaces. The aspect ratio of the crystal has a direct effect on the light propagation since photons are encountering more reflections in a thin crystal as compared to a bulk one. Therefore the fact that we observed experimentally a strong dependence on the aspect ratio demonstrates that surface effects are of most importance in the modeling of light propagation.

In the case of a perfect crystal, it is assumed that the inner reflections occur without losses and that photons encounter no scattering. Under these conditions, the light collection is not affected by the aspect ratio since more reflections does not mean more losses. In order for the simulations to be the closest to the experimental observations, we implemented scattering in the simulations. The attenuation in the material has then two contributions, one due to intrinsic absorption in the material, one due to scattering:

$$\alpha_{att} = \alpha_{scat} + \alpha_{abs} \tag{5.1}$$

As presented in [85], it is possible to define B as the ratio between these contribution leading to:

$$\alpha_{abs} = \frac{B}{1+B}\alpha_{att} \quad \text{and} \quad \alpha_{scat} = \frac{1}{1+B}\alpha_{att} \tag{5.2}$$

The attenuation coefficient α_{att} can easily be determined experimentally. Simulations can then be run in order to find the adequate value of B. However this parameter only defines bulk scattering and as mentioned before it is highly probable that surface effects are dominating when studying the effect of aspect ratio. An ideal model that would take into account all contributions would be based on three levels of scattering: in the bulk, on the faces, on the edges. The first contribution would model the inner cracks and diffusion centers intrinsic to the material and its growth method. This value should be the same for all samples. The second contribution would model the remaining defects after polishing. And the last contribution would model the defects commonly observed on crystal edges. Obviously, while the first contribution is necessary to fine tune the model, the two others are the most relevant in the frame of this study. In order to ease the simulations we focused exclusively on the edges. This choice can also be justified experimentally. When looking closely at LSO crystals excited with UV light, the edges appear indeed especially bright (see Figure 5.4). We therefore basically assumed that no scattering occurs in the bulk of the material and that the polishing of our set of crystal was done with enough care to minimize the scattering on the faces. The only free parameter remaining is now the scattering due to the edges of the crystals.
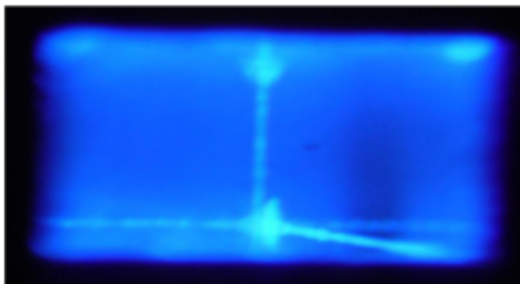
Figure 5.4: A photograph of an LSO crystal under UV excitation emphasizing the brightness of the edges.

We then reproduced in LITRANI the geometry of the samples and the different configurations in which the measurements were performed. We also defined a region around each of the twelve edges of the sample where the probability for a scattering to occur is non-zero, by contrast to the other regions of the crystals.

Edges are defined using two parameters: their thickness and their diffusivity. LITRANI has a built-in setting called diffusion length that defines a probability for a photon to be scattered after some distance in the material. Since the width w of the edges will be varied, we define the diffusivity D as follows:

$$D = \frac{w}{\lambda_{scat}} \tag{5.3}$$

With this definition, if the selected edge region is smaller, the scattering length is set lower as well in order to keep the same diffusivity. More explicitly, this means that a photon crossing a 100 μm edge where $D = 0.1$ has a probability to scatter of 9.5%. When $D = 1$, this probability becomes 63.2%.

Before estimating the value of this diffusivity it is important to determine a relevant value for the size of the edge region. Figure 5.5 plots the simulated photon extraction percentage as a function of the edge diffusivity for edges of different sizes. We simulated a 5$\times$5$\times$20 mm^3 sample wrapped with Teflon and coupled to the detector with optical grease, with all of its faces polished.
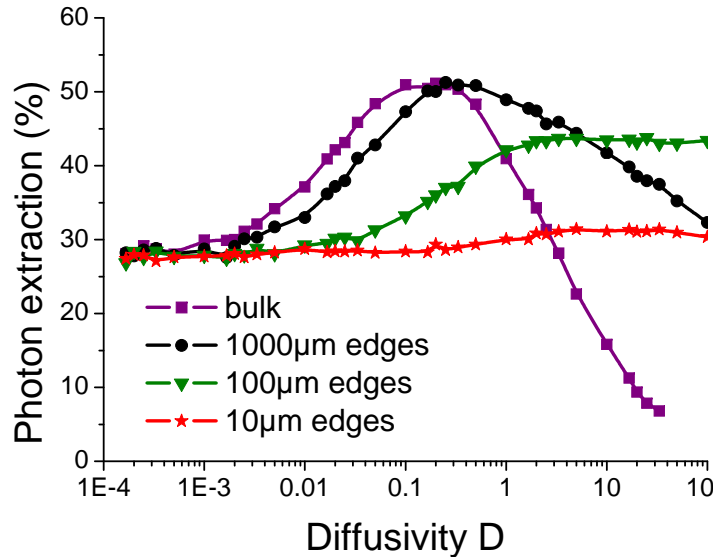
Figure 5.5: The simulated photon extraction as a function of diffusivity for several edge thicknesses.

First we observe that the implementation of scattering leads to an increase in the light output of the sample. This is easily understood by the fact that diffusion in the crystal will break the looping of the photons that were trapped in the crystal by total internal reflections. Edges of 10 μm are visibly too small to significantly modify the light propagation in the crystal (surface effect is still negligible compared to the bulk). On the other hand, for large edges, the scattering mechanism becomes close to the homogeneous case and therefore again no surface effects are visible. The relevant edges size should be somewhere in the middle and we selected of value of 100 μm. This value is confirmed with micrographs of the surface of crystals as shown in Figure 5.6.
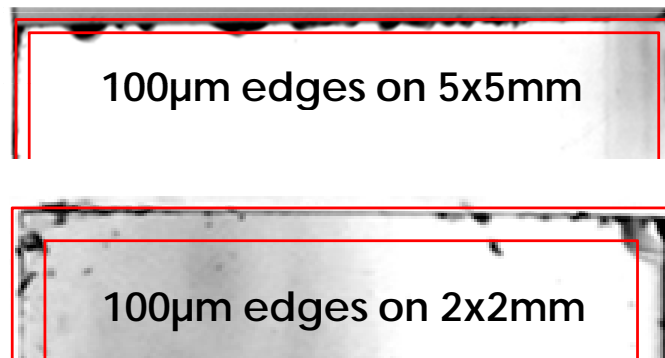
Figure 5.6: Some micrographs of $5\times5\times20$ mm^3 and $2\times2\times20$ mm^3 crystals and on-scale illustration of 100 μm edges.

The set of crystals was modeled using the same edge size for all. We could not however fix the diffusivity of theses edges since this parameter depends on the surface state of the sample and varies thus from sample to sample. In order to estimate the edge diffusivity of the set of crystals, we took profit from the fact that we measured each of them in four different configurations, leading each time to a different propagation of the light extracted. It is not possible to compare directly the simulations to the experimental results since we do not know the intrinsic light yield of the material, which means the total number of photons generated inside the material (before their extraction). It is however possible to compare two configurations, for instance comparing the light gain induced by

wrapping or optical grease. We therefore reproduced the four configurations in which the crystals were measured with various edge diffusivities and we looked for a specific value where the light gain would match the experimental data. Once the edge diffusivity thereby estimated for each sample, it was possible to obtain the light output as a function of the aspect ratio of the crystal. Figure 5.7 presents the results obtained. We normalized the light output to the number of photons generated and defined it as a photon extraction efficiency. The simulation runs were performed with a large number of photons (100 000) in order to bring the statistical error below 1%.
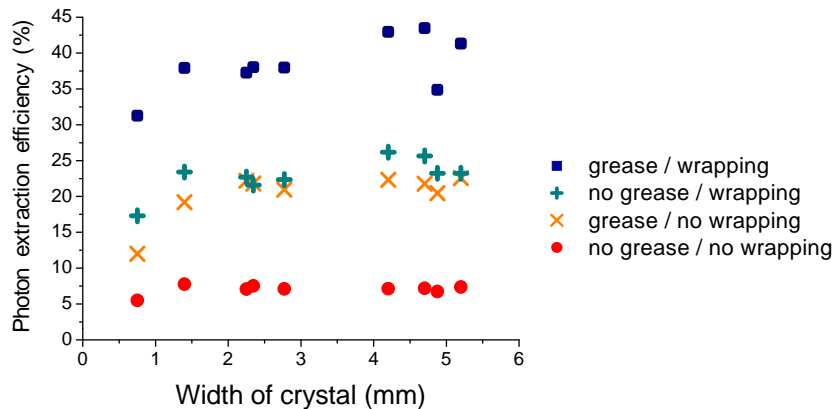
Figure 5.7: The simulated photon extraction efficiency for LSO crystals having all faces polished with/without optical grease, with/without optical wrapping.

From the graph, we first observe that our model predicts that less than 45% of the total light generated is extracted, this is consistent with earlier studies [53]. With this new model we observe a decrease in light collection as the section decreases. This decrease is however not as important as what is observed experimentally. We can give several reasons for this. Firstly, the model is most probably optimistic for what concerns Teflon wrappings. Although the diffusivity of Teflon was set properly in the simulation, a higher supplementary absorption is most probably needed. It is indeed observed experimentally that some light exits through the Teflon tape; this can be simulated with absorption in LITRANI. The crystal model used here can also be more realistic by setting two more diffusion parameters for the bulk and the crystal faces respectively. An increase in the

number of simulation parameters is however bringing the need to increase the number of independent measurements in order to be able to tune each of the parameters in a reliable way. At present, we did not succeed to find a consistent set of optical parameters in LITRANI that fit the experimental data.

The study of the influence of the section of the scintillating crystal on the quality of the light collection was started with crystals of square dimensions because they made possible the achievement of a good polishing. The idea, in the first place, was to validate the simulation tool on such a set of crystals and extend it to cylindrical or hexagonal shapes which are more difficult to produce with a fairly good surface state. Unfortunately, the simulations turned out to be, even for these 'simple' cases, much more complex than expected and they would require a non-negligible amount of time to be perfectly tuned.

We can nevertheless conclude that, even with the help of wrapping, the quality of the light propagation in a fiber-shaped material is significantly decreased for samples with poor surface states. Building highly granular calorimeters based on scintillating crystals with a high aspect ratio might then appear even more challenging since the large-scale production of such crystals with a high surface quality is non-trivial. The best quality would in principle be obtained by carefully machining bulk crystals into the desired shape. This option is however time consuming and is therefore not an option given the quantity of samples required by a calorimetry experiment.

The decisive advantage of the micro-pulling down technology is the direct production of elongated crystals which do not, *a priori*, require further machining to meet the design criteria. Characterization results of such fiber-shaped single crystals of LuAG are discussed in the next chapter.

Chapter 6

LuAG fibers grown by micro-pulling down

This chapter presents the properties of single-crystalline fibers of LuAG grown by micro-pulling down (μPD). This technology (described in chapter 4) allows growing fibers with a variety of section (square, round, hexagonal, etc). Only the cylindrical geometry was studied here. This geometry does not allow an optimum stacking but leads to samples of better quality. The diameter was fixed to 2 mm which is a good compromise between a high granularity and a reasonable number of fibers to be grown to build a prototype.

When growing single crystals, an important set of parameters have to be taken into account. Obtaining the best performances is only possible if all of these parameters are under control. This is especially true for the micro-pulling down technology since, on the contrary to traditional growth techniques, the entire crystal has to be used. Among these growth parameters, we can cite the choice of the crystal orientation (<111> here), the growth atmosphere, the design of the thermal insulation, the absence of parasitic vibrations, the pulling rate and the origin of the raw material. The pulling rate plays an important role since a compromise has to be found between a strong segregation of the dopant in the matrix due to their high mobility at low pulling rate and instabilities at the fiber surface at high pulling rate. The quality of the raw material can affect the concentration of structural defects and impurities.

A systematic study of these numerous parameters involved was initiated in the frame of an ANR project[1]. In order to keep track of all the fibers, a database listing all the growth parameters was set up. Discussing the performances of the samples during the different characterization steps was then easier and led to the identification of the parameters that significantly improve/alter the quality of the sample. To lead to an efficient characterization of the performances of the fibers, the samples were grown with lengths above 30 cm and were cut in order to form the following set of samples:

- 1 cm for estimation of the Cerium concentration in the head of the fiber
- 2 cm for estimation of the light output in the head of the fiber
- 23 cm for characterization of the light propagation
- 2 cm for estimation of the light output in the tail of the fiber
- 1 cm for estimation of the Cerium concentration in the tail of the fiber

The discussion of the results obtained will be based on the set of fibers listed in the table here under:

Fiber ID	Pulling date	Producer	Pulling rate (mm/min)	Doping (at.%)	Origin of material
F1	Dec. 2008	Fibercryst	0.5	0.1	Cz crystals
F3	June 2009	Fibercryst	0.5	0.5	Cz crystals
F1180	Nov. 2011	Fibercryst	0.5	undoped	Cz crystals
B1	Jan. 2012	K. Lebbou	0.5	undoped	Cz crystals
B8	Jan. 2012	K. Lebbou	0.5	undoped	Cz crystals
C3	July 2012	K. Lebbou	0.5	0.1	Oxydes
C4	Sept 2011	K. Lebbou	0.5	0.1	Oxydes
C5	July 2012	K. Lebbou	0.7	0.1	Oxydes
C8	Nov. 2011	K. Lebbou	0.6	0.1	Oxydes
C13	April 2012	K. Lebbou	0.6	0.1	Cz crystals
C15	June 2012	K. Lebbou	0.65	0.1	Cz crystals
C17	June 2012	K. Lebbou	0.5	0.1	Cz crystals
C18	June 2012	K. Lebbou	0.5	0.1	Cz crystals
C20	July 2012	K. Lebbou	0.25	0.1	Cz crystals
C21	July 2012	K. Lebbou	0.75	0.1	Cz crystals

---

[1]ANR project **INFINHI**, *ANR-10-BLAN-0947*.

6.1 Optical quality of LuAG fibers

A photograph of two LuAG fibers[1] is provided in Figure 6.1. From the picture, we see that both the Cerium doped and the undoped LuAG fibers can be grown with good optical quality.

Figure 6.1: Two LuAG fibers of $\varnothing 2$ mm and length 2 cm. The right sample is undoped whereas the sample on the left was doped with 0.1 at.% of Cerium.

A closer look at the surface state reveals on some of the samples a certain number of bubbles and grooves. Because of the cylindrical geometry of the fibers, imaging these surface features is not straightforward. We decided to hold the fibers vertically on a rotating table and image the surface with a microscope objective[2] coupled to a camera[3]. A ring light source[4] was placed at the bottom of the fibers, thus illuminating homogeneously the lateral surface with a grazing angle. Surface irregularities are thereby diffusing the incident light which is then visible on the pictures.

In order to image a surface larger than the surface in focus, the fibers were turned along their vertical axis. The multiple pictures acquired were then assembled as shown in Figure 6.2. The reconstructed images allow unfolding the lateral surface of the fibers. Hot colors on the images mean an important light diffusion which can be attributed to surface defects.

---

[1]Please not that, in the following, the term *fiber* will refer to a single crystalline sample grown by μPD.

[2]Melles Griot, x2.5, N.A. 0.1.
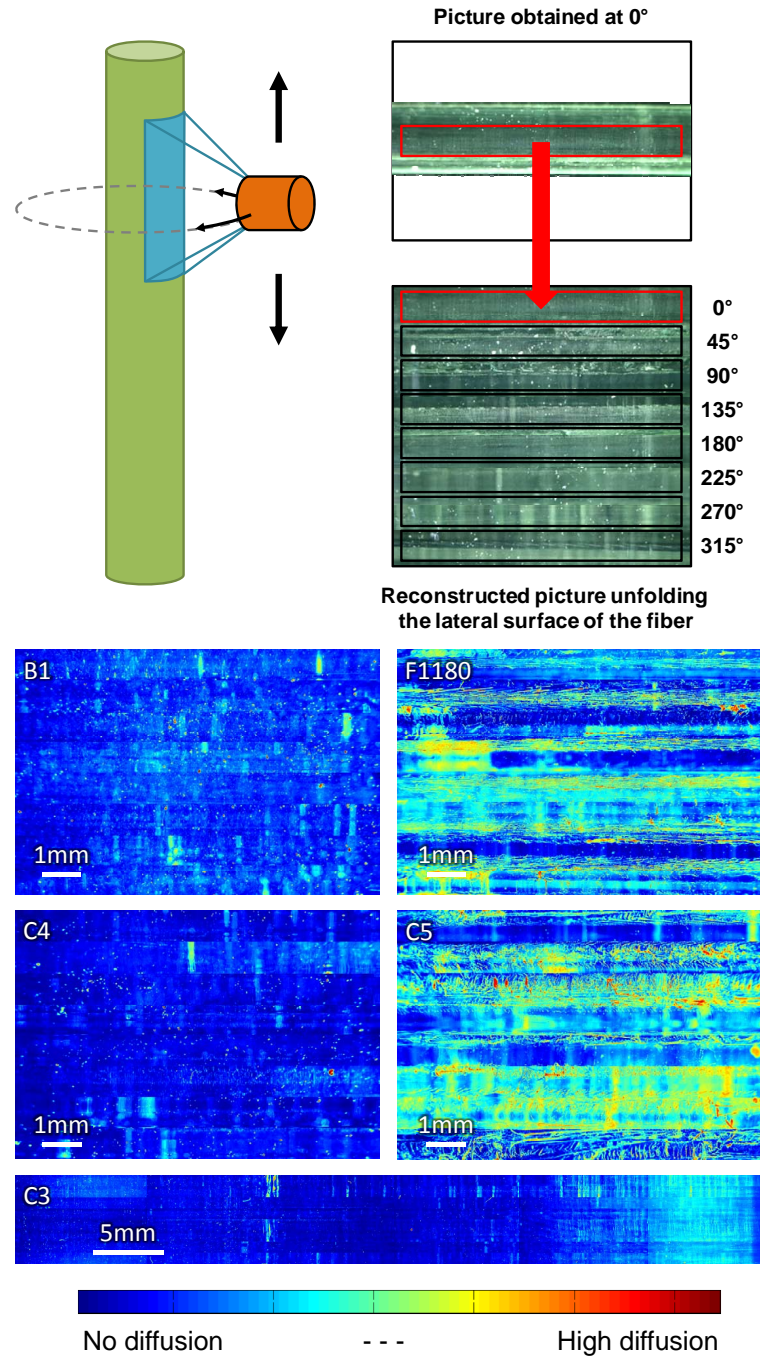
[3]Canon EOS 500D

[4]Volpi Intralux 6000-1

Figure 6.2: Setup used to image the lateral surface of the fibers and illustration of two undoped (B1 and F1180) and three Cerium doped (C4, C5 and C3) LuAG fibers.

The quality of the raw material is important, as illustrated by comparing the undoped fibers $B1$ and $F1180$. They were grown under the same conditions but the raw material did not present the same level of purity. We can also observe that, at low Cerium concentration (0.1 at.%), the doped fibers can be grown with the same optical quality than undoped fibers (as can be seen by comparing $C4$ to $B1$). The selection of an optimum pulling rate appears to be crucial to obtain high optical quality. This is well illustrated by comparing fibers $C4$ and $C5$, grown with a pulling rate of 0.5 and 0.7 mm/min respectively. On the contrary to sample $C4$, the sample $C5$ present large-scale structures on the fiber surface.

The exact origin of these surface defects is not known but we suspect background vibrations during the growth and the design of the thermal insulation to play an important role. These defects are observed at specific angles and are aligned along the pulling direction. This might be imputed to instabilities at the solid-liquid interface in delimited regions of the crucible. The last image of Figure 6.2 shows that both high quality surfaces and deteriorated ones can be observed on the same fiber but at different locations along the growth axis. The pulling direction being from right to left and the surface defects being observed on the right region, we can suspect these defects to appear as the fibers are grown. This could be explained by a perturbation that alter the quality of the interface after some centimeters of growth. It could also be attributed to a change in the doping concentration. The tail of the fiber is indeed expected to have a higher concentration of Cerium since the pulling often starts with an inhomogeneous distribution of Cerium in the melt (due to non equilibrium of the convection movements in the melting zone). The appearance of the surface defects could then reflect the fact that the Cerium concentration reached a threshold where the interface is more likely to be unstable.

6.2 Spatially resolved radioluminescence

In order to inspect the distribution of the scintillation light coming out of the fibers, we irradiated them with X-rays. The X-rays tube (40 kV, 100 μA) generates a wide (50°) beam of X-Rays which penetrate 130-160 μm in LuAG. We thus decided to aim the tube at one face of the fiber while acquiring pictures

from the other face. This ensures a nearly homogeneous excitation of the fiber (along its radius). The pictures obtained are displayed in Figure 6.3. Here again, false colors are used to enhance the contrast between the different regions of the sample. Blue and red colors represent respectively a low and a high brightness.

Pictures were acquired at different angles with respect to the exit face in order to qualitatively estimate the angular distribution of the scintillation light. The colorscale being identical for all the images, we note that the pictures of the bottom row (40° to 80°) are much more bright with respect to the picture acquired with small collection angles. It is worth noting that the brightest signal is precisely located around the surface defects. This is in agreement with the observations of section 5.4. In the case of the fibers, failing to improve their surface quality will induce a lot of cross-talk in between fibers. Most of the light exiting through surface defects is indeed almost perpendicular to the fiber axis. Wrapping or coating the lateral surface of the fibers in order to re-route these photons can be another approach.
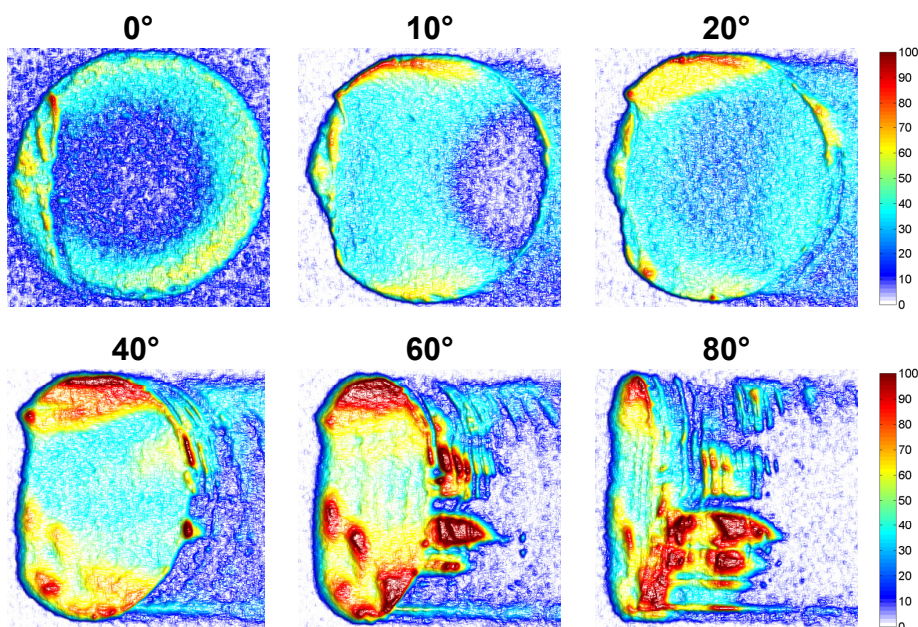
Figure 6.3: Cerium luminescence (in false colors) of fiber C3-1 ($\varnothing$2 mm, L=10 mm) grown by μPD at angles of 0, 10, 20, 40, 60 and 80°.

The first two images acquired at 0° and 10° show another peculiarity of LuAG:Ce fibers: only a very weak Cerium luminescence is visible in the core of the fibers. On the contrary, the same experiment performed on a LuAG crystal grown by Bridgman (as those studied in Chapter 3) resulted in a quasi-flat distribution of light in the crystals. This inhomogeneous distribution of the Cerium ions in the matrix is however not strictly specific to the μPD technique. As a matter of fact it is also observed on Bridgman- and Czochralski-grown ingots. The size of these crystals being however much larger, it is possible to select regions of the ingot where the concentration is *locally* homogeneous.

6.3 Cerium distribution

In order to quantify more quantitatively the radial distribution of Ce^{3+} ions along the fiber, we measured some samples with help of a confocal microscope [86]. The term confocal refers to the fact that both excitation and observation points are confocal.
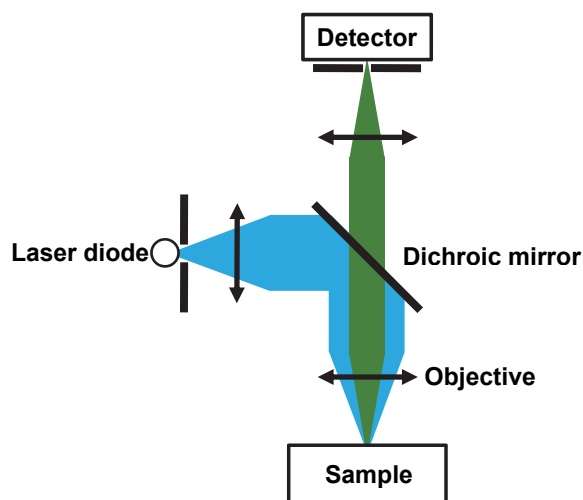
Figure 6.4: Setup description of a confocal microscope.

The light of a laser diode (473 nm) is sent on a dichroic mirror which reflects it towards a microscope objective. In the focal plane of this objective, the Cerium of

the sample is absorbing the excitation light (which wavelength was chosen to lie in its absorption bands) and a part of the isotropic re-emission is traveling back through the microscope objective. This luminescent light reaches a detector by passing through the dichroic mirror and a focusing lens identical to the one placed after the laser diode. A pinhole inserted just before this detector then restricts the regions detected to a box of a few μm^3. A confocal microscope is thus a valuable tool to probe the yield of scintillation centers in a spatially resolved way.

In order to determine the Cerium distribution of the fibers, we started by calibrating the confocal microscope with LuAG samples of known Cerium concentration. The calibration plot is provided in the top graph of Figure 6.5. The bottom plot displays the Cerium concentration (obtained with the calibration curve) as function of the radial position for two fibers grown by μPD and one sample grown by Bridgman.

As expected, the crystal ($Bg2154$) cut out of a Bridgman-grown ingot has a quasi homogeneous repartition of Cerium ions. On the contrary, the fibers grown by the μPD technique present a strong segregation of Cerium ions in the lateral surface. While the core has a concentration around 0.02 at.%, the last 150 μm contain around 0.35 at.% of Cerium. The discrepancy observed between core and rim of the fibers is also observed on fibers grown with a smaller diameter, as illustrated with sample $F3$. This fiber has a diameter of 0.35 mm and a strong distinction between core and rim is nevertheless observed.

This segregation of Ce^{3+} ions in LuAG was observed earlier [55] and it was attributed to dopant migration along the temperature gradient. The key parameter to quantify these inhomogeneities is actually the segregation coefficient k^0 of the ions in the matrix. As a matter of fact, while Ce^{3+}, Pr^{3+} and Nd^{3+} have a low k^0 in LuAG [87, 88], elements at the right of the Lanthanide group such as Ho^{3+}, Er^{3+}, Tm^{3+} [88] or Yb^{3+} [89] were measured to have $k^0 \sim 1$. This latter condition is then in general a good hint for a flat distribution of dopant in crystals. These studies showed that higher concentrations in the rim of the fiber start to be visible for Holmium and get more and more pronounced for elements left from it in the periodic table. Instead of comparing k^0 values, it is also possible to compare the ionic radius of the dopants (see Figure 6.6).
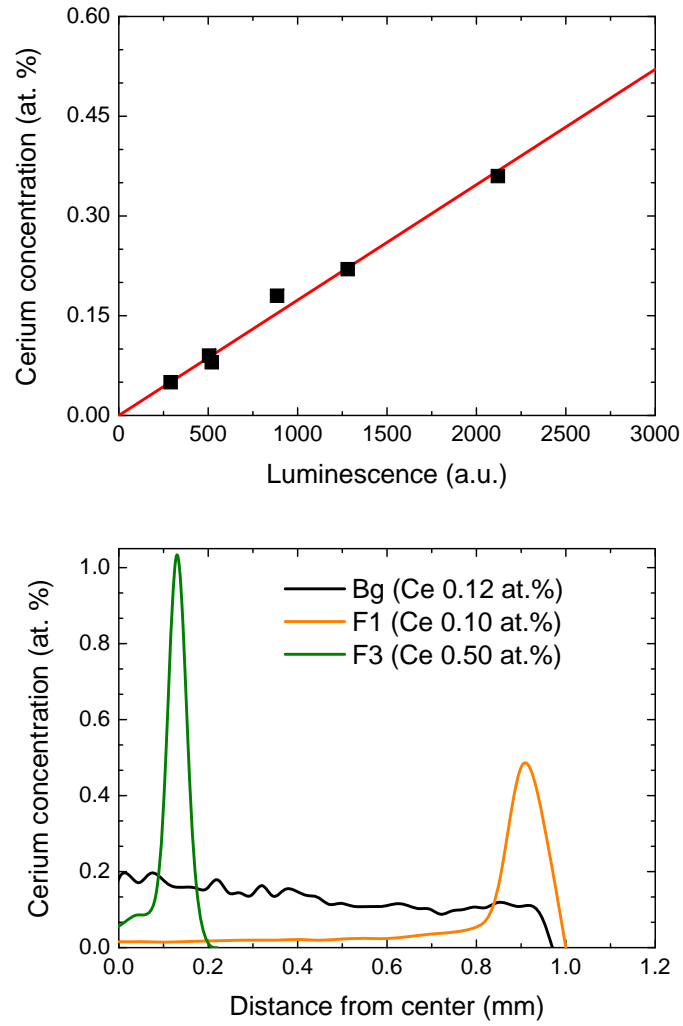
Figure 6.5: Calibration curve of the confocal microscope (top) and Cerium distribution (bottom) on samples grown by μPD ($F1$ and $F3$) and Bridgman ($Bg2154$).
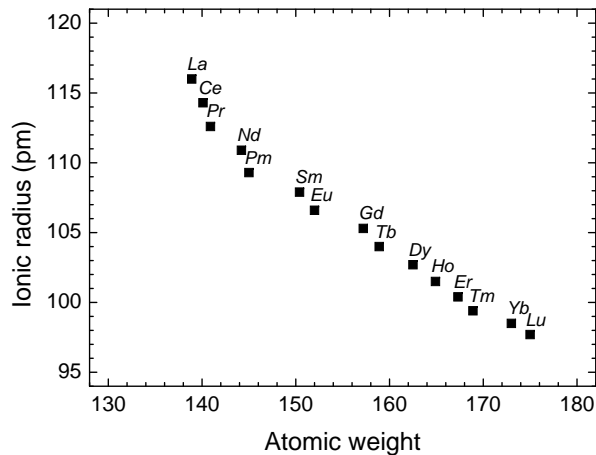
Figure 6.6: Ionic (X^{3+}) radii of the lanthanide series; values are from [90].

We observe that Ce^{3+} has the second largest ionic radius of the Lanthanide group and is thus not favored for what concerns homogeneity in doping concentration. Nevertheless, the Cerium segregation, although strongly favored from the point of view of thermodynamics, is in principle not necessarily impossible to avoid. Fine tuning the growth parameters might indeed change the kinetics of Cerium migration and possibly lead to fibers with quasi-homogeneous dopant concentrations.

In any cases, it is relevant to investigate precisely the impact of an inhomogeneous Cerium distribution. If the segregation cannot be excluded, maybe its effects can be minimized under certain conditions. In section 6.5, we will continue the discussion of this point. We will now focus on the light propagation in LuAG fibers grown by μPD.

6.4 Light propagation

In section 6.1, we showed that some of the fibers presented a significant amount of surface defects. As mentioned in the previous chapter these defects play an important role in the quality of the propagation of the scintillation light. In order to estimate the attenuation length of the fibers, we excited them at different locations with an X-rays tube (40 kV, 35 mA). A bundle of optical fibers was

dry coupled to one of the exit faces and by scanning the fibers with X-rays, the distance necessary for the luminescent photons to reach the exit face was varied and an attenuation curve could be obtained. The other extremity of the bundle of optical fibers is sent on a grating coupled to a CCD. This provides attenuation curves resolved in wavelength. The setup is described in Figure 6.7. Slits of 1 mm were positioned on the exit of the X-rays tube to restrict the area of the fiber excited.

The attenuation lengths as a function of wavelength were obtained from the spectra acquired with the CCD at different locations along the fibers. As shown on the graphs of Figure 6.7, we computed an exponential fit of the data points for each wavelength.
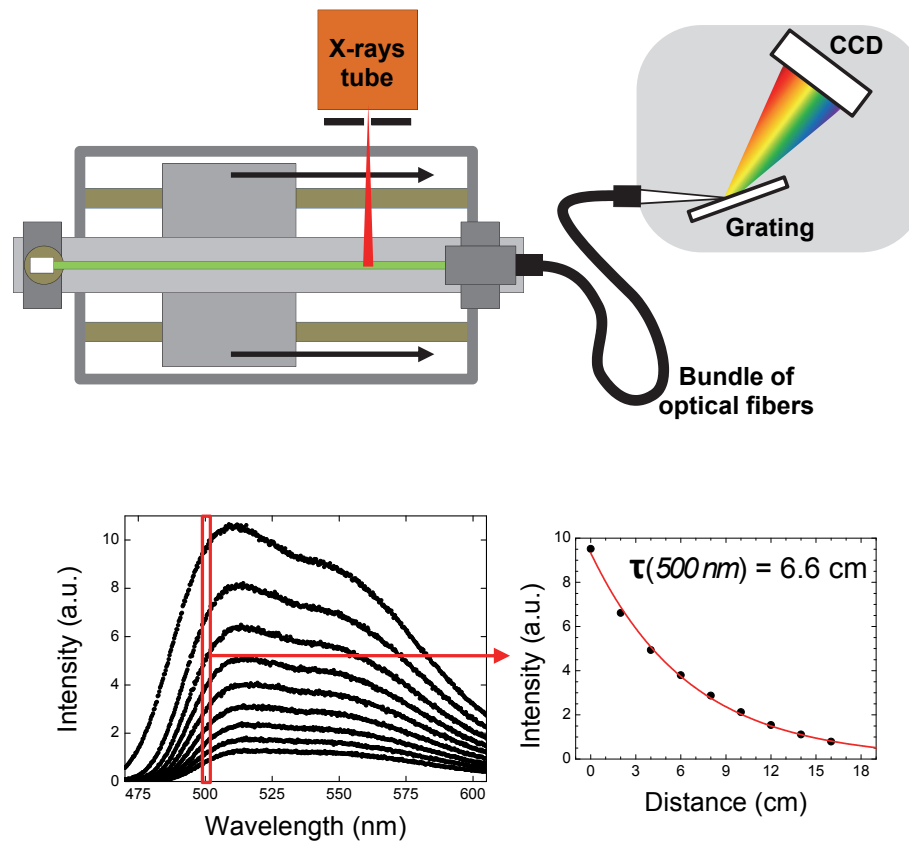
Figure 6.7: Setup for measurement of the light propagation in fibers (top) and computation of the attenuation lengths for each wavelengths (bottom).

We provide in Figure 6.8, the attenuation lengths computed for Cerium doped fibers ($C4$ and $C5$). We selected these two fibers since we saw in section 6.1 that these fibers presented a very different surface quality (C4 presented much less surface defects as compared to C5).
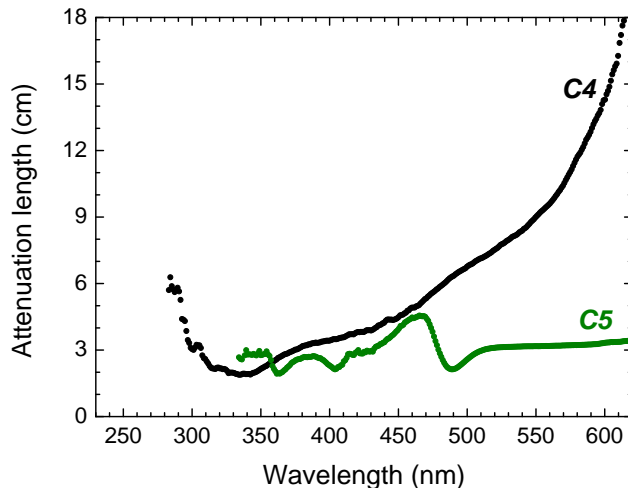
Figure 6.8: Light attenuation lengths as function of wavelength for two LuAG:Ce fibers $C4$ and $C5$.

From the figure, we note that the light is considerably more attenuated than what is observed with crystals cut out of Bridgman grown ingots. The same experiment was indeed performed on a $1 \times 1 \times 70$ mm^3 crystal of LSO and despite the smaller section, attenuation lengths reached 100 cm, which is one order of magnitude higher. Sample to sample fluctuations are in addition observed with the fibers grown by μPD. The comparison of Figure 6.8 and 6.2 bring us to conclude that a good surface state is crucial to obtain reasonable light attenuation lengths. Surface diffusion is otherwise favoring the light escape through lateral faces.

In order to estimate the attenuation length of the scintillation light, we can then convolute the curves of the Cerium doped LuAG fibers with their emission spectra. This leads to 3.0 and 8.5 cm for C5 and C4 respectively. Although a relevant fiber length for prototyping a calorimetric experiment is around 30 cm, an attenuation length close to 9 cm is affordable given the energies involved in

calorimetry. It is noteworthy that, especially for the sample $C4$, the propagation in the red end of the spectra is much better. The different choice of photodetector could then lead to different values (depending for instance on its quantum efficiency above 600 nm).
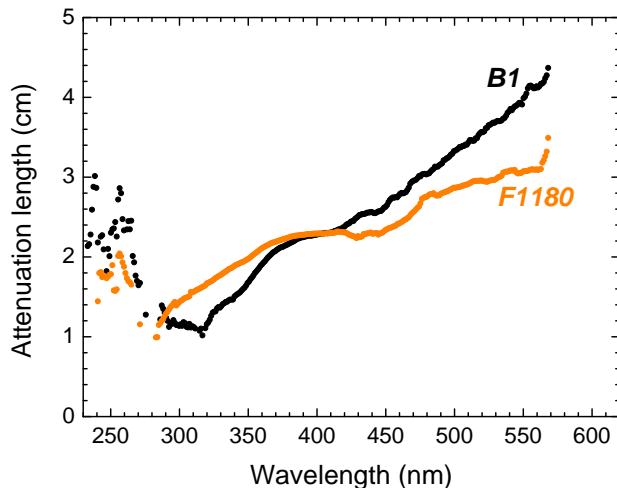
Figure 6.9: Light attenuation lengths as a function of wavelength for two undoped LuAG fibers $B1$ and $F1180$.

Figure 6.9 presents the attenuation profiles of two undoped LuAG fibers ($B1$, $F1180$) having again a different surface state. Since the undoped fibers were selected for Cherenkov light readout, the convolution has to be computed with the emission spectra of Cherenkov light ($\sim 1/\lambda^2$). This leads to surprisingly low attenuation lengths lying around 2.5 cm. This different behavior, as compared to the doped fibers, could originate from a difference in light propagation. The setup used here is indeed based on the luminescence signal. Therefore, in Cerium doped samples, the light propagation starts from the surface (where most of Cerium is located) whereas, for the undoped samples, the starting point is not restricted to this region.

Previously, we saw that parts of fiber C3 have a defect-free surface while others are covered by bubbles. We therefore provide in Figure 6.10 the attenuation curves at different wavelengths measured on this sample. We see that the attenuation curve at 520 nm (which corresponds to the maximum of Cerium emission)

is clearly presenting two attenuation regimes which certainly correspond to the different surface states observed. On the contrary, the attenuation profiles at 330 and 370 nm (originating from the intrinsic emission of LuAG) seem to be unaffected by the surface state of the fiber. The estimation of the attenuation is thus not the same at every wavelength. The current setup is therefore not, strictly speaking, a reliable estimator of the attenuation in the fibers.
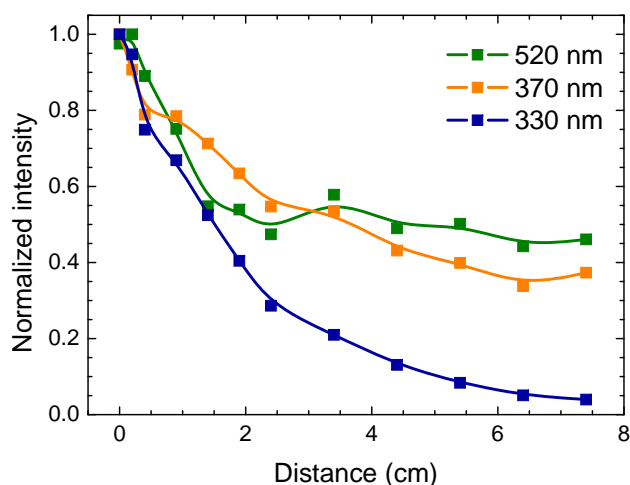
Figure 6.10: Light attenuation curves of fiber C3 for a few wavelengths.

It is worth noting that the light is collected at the exit face of the sample with a bundle of optical fibers. These fibers ($\varnothing$ =200 μm) have a numerical aperture of 0.22, corresponding to a collection angle close to 13°, which in turn corresponds to 7° in LuAG. The light attenuation measurements performed with this setup thus focuses on the photons which travel with a low number of bouncing on the lateral faces. For an isotropic source, located a certain distance away from the exit face, it is possible through, solid angle considerations, to estimate the average (most probable for a photon) number of reflections in the LuAG fiber for light rays traveling to the detector. We plotted the obtained values in Figure 6.11. This shows that even after 10 cm, most of light collected hits the surface only three times. On the contrary, if all the extraction cone is considered, this value is equal to 20 and 35 respectively for dry coupling and coupling with optical grease (n=1.41). Therefore here only a fraction of the light is effectively collected.

127
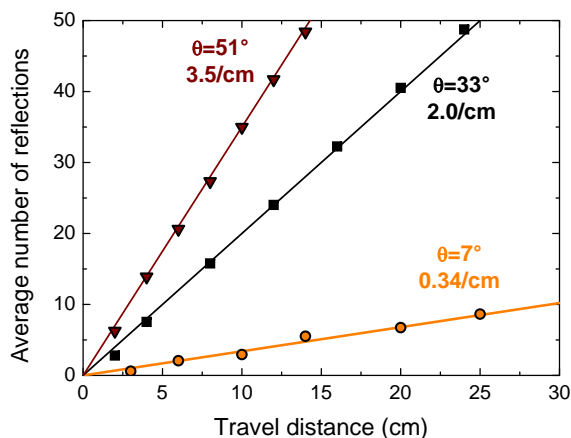
Figure 6.11: Average number of reflections involved in the propagation of an isotropic light as a function of the distance to the detector, for three different collection angles. We assumed that no losses occur upon reflection.

Besides, while wrapping or coating is very likely to improve the quality of the light propagation, the small acceptance angle does not allow its study with the present setup. The only reliable way to estimate the attenuation of the fiber is thus to measure them on the final prototype. Too many parameters are indeed very likely to significantly change the propagation of the light. We can cite the choice of detector (quantum efficiency, angular acceptance), the choice of coupling (dry contact, grease, glue or lenses), the choice of wrapping/coating (with what angle are the photons re-injected?), the energy range investigated (it will determine the radial position of the interaction).

Nevertheless, the attenuation estimation obtained with the X-rays is probably the lower boundary (worst case scenario since it favors interactions with surface defects). The upper boundary would then be a measurement of the transmission as performed in chapter 3 on LuAG crystals cut from Bridgman-grown ingots. Such a measurement leads to excellent values: no distinction is observed between Bridgman- and μPD- grown samples. This shows that the bulk of the fiber is of high quality and only the surface is likely to alter the light propagation. The effect of surface depolishing studied in the previous chapter came to the same conclusion.

Some measurements where also performed with visible light (400-450 nm). With such photons it is only possible to probe the propagation of photons emitted by the Cerium sites but it is possible to vary the excitation region from a few hundreds of microns (at 450 nm) to a few millimeters (at 420 nm). Of course, since the Cerium sites are mainly located in the rim of the fibers and that only these sites are excited, even with a large excitation region, the bulk has a minor contribution to the emission of light. The results of these measurements are provided in Figure 6.12.
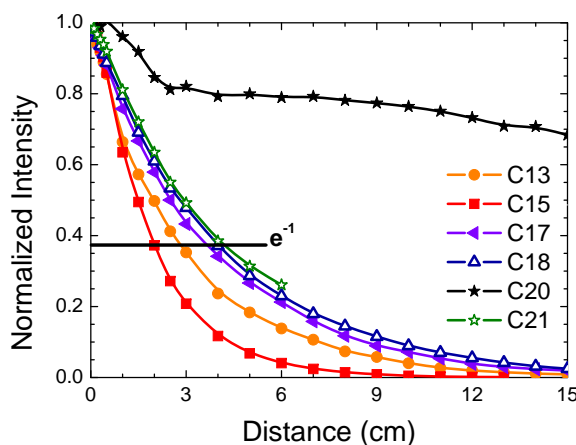
Figure 6.12: Light attenuation curves measured with 450 nm photons.

The attenuation lengths computed with this setup lead to similar values as the ones computed with the X-rays (see $1/e$ threshold on the Figure). The surface quality of the fibers measured here is indeed explaining the improvement in light propagation. On the graph, the different samples differ by their growth parameters. The producers started a systematic scan of the relevant parameters to identify the optimum ones. This approach was successful since it allowed identifying fiber $C20$, which is behaving extraordinary better than other ones, from the point of view of light propagation.

We also estimated the attenuation based on 511 keV γ-rays interactions. Such an energy favors an interaction on the entire diameter of the fibers. The results will be presented in the next section together with an estimation of the light output of the fibers.

6.5 Light output

In order to estimate their light yield, the LuAG fibers were measured with the bench presented in section 3.4 in both horizontal and vertical configurations (Teflon tape as wrapping and silicon grease as optical coupler). Due to the cylindrical shapes of the fibers, the horizontal configuration did not however lead to reliable values of the light output. The extraction is indeed too sensitive to any fluctuations in the amount of grease used and the tightness of the Teflon wrapping. On the other hand, the measurements performed in the vertical configuration, although having a reduced experimental error, led to charge spectra with barely distinguishable photopeak and Compton regions. We provide for illustration the charge spectra of sample $C8$ in Figure 6.13. The charge spectra was calibrated to the single electron response in order to allow directly reading the number of photo-electrons (phe).
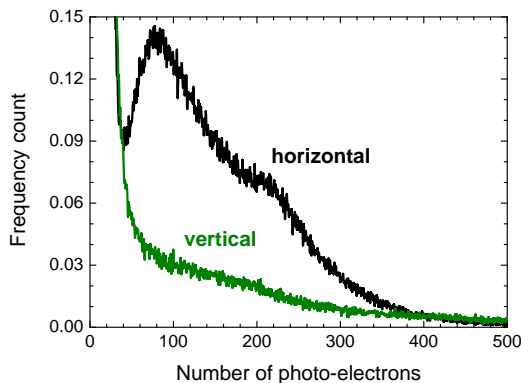
Figure 6.13: Photo-electrons distribution of a Cerium (0.1 at.%) doped LuAG fiber (sample $C8$) acquired with 662 keV γ-rays.

The Compton continuum being below 150 phe, the trigger of the acquisition chain must be set significantly low. In such a situation the noise level is increased and pollutes the left part of spectra. In addition, the right part of the spectra is affected, like in LSO, by the natural radioactivity of Lu^{179} (see section 5.2.2). On Figure 6.13, we can see that up to 500 phe are being collected. Background measurement (measurement repeated in the absence of the Cs^{137} radioactive source) however attributed this to the Lutetium activity. Since background subtraction

(as the one performed in chapter 3) becomes critical at low trigger values (very dependent on the noise level), we decided instead to modify the setup in order to use a tagging system for the γ-rays.

A convenient way to obtain a tagging of the γ-rays emission is to use a Na^{22} radioactive source. This source is a positron emitter which quickly leads to a $e^+ - e^-$ annihilation. Upon annihilation, two back-to-back γ-rays of 511 keV are emitted. By positioning a second (tagging) scintillator of adequate geometry at the other side of the Na^{22} source, it is then possible to detect one γ-ray in the sample investigated and the other in the tagging scintillator. Triggering on both scintillators can then only be attributed to the activity of the radioactive source. Both the noise and Lutetium backgrounds are thus excluded from the charge spectra. As a result, the trigger level in the measured fiber can be decreased down to the detection of a single phe.
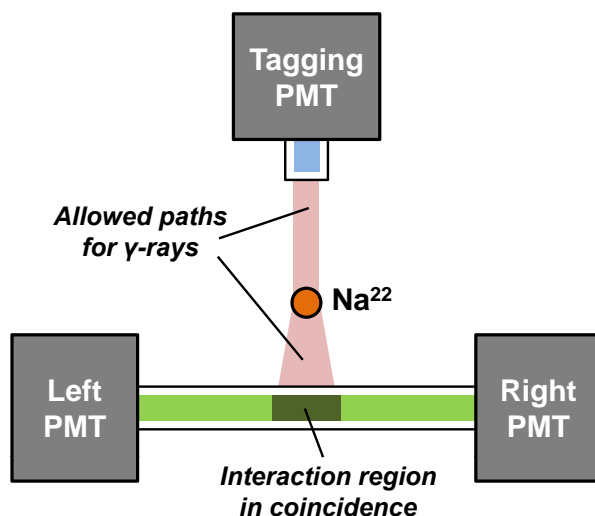
Figure 6.14: Setup for measurement of the light output of the fibers based on double readout and tagging of the γ-rays.

There is an additional factor which can degrade the charge spectra: the light attenuation along the sample. When the sample length does not ensure this attenuation to be negligible, a smeared photopeak is observed. This is due to the fact that, for a given energy deposited, the light extracted from the crystal is

dependent on the location of interaction (leading to a degradation of the energy resolution). In order to correct this effect, we decided, in addition to the tagging system, to read both sides of the fiber.

By defining x to be the position of the interaction ($x = 0$ defined as the center of the fiber), L_0 and λ to be respectively the length and attenuation length of the sample and assuming the defects to be homogeneously distributed along the fiber axis, we can express the signal of the left (S_L) and right (S_R) PMTs as:

$$S_L(x) = A_0 \exp\left(-\frac{\frac{L_0}{2} + x}{\lambda}\right) \quad \text{and} \quad S_R(x) = A_0 \exp\left(-\frac{\frac{L_0}{2} - x}{\lambda}\right) \tag{6.1}$$

By defining $X = \frac{x}{\lambda}$ and $A_1 = A_0 \exp\left(-\frac{L_0}{2\lambda}\right)$, we can re-write this into:

$$S_L(X) = A_1 \exp\left(-X\right) \quad \text{and} \quad S_R(X) = A_1 \exp\left(X\right) \tag{6.2}$$

In practice, the positions X and x are unknown and the known parameters are S_R and S_L. The relative position X can however be expressed as:

$$X = \frac{1}{2}\ln\frac{S_R}{S_L} \tag{6.3}$$

This relative position can be used to estimate the interaction point of the γ-rays. It is then possible to use it to compensate the light attenuation. Computing the constant term A_1 in equation 6.2, is actually a way to achieve this. We thus define the corrected signal S_L^{corr} and S_R^{corr} as:

$$S_L^{corr} = S_L(X)\exp\left(X\right) = A_1 = S_R(X)\exp\left(-X\right) = S_R^{corr} \tag{6.4}$$

Summing the readout on both sides then leads to:

$$S_{corr} = S_L^{corr} + S_R^{corr} = 2\sqrt{\frac{S_L(X)}{S_R(X)}}S_R(X) = 2\sqrt{\frac{S_R(X)}{S_L(X)}}S_L(X) \tag{6.5}$$

The left, right and corrected signals as function of the relative position X are plotted in Figure 6.15.
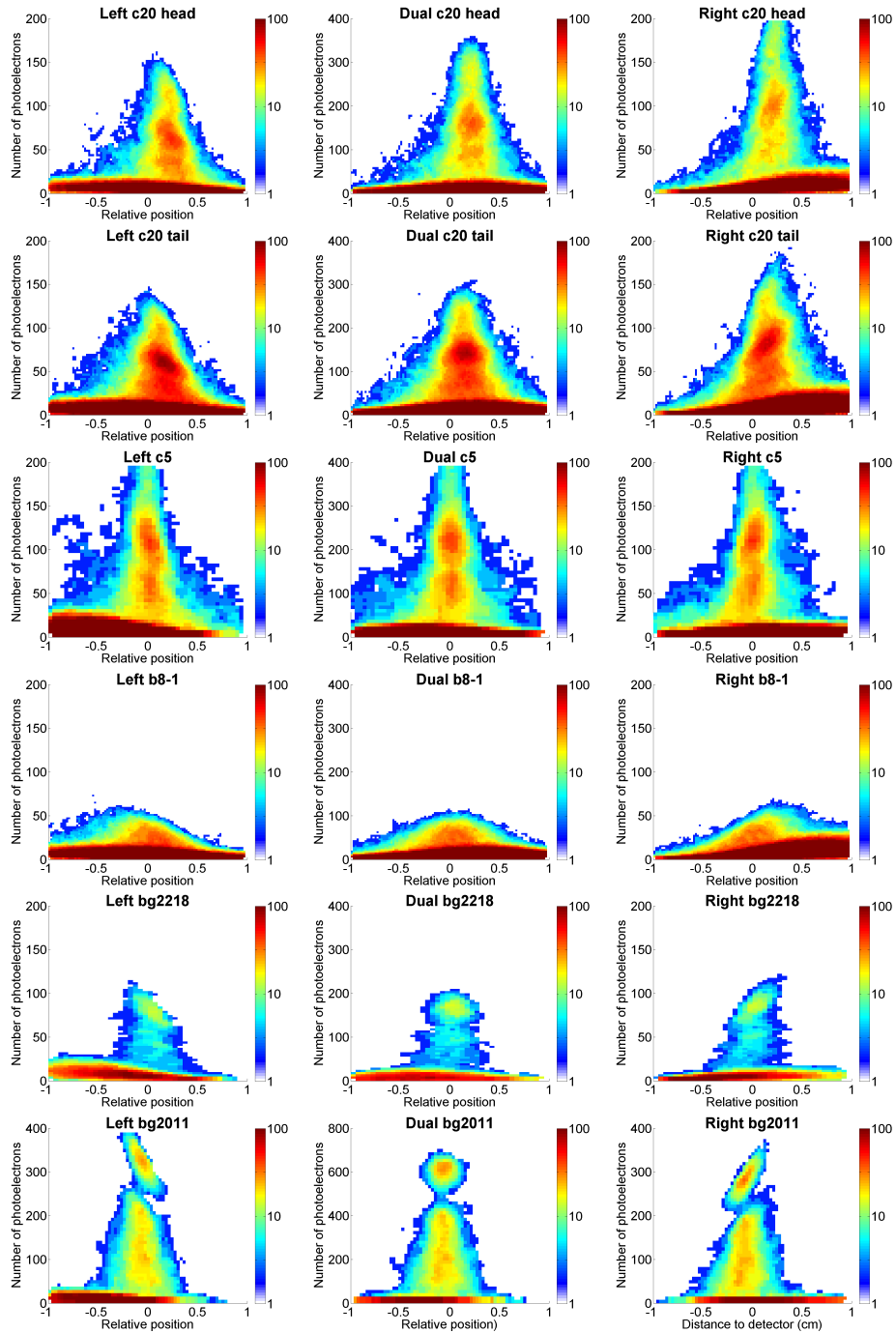
Figure 6.15: Contour plots giving the signals acquired on the left and right PMTs as a function of the relative position (expressed in attenuation lengths) of the interaction. The middle column displays the signal after correction for the attenuation (as computed from 6.5).

On Figure 6.15, the four top rows were computed on LuAG fibers grown by μPD. Samples $C20$ and $C5$ are doped with Cerium (0.1 at.%) while sample $B8$ is undoped. For comparison, the two lowest rows of Figure 6.15 provide the contour plots computed from two LuAG crystals cut out of Bridgman-grown ingots. Sample $Bg2218$ is undoped while sample $Bg2011$ is doped with 0.05 at.% of Cerium. The contour plots of the left and right signals emphasize the dependency of these signals on the location of interaction. The plots obtained after correction efficiently compensate this and all plots appear centered around the zero position which is consistent with the location of the source and the tagging system. We remind here that since the horizontal axis is expressed in terms of attenuation lengths, a wider peak (on the horizontal axis) is not necessary implying a wider interaction region. Since the source was approximately positioned in the same place for all samples, it has rather to be attributed to a shorter attenuation length.

This approach allows a fast discrimination of the signals based on their relative interaction point and the correction is simple to compute. When the light attenuation length is greater than the length of the crystal, a correction based on the sum of the left and right signals is actually as efficient but when attenuation lengths are smaller, this approach is however more accurate.

It is worth noting that this correction is normalized to the value at $x = 0$. This position, in most of the cases, corresponds to the center of the fiber. To reach the detector, the photons traveled a length $L_0/2$ in a material with an attenuation length λ. Therefore the amount of light generated in the center is higher by $\exp\left(-\frac{L_0}{2\lambda}\right)$.

It is also possible to use this correction to improve the resolution of the photo-electron distribution. We can only compute it for events originating from the interaction region in coincidence with the source. In practice this was achieved by integrating the contour plots over the width of the photopeak region. As can be seen from Figure 6.16, the samples grown by Bridgman show a well resolved photopeak (with 511 keV γ-rays) centered at 160 phe and 610 phe for the undoped and 0.05 at.% Cerium doped samples respectively.
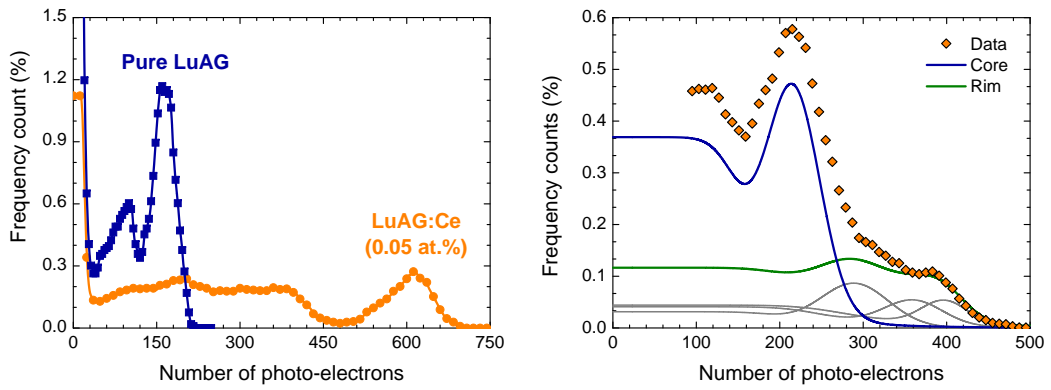
Figure 6.16: Photo-electron distribution of LuAG crystals grown by Bridgman (left) and LuAG fibers grown by μPD doped with 0.1 at.% of Cerium (right). The measurements were acquired in double readout and corrected for the attenuation in the crystals. Interactions were based on 511 keV γ-rays. The plot on the right also decomposes the charge spectra into core and rim contributions.

The same method applied to the samples grown by μPD leads also to distinguishable photopeaks for the Cerium doped fibers. Surprisingly, an extra peak of weaker intensity is also visible on these samples. We showed in section 6.3 that the rim and core of the fibers grown by μPD present a very different Cerium concentration. For this reason, the observation of multiple peaks can reasonably be attributed to these two regions. They do not superimpose because the light yields of these regions differ significantly. The phe distributions can then be interpreted as in the right plot of Figure 6.16. A Cerium emission originating from the core of the fiber which generates less light but is more frequent (in terms of number of events) and some emission coming from the rim of the fiber. The interactions in that region being less probable (dimensions in the hundreds of μm), although

the photopeak leads to a higher number of photoelectrons, its frequency count is significantly weaker. On the plot, the light generated in the rim was not fitted with a single Compton continuum and photopeak. This choice was motivated to illustrate the fact that the concentration in the rim is not constant and that instead a continuum increase of Cerium concentration is observed towards the surface.

In order to verify the homogeneity of the scintillation and optical properties along the fiber, two pieces of the original fiber $C20$ were also measured. They correspond to the head and the tail of the fiber. We observe a slight difference in the position of the photopeaks (see Figure 6.17). This shift towards a lower number of phe of both photopeaks measured on the tail as compared to the head of the fiber could be attributed to a change in light attenuation. The tail presented indeed a slightly worse surface state which in turn immediately affects the quality of the light collection.
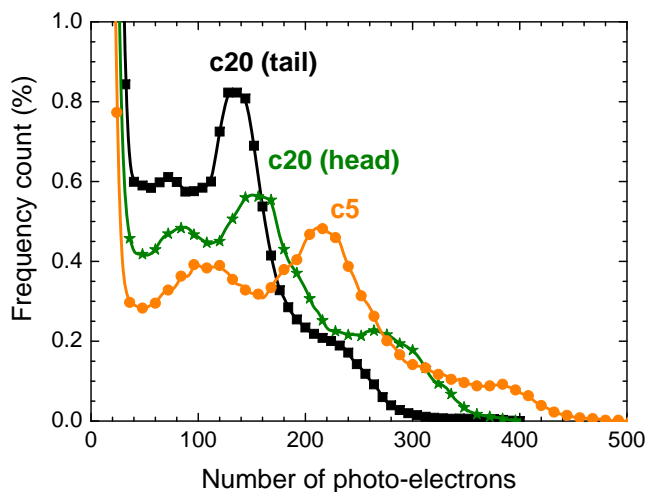
Figure 6.17: Photo-electron distribution of LuAG fibers grown by μPD doped with 0.1 at.% of Cerium. The measurements were acquired in double readout and corrected for the attenuation in the crystals. Interactions were based on 511 keV γ-rays.

The sample $C5$ was shown to have a even shorter light attenuation length. It is therefore surprising to collect more photo-electrons than $C20$. The fiber $C5$ is therefore very likely to present a higher concentration of Cerium although the concentration in the melt was identical. The explanation lies in the faster pulling rate selected for the growth of $C5$ which do not favor the equilibrium of the Cerium concentration in the melting zone.

The photopeaks of the head and the tail of $C20$ also differ in relative intensity. This can be attributed to the fact that the Cerium distribution evolves as the fiber is grown. The Cerium content in the core of the fiber gets higher as the fiber grows. It is important to remark that although, for a given energy, two significantly different values of photo-electrons can be obtained depending on whether the interaction occurred in the core of the fiber or at the surface. However this statement does not take into account the probability for each of these conversions to happen. We showed earlier (see section 6.3) that the Cerium segregation cannot be strictly avoided. A favorable situation could consist in a localization of the highly concentrated Cerium in a very narrow rim which would not be significantly visible in the eye of the detector.

Since the photopeak due to the core is more probable, an increase of the concentration of Cerium in this region is crucial to enhance the detection efficiency. The growth parameters must therefore be optimized in that direction. The tail of the fiber, for which a better equilibrium of the Cerium concentration in the crucible nozzle has been reached was already demonstrated to be of higher interest. Another approach would be to increase the Cerium concentration in the melt but the fibers grown in these conditions presented a peculiarly bad surface state which then noticeably decreases the attenuation properties.

The photo-electrons distributions obtained with the undoped samples provided in Figure 6.18 allowed us to exclude the possibility that only the intrinsic emission is observed in the core of the fiber. A distribution with hardly visible features is indeed observed for the undoped samples and the peak which may be attributed to photoelectric interactions is observed below 80 phe. Since both doped and undoped samples measured here had the same length (2 cm), the photopeaks observed above 120 phe can reasonably be attributed to Cerium sites. The undoped samples also allow the comparison of photon extraction efficiency as compared to Bridgman grown crystal. Since the scintillation is intrinsic, we are sure that the same number of photons are generated upon γ conversion. Since 160 phe are extracted from the Bridgman grown crystal and only 70 phe are extracted from the fibers, a light loss of 43% was measured. This turn corresponds to an attenuation length of 1.2 cm. This values, although slightly lower, is in agreement with the values estimated with the X-rays.
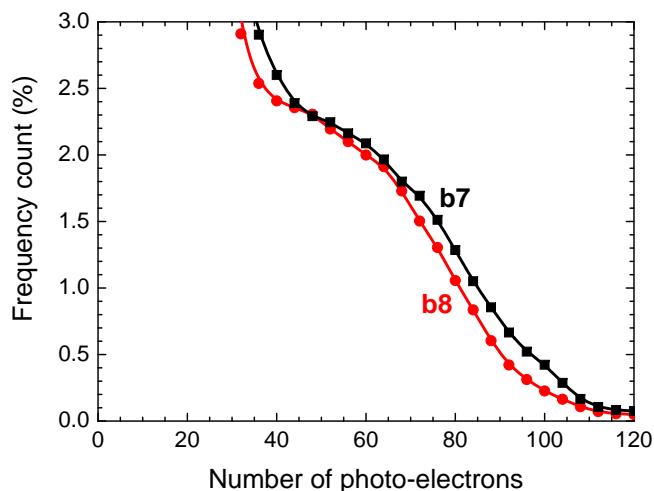
Figure 6.18: Photo-electron distribution of an undoped LuAG fibers grown by μPD. The measurements were acquired in double readout and corrected for the attenuation in the crystals. Interactions were based on 511 keV γ-rays.

The attenuation of the Cerium doped fibers cannot be estimated in the same way since it is difficult to compare them to a Bridgman grown crystal of homogeneous concentration. We decided instead to perform several measurements with

different positions for the radioactive source. The result of these measurements performed on fiber $C3$ are provided in Figure 6.19. The surface of this particular fiber was shown earlier to be partly composed of a defect-free surface, the rest of the surface being altered by ripples and bubbles. We see that this has also an effect on the attenuation curves acquired with γ-rays. The 8 cm length of the fiber led to a rather low number of phe when the source is located at the other extremity of the fiber. And consequently a rather poor resolution of the attenuation curve in that region. We can nevertheless estimate the attenuation length to be in the 4-5 cm range, which is again in agreement with earlier estimations based on X-rays.
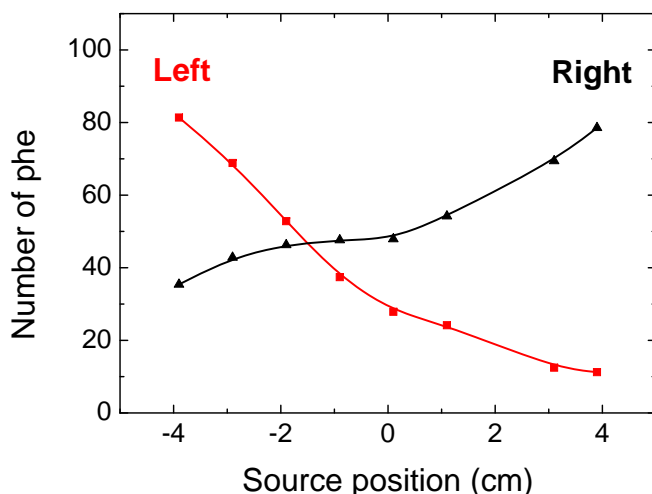
Figure 6.19: Number of photoelectrons collected on the left and the right side of a LuAG:Ce fiber ($C3$) with 511 keV γ-rays.

Confocal measurements estimated at 0.02 at.% and 0.35 at.% the Cerium concentration in the core and the rim respectively. From the study of the light yield as a function of Cerium concentration presented in chapter 3, we would expect respectively a light yield of 10 000 ph/MeV and 30 000 ph/MeV. The two photopeaks should therefore be separated by a factor three. In practice, this factor is much lower. This could be explained by the narrow geometry of the rim. It is possible that the second photopeak is actually a sum of both Cerium

contribution: a Compton scattering occurs in the bulk and the scattered γ-ray is absorbed by photoelectric interaction in the rim. In such a case the factor is lowered by the fraction of energy deposited in the core.

The values in photo-electrons discussed up to now can be converted into photon yield. We then obtain, for the core emission, between 2 000 and 4 000 ph/MeV sent towards each detector, which means up to 8 000 with double readout. This corresponds to up to 50% of the light yield of a Bridgman-grown crystal with an homogeneous Cerium doping of 0.05 at.%.

In addition, the scintillation signal of the Cerium is rather well separated from the intrinsic emission of LuAG which is common to both types of fibers (Cherenkov sensitive ones and scintillation ones). The difference in timing properties can nevertheless also act as a discriminator to exclude this intrinsic scintillation. Cerium doped LuAG has indeed a fast emission in the 60 ns range (as opposed to the μs range of the intrinsic). It is, in that case, especially important to find ways to *speed up* the slow light of the Cerium (as discussed at the end of chapter 3) in order to extract more photons in that time window. Obviously Cherenkov light, with its quasi instantaneous emission of light will also be easily separated.

Regarding the Cherenkov photons, the collection efficiency of these photons could not be studied with such "low "energies as the one used until now (less than a few MeV). From the decay curve acquired on an undoped LuAG crystal grown by Bridgman (presented in Figure 3.12) we can estimate the contribution of the Cherenkov photons to be of 1.7% as compared to the contribution of the intrinsic scintillation light. This intrinsic light generating around 160 phe with our setup, this means that only 2 and 3 photoelectrons can be imputed to the Cherenkov effect. The situation is then worse for fibers grown by μPD, based on the estimation of the attenuation presented earlier, only 1 photoelectron is likely to caused by Cherenkov effect.

This ends this chapter about to the characterization of LuAG fibers grown by the micro-pulling down technology. The next chapter will discuss the behavior of these fibers when assembled to form a calorimeter for the detection of high energetic particles.

Chapter 7

Tests in high-energy conditions

The single crystalline fibers studied in this thesis were designed to be used for calorimetric experiments. In order to be able to discuss their suitability with respect to this application, it is necessary to investigate their behavior at high energies. At CERN, the high energy protons of the SPS (see Figure 1.2), which are partly injected into the LHC rings, are also available in dedicated beam lines for test purposes. Obtaining a time slot on the very busy timetable of these test beam facilities is unfortunately rather difficult and only a few runs could be useful to characterize the LuAG fibers properties in high energy calorimetry conditions. This chapter summarizes the results obtained with all available test beam periods. These tests were performed at the CERN beam lines H2 and H4, in the north area of the SPS, located on the site of Prévessin. These beam lines provide mono-energetic particles produced by the high energy protons accelerated in the SPS. After extraction from the SPS, the protons are directed towards a production target. The desired subset of secondary particles is then filtered with magnets and sent in vacuum pipes to the test areas.

Several experimental zones then acquire data with these beams of particles. Figure 7.1 provides a top view of the facility. On the picture, the experimental zone of the H2 beam line dedicated to the study of the HCAL is visible on the right side of the image. A large yellow movable stage is located in front of the beam pipe and supports a wedge of the CMS detector built out of spare parts of HCAL modules. We obtained two time slots in this experimental area in May and November 2012. The data will be discussed in section 7.2.

Figure 7.1: Picture of H2 (right side) and H4 (middle) beam lines at CERN. In front of H2, the movable stage holding a slice of the CMS detector is visible.

In the central part of the picture (Figure 7.1), the H4 beam line can also be seen. On this beam line, three time slots were available in 2008 and 2009, in the experimental zone dedicated to the investigation of the ECAL. On the contrary to the calorimetry tests performed in 2012, these earlier tests were based on LuAG fibers which were not yet optimized. Nevertheless, given the high importance of a discussion on the behavior of the LuAG fibers at high energies, we decided to further analyze this data in order to extract the maximum of informations from these runs. The results of these data analyses are presented in the next section.

7.1 Calorimetry tests with LuAG meta-crystals

7.1.1 Setup description

In May and November 2009, two batches of 20 fibers with length of 8 cm and diameter of 2 mm were enclosed in a Teflon casing which ensured mechanical support as well as light guidance (see Figure 7.2). Two bundles of fibers, or meta-crystals, were then obtained. The concept of dual readout discussed in earlier chapters is based on meta-crystals composed of both doped and undoped fibers. This configuration was not investigated here because of the complex optics required for separating the readout of both types of fibers. Instead, one meta-crystal was made out of undoped LuAG fibers while the other one was based on Cerium doped LuAG fibers. The red tint observed on some of the undoped fibers was attributed to Europium impurities.
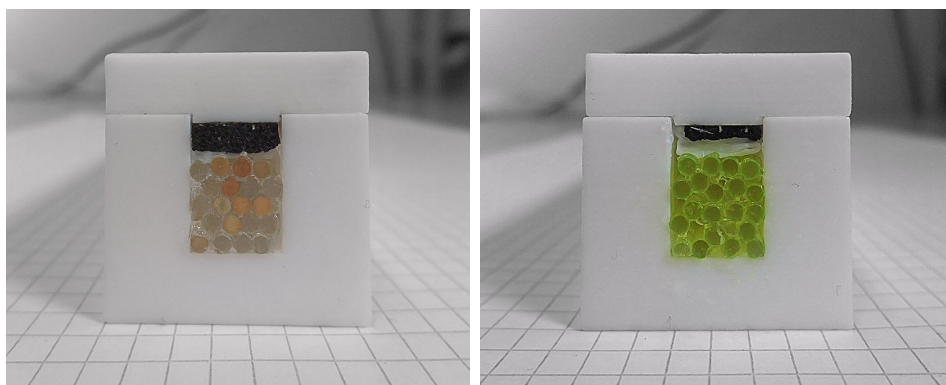
Figure 7.2: Bundle of undoped (left) and Cerium-doped (right) LuAG fibers.

The left and right ands of each of the fiber bundles were coupled with optical grease to two PMTs[1]. This configuration simplifies drastically the readout issues but does not correct for fiber to fiber fluctuations in the light yield. The meta-crystal is indeed read out as would be a bulk crystal. In the case of local

---

[1]XP2020Q from Photonis

inhomogeneities in the fiber batch, the energy resolution may be affected.In order to minimize fluctuations due to the dependence of the light yield on the ambient temperature, the fiber bundles were inserted in a water-cooled copper housing, as depicted in Figure 7.3. The entire setup was finally placed on a rotating table allowing to vary the angle of the impinging beam particles.
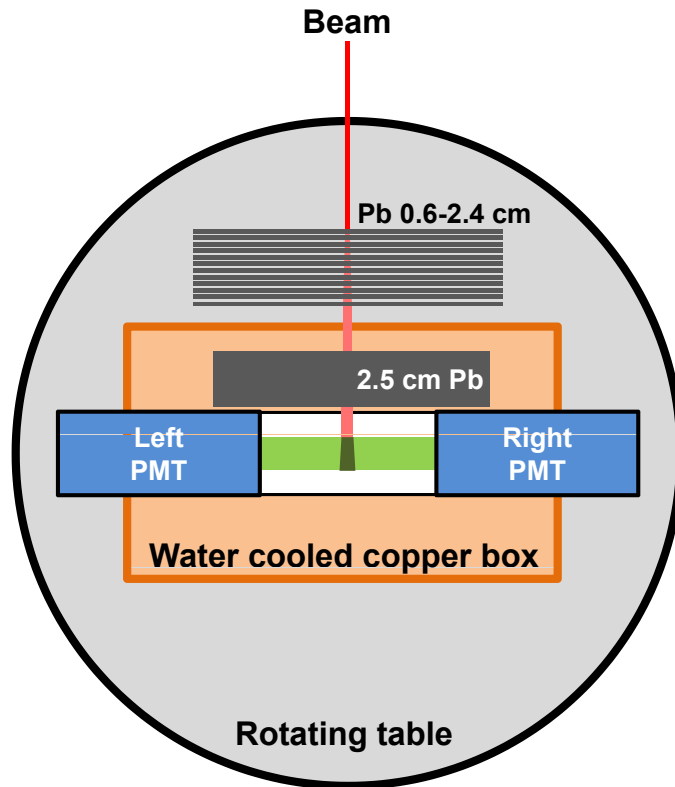
Figure 7.3: Sketch of the setup used for the tests at the H4 beam line.

Because of the high energy of the electrons (120 GeV) and the relatively small amount of active material, the electromagnetic shower deposit a relatively small amount of energy in the LuAG fibers. For this reason, two Lead absorbers were placed before the LuAG bundles. These very dense absorbers, often referred as *preshower*, initiate the electromagnetic shower thus producing much larger observable signals in the bundles of fibers. We used here a combination of two absorbers: one of fixed thickness equal to 2.5 cm and another one composed of

layers of 2 mm thickness. The number of these layers was then adapted depending on the angle of the electrons in order that the beam interacts with a constant thickness of preshower. This enabled us to probe the energy deposition at the same depth of the electromagnetic shower regardless of the angle of incidence of the beam particles. It is worth noting that, because of the geometry of the preshower, only angles between -35° and 35° are relevant. At larger angles, the interaction with the electron beam occurs at the edge of the preshower leading to larger fluctuations in the shower path.

The combination of both preshowers leads to a thickness of 4.9 cm which corresponds to around 9 X_0. According to the equations 2.16, the maximum of the shower is obtained at around 11 X_0 and the 95% containement is reached after 15 X_0. This preshower dimension is thus a good compromise between number of secondary particles and a not too advanced development of the shower.

7.1.2   Correction for light attenuation

As discussed in chapter 6, reading out both end allows to correct for the attenuation of the light along the fiber. To better illustrate this, the left graph of Figure 7.4 provides the charge spectra acquired with only one of the PMTs. As expected, this configuration leads to featureless spectra. On the other hand, we can see that the sum, performed event by event, leads to a clearly distinguishable peak (see green curve on the right graph). We also provided the charge spectra obtained after correction for the attenuation as described in section 6.5. We can observe that this latter curve does not significantly differ from the simple sum of the channels. This is explained by the fact that the beam interaction region was centered in the middle of the fibers. In the case of a longitudinal configuration (beam aligned with the fibers), this improvement would be much more important. Nevertheless, we will apply this correction in this case as well, to reach the best resolution.
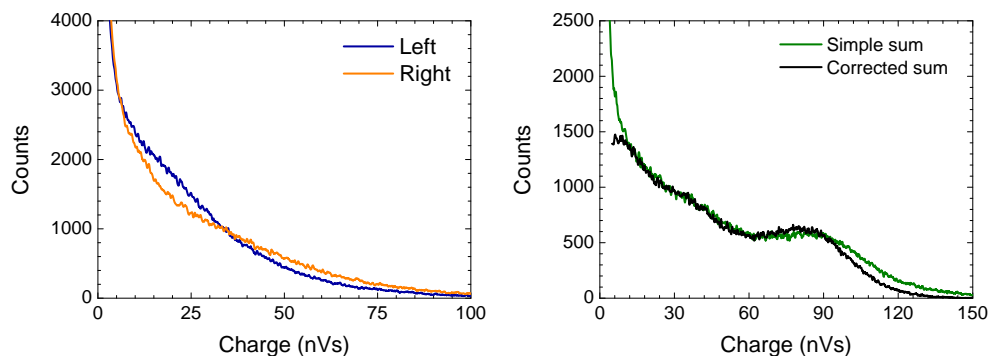
Figure 7.4: Single readout (left) versus double readout (right) with Cerium doped LuAG fibers. The correction of the sum for the attenuation is also compared.

7.1.3   Pulse shapes analysis

Before discussing in more detail the meaning of the peak observed on the previous graph, we will take a closer look at the pulse shapes of the signal acquired with both bundles. The average pulses acquired with each of them is provided in Figure 7.5.
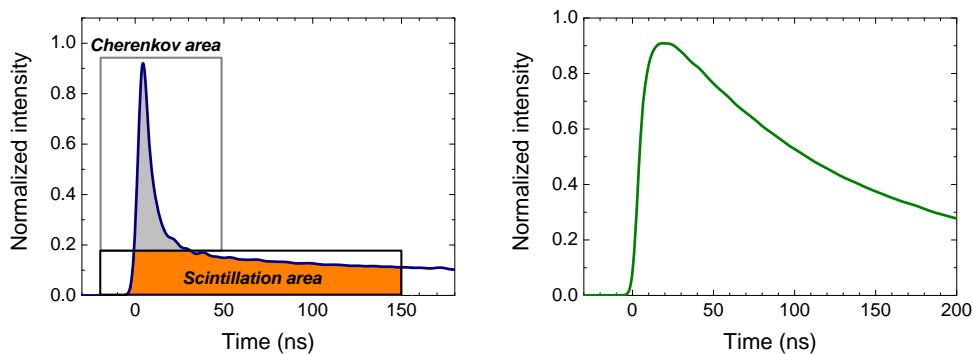
Figure 7.5: Response to 120 GeV electrons hitting perpendicularly the undoped (left) and Cerium-doped (right) LuAG fibers with a 4.9 cm Lead preshower.

We observe a clear difference in pulse shape between Cerium doped and un-doped fibers. The undoped bundle leads to a sharp Cerenkov emission superim-

posed to the intrinsic slow scintillation. On the other hand, with the Cerium-doped bundle, no Cherenkov peak is visible and the scintillation presents, as expected, a much faster decay than the intrinsic contribution. The scintillation is leading to a higher signal and, as a result, no Cherenkov peak is distinguishable with this bundle. Besides, the Cerium bands are wide enough to favor re-absorption of the Cherenkov photons. The Cerium-doped bundle is thus a measurement of all interactions whereas the undoped contribution leads to the Cherenkov signature for short time windows.

7.1.4 Cherenkov - scintillation signals discrimination

In order to be able to study the corrections permitted by the dual readout method, we defined, as in [22], two regions for the integration of the signal of the undoped bundle. The scintillation was estimated with the intrinsic contribution integrated on a 150 ns time window (see Figure 7.5). Cherenkov signals were estimated on a 50 ns time window after subtraction of the intrinsic emission. This discrimination based on time profiles is not as accurate than the use of two types of fibers (due to inter-coupling between Cherenkov and scintillation signals). Nevertheless, this technique will allow us, in the absence of diffractive optics, to discuss the dual readout method applied to the LuAG fibers produced in 2009.

7.1.5 Dual-readout calorimetry

In Figure 7.6, we provide a set of contour plots for two thicknesses of preshower: 2.5 cm and 4.9 cm. The latter configuration probes a more advanced shower development. The increase in the number of secondary particles is thus likely to lead to a higher deposition of energy in the fibers bundle. This is visible when comparing plots e and g to plots f and h respectively. Both the Cherenkov and scintillation signals are indeed higher with the 4.9 cm preshower. On plot h we observe a peak region in the scintillation (labeled with a dashed circle) centered at 60 nVs. On these plots, the events are ranked according to their average position of interaction (as in Figure 6.15). We observe that the distribution of these

interactions is rather narrow, which is again in agreement with the perpendicular incidence of the beam.

Plots *a-d* quantifies the contributions of both Cherenkov and scintillation signals. Plots *a* and *b* provide the Cherenkov (C) over scintillation (S) contributions. Some values of C/S are provided on the graphs to better visualization. In both preshower configurations, two regions with diferent C/S ratio are visible. This is emphasized on plots *c* and *d* where the scintillation is plotted as a function of the $C/(C+S)$ ratio.

It is worh noting that the values of these ratios are dependent on the choice of integration windows. A window of 150 ns was selected here for the integration of the scintillation signals but this corresponds to less than 8% of the total intrinsic emission. Therefore values of Cherenkov and scintillation are usually normalized to a given situation [91]. We decided not to normalize these ratios. They thus have to be considered relatively to each other.

We integrated the contour plots *f* and *h* to obtain the charge spectra (see Figure 7.7) for both thicknesses of preshower. The energy resolution is completely dominated by sampling fluctuations. Our setup is indeed a very simple form of detector: we do not contain the shower and in addition there is only one alternation of passive and active media. With the largest thickness of preshower, the resolution is better since fluctuations in the shower energy density are reduced in vicinity of the shower maximum.

7.1.6 Particle discrimination

As discussed in section 1.4.3, the idea of dual readout is to discriminate events based on the nature of their interaction in order to compensate the difference induced in the detected signal. Reading the Cherenkov and the scintillation signals is one of the possible discriminations. We applied this approach to the data acquired and the charge spectra for events with a Cherenkov fraction lower or higher than 0.34 are displayed in Figure 7.7. Setting this threshold separates two regions in the charge spectra: one Gaussian peak and a broader continuum.

The exact nature of these regions is not clear. Earlier communications demon-

Figure 7.6: Contour plots of Cherenkov and scintillation signals for a bundle of undoped LuAG fibers exposed to a beam of 120 GeV electrons with 2.5 cm (left column) and 4.9 cm (right column) Lead preshower. Impinging angles vary from -35° and 35°.

149

strated the presence of beam contaminants in the H4 electron beam at high energy (above 100 GeV) [20]. The peak at low energies was attributed to muons whereas pions were responsible for a broad energy deposition. The difference in Cherenkov fraction could be explained by these beam impurities but, according to the same paper, they should correspond to about 25% of events. This is not enough to explain the differences observed here. The non-containment of the shower is most probably playing a role. Depending on the angle of the impinging particles, the interaction with the preshower could lead to different shower profiles which in turn could yield different Cherenkov and scintillation signals.
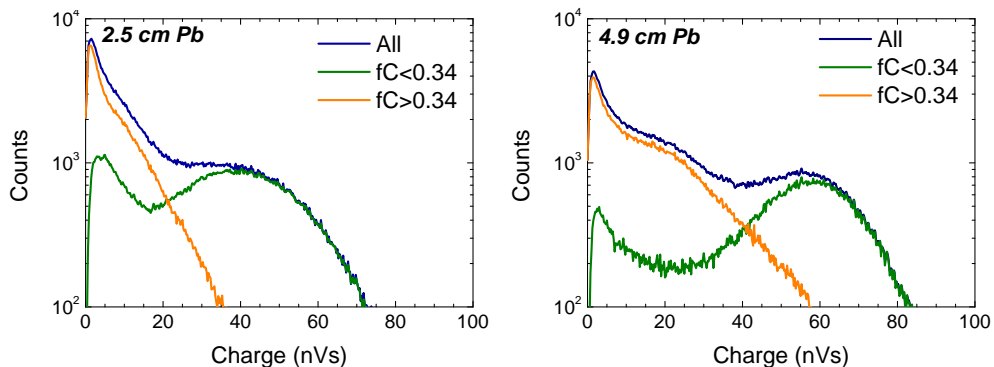
Figure 7.7: Charge spectra of the scintillation light produced by a bundle of undoped LuAG fibers exposed to an electromagnetic shower induced by a 120 GeV electron hitting a 2.5 cm (left) and 4.9 cm (right) Lead preshower.

7.1.7 Scintillation yield improvement with Cerium doping

We mentioned earlier that we did not read simultaneously both the undoped and doped fibers. However we can estimate the improvement permitted by using the Cerium luminescence instead of the intrinsic luminescence of LuAG. In Figure 7.8, we can see that the bundle of Cerium-doped fibers shows an increase in the scintillation light output as compared to the undoped bundle. This gain of a factor 6 can be further increased with a photo-detector presenting a better photon detection efficiency in the green. The use of Cerium-doped fibers is thus relevant since it leads to a better energy resolution (better photon statistics). In addition,

the pulse shape being shorter as compared to the intrinsic scintillation of LuAG, more photons are read out within shorter integration gate. This is important in the case of high interactions rates since a slow component of the scintillation decays can cause a non-negligible pile-up of the signals.
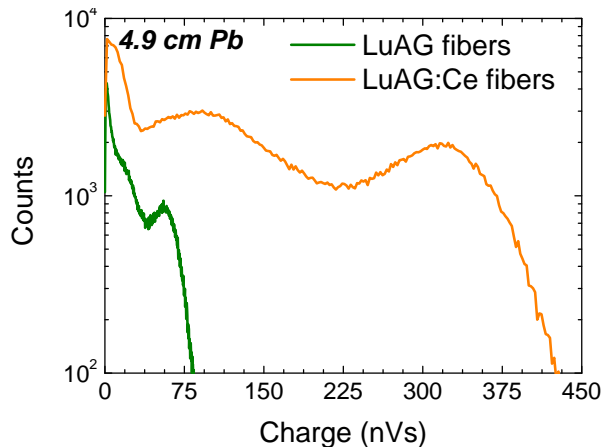
Figure 7.8: Improvement in scintillation yield with Cerium doping.

7.1.8 Comparison with bulk LuAG crystals

We also measured a bulk undoped LuAG crystal of dimensions $2 \times 2 \times 8$ cm^3. The same analysis yielded the contour plots as provided in Figure 7.9. For this crystal, we observed different C/S ratios as compared to the fibers bundles. The crystal probes a larger fraction of the shower since its volume is larger. The relative contribution of Cherenkov and scintillation signals depends on the calorimeter configuration [92] and more precisely on the sampling fraction.

The contour plots discriminating events based on their average interaction point (c and d) distinguishes several regions which most probably correspond to different angle for the impinging electrons. The resolution here is better as compared to the fibers bundles. We could not determine whether this has to be attributed to a better optical quality of the bulk sample or to a higher sampling fraction.
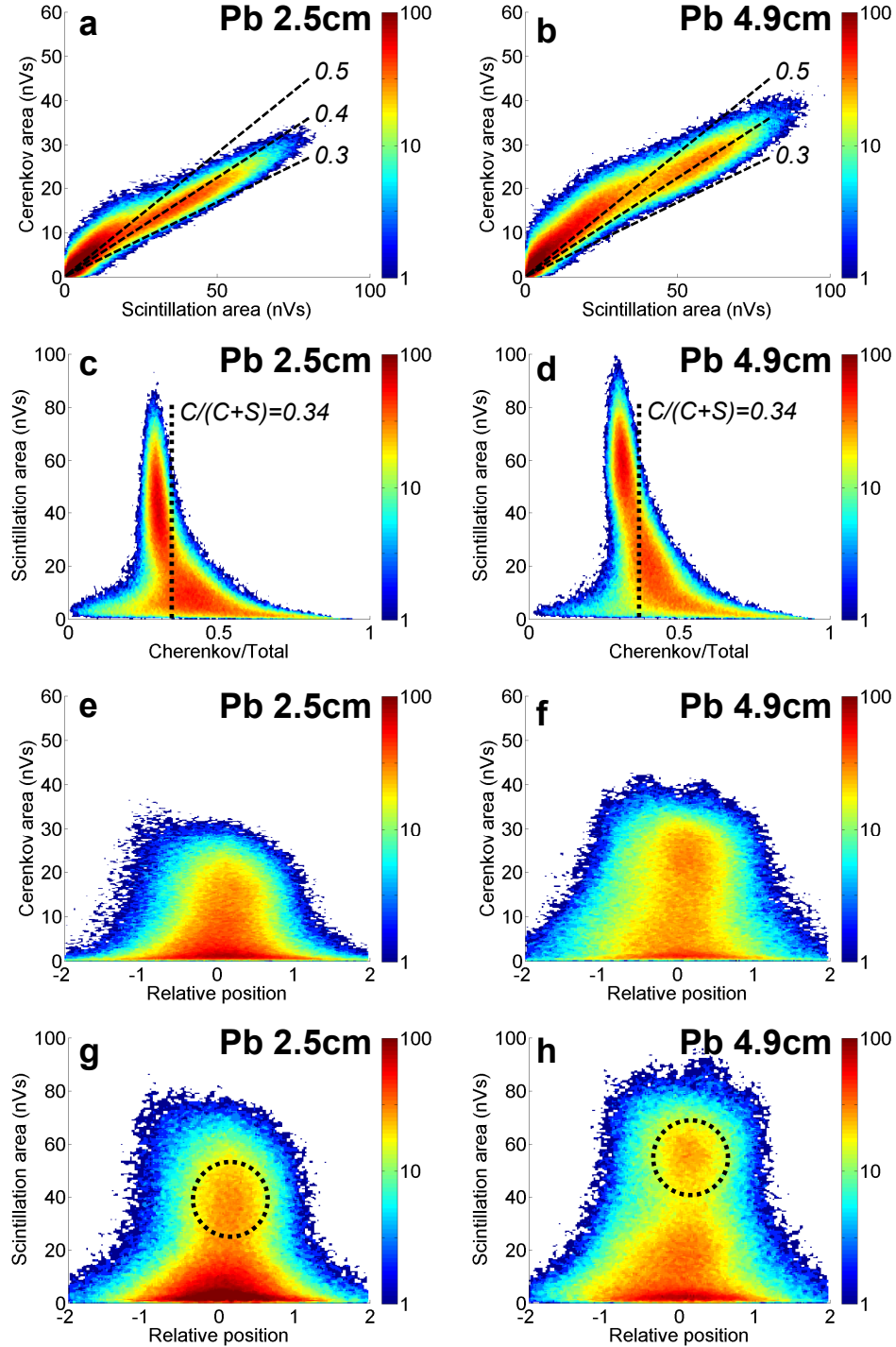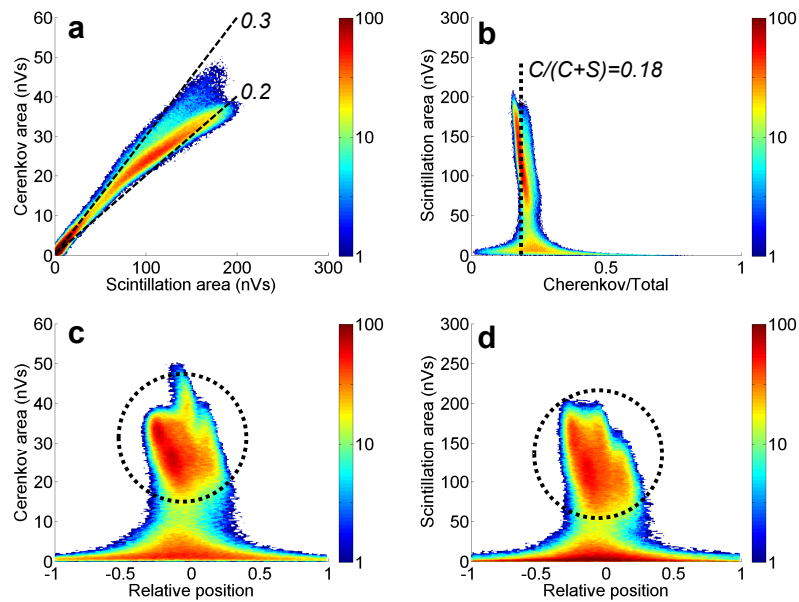
Figure 7.9: Contour plots of Cherenkov and scintillation signals for a bulk crystal of undoped LuAG excited with a beam of 120 GeV electrons with 2.5 cm Lead preshower. As for the fiber bundles, impinging angles vary from -35° and 35°.

7.1.9   Geant4 simulation

To estimate the amount of energy deposited in the different samples, Geant4 [93, 94] simulations were performed with help of Marco Lucchini, PhD student in the same lab at CERN and working on test beam data. The setup (preshower and crystals) was reconstructed with the simulation tool and a quasi-parallel beam of 120 GeV electrons was sent perpendicularly towards the center of the different samples. The distributions of the different energy depositions are provided in Figure 7.10. We plotted on the same graph the experimental data.

The acquired experimental data was not calibrated and the exact number of photoelectrons was thus unknown. If this value would be known, it would be possible to estimate the number of photons generated and thus, assuming a linear response of the crystal, we could obtain the amount of energy deposited in the crystals based on the light yield estimation of chapters 3 and 6. We therefore normalized our data in order to fit it to the values of energies obtained by simulations (red curves on Figure 7.10).

The Geant4 simulations only provide the amount of energy deposited in the sample. The energy resolution computed is not taking into account the photon statistics fluctuations. We observe that the obtained spectra do not differ too much from the experimental ones (except for the fiber bundle with 4.9 cm preshower). This indicates that sampling fluctuations are dominating the resolution of the peaks.

The values of energy depositions obtained with Geant4 also allow us to estimate the number of photoelectrons as observed experimentally. We measured indeed, for undoped fibers of 2 cm, around 60 phe for 511 keV γ-rays (see chapter 6). Assuming a linear behavior of LuAG scintillators, with 8 cm long fibers, the shower of a 120 GeV electron would lead to 30 000 and 53 000 photoelectrons respectively with 2.5 cm and 4.9 cm Lead preshower. These values are most probably over estimated since quenching effects are neglected here.
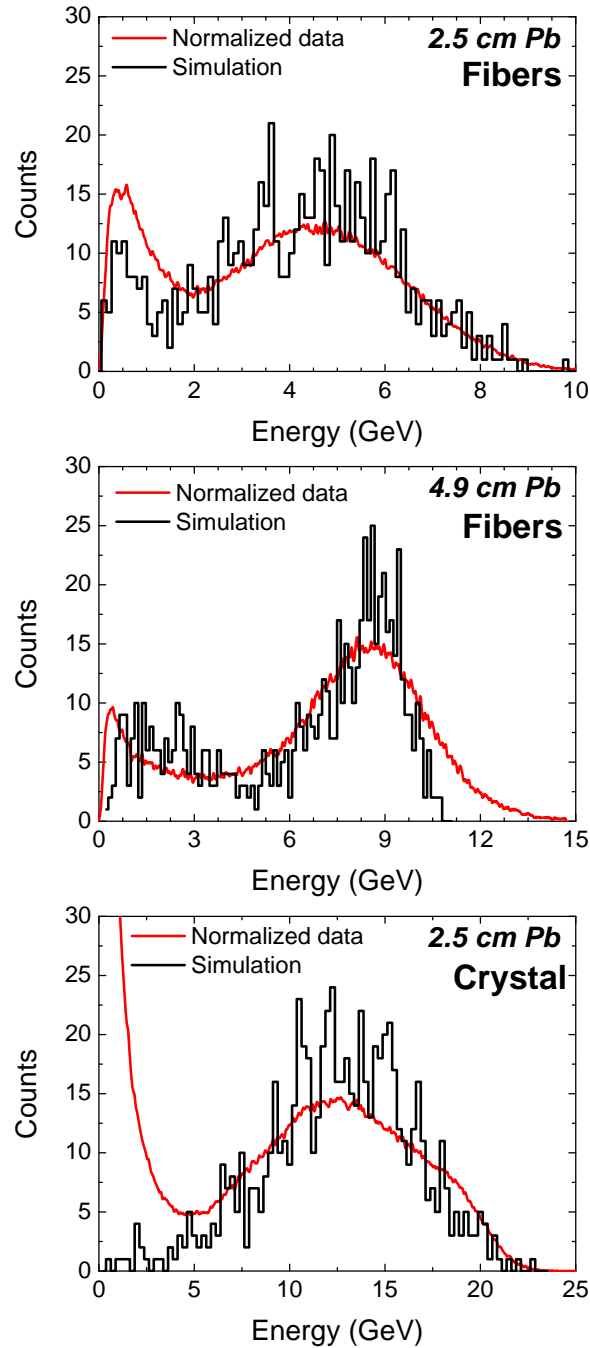
Figure 7.10: Comparison of energy spectra obtained experimentally and with Geant4 simulation for the fibers bundle and the bulk crystal of undoped LuAG.

7.2   Calorimetry tests with the new LuAG fibers

In chapter 6, we demonstrated that the properties of the LuAG fibers have been improved. Therefore, it was important to be able to confirm their better performances with a new test beam campaign. The fact that CERN planned a technical stop of its accelerators from December 2012 to May 2014, urged us to quickly obtain a time slot on one of the beam lines.

On such short notice, we did not manage to obtain some beam time on the H4 beam line as in earlier tests but we obtained some runs in H2. As depicted in Figure 7.11, one of the experimental zones of this beam line has a wedge of CMS detector positioned in front of the beam pipe. Under the black curtain we can recognize the shape of a wedge of hadron barrel (HB). A wedge of the hadron endcap (HE) can also be seen at the back of the stage. In front of the HE, an endcap ECAL (EE) module in its aluminum housing can be seen. The EE module contains four super-crystals, which consists of 4 matrices of 5×5 PbWO$_4$ crystals.

Figure 7.11: Picture of one of the experimental zones of H2. A wedge of the CMS detector (right side) faces the beam line and its triggering system (left side).

We had the opportunity to exchange one of these PbWO$_4$ crystals with a meta-crystal based on LuAG fibers. This work has been performed in close collaboration with Tatiana Medvedeva and Christopher Tully from the University of Princeton (New Jersey, USA) as well as with Arjan Heering and Randal Ruchti from the University of Notre Dame (Indiana, USA). Having the possibility to test the newest batch of LuAG fibers with the possibility to read out neighboring channels turned out to be the best option we could imagine. On Figure 7.12, a closer look at the EE is provided and the positioning of the CFCAL is illustrated.
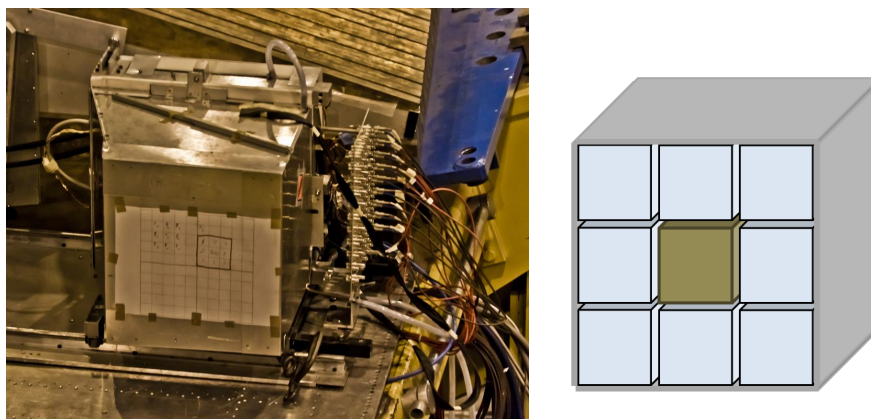
Figure 7.12: Pictures of the EE module containing the 100 PbWO$_4$ crystals facing the beam. On the housing, a red square illustrates the position of a 3 × 3 assembly of crystals. The center position was used to insert a single-crystalline-fiber-based crystal (CFCAL).

Assembling a LuAG CFCAL would in principle require around 150 LuAG fibers of 22 cm each. This number of fibers is obviously too large to be conceivable as a first proof of concept. The decision was thus made to shape a brass absorber of the size of a PbWO$_4$ crystal and to drill holes to host a small number of LuAG fibers. Two test beam campaigns were then planned: one early period in May 2012 to have some preliminary tests of this new configuration and another one based on the latest fibers planned for November 2012.

7.2.1   Test beam of May 2012

The preliminary tests of May 2012 were based on four LuAG fibers. Two of them (F85 and F88) were grown by Fibercryst under the same conditions as the fibers used to obtain the first test beam result in 2009. The other two were grown by K. Lebbou. The fiber C12 turned out to be very weakly doped. The undoped fiber B4 was selected to investigate the Cherenkov light detection. A table summarizing the fiber properties is provided here under:

Fiber ID	Pulling date	Producer	Doping
F85	December 2008	Fibercryst	0.1% at. Ce
F88	December 2008	Fibercryst	0.1% at. Ce
C12	February 2012	K. Lebbou	0.1% at. Ce
B4	January 2012	K. Lebbou	undoped

These four LuAG fibers of diameter 2 mm were wrapped into Teflon tape and inserted into the 3 mm holes of the brass absorber, as depicted in Figure 7.13. The alignment pins and screws on each extremity of the CFCAL allowed the coupling of each individual LuAG fiber with two optical fibers. Each inorganic fiber was thus readout both from the front and the back.

Figure 7.13: Pictures of the brass absorber containing the four LuAG fibers. This CFCAL was inserted among PbWO$_4$ crystals in the EE module facing the beam.

The fibers being here oriented parallel to the beam, the entire length of the fiber is exposed to secondary particles interactions. The double read out (front and back) is necessary to determine the average depth of the energy deposition and thus to enable a correction.

The response of the matrix of $PbWO_4$ crystals of the EE was first calibrated by centering the beam in the middle of each crystal. Subsequently, one of the $PbWO_4$ crystal was replaced by the CFCAL. The optical fibers, coupled to both ends of the LuAG fibers were used to send the scintillation and Cherenkov light to HCAL readout modules based on silicon photomultipliers (SiPMs). The use of these optical fibers allowed positioning the readout boxes behind the HE calorimeter thus protecting the photodetectors from radiation damages.

We acquired data with a beam of mono-energetic electrons centered in the middle of the absorber with a beam size around 2 cm. Runs of 50 000 events were acquired for energies ranging from 15 to 150 GeV. These preliminary test beam runs allowed us to estimate the number of photoelectrons detected as a function of beam energy. It turned out that the Cherenkov fiber $B4$ produced signals too close to the pedestal value to be exploited. We could not determine whether this was due to an intrinsic low number of Cherenkov photons, to a bad propagation of the Cherenkov light in the LuAG fibers or to a low photon detection probability of the HCAL photodetectors. The Cerium doped LuAG fiber $C12$ showed a rather strong light attenuation towards the back of the fiber resulting in very low observable light signals. We attributed this to a large bubble observed in the bulk of the fiber.

On the other hand, fibers $F85$ and $F88$ presented several promising features. The shower of 100 GeV electrons produced observable signals between 30 and 300 photo-electrons depending on the impinging point of the beam. This value can be significantly improved with better light attenuation properties. Given a typical path of light of 11 cm (half length of ECAL crystal), the improvement of the attenuation length from 2 to 8 cm would increase the observed signal by a factor of about 60.

The experimental zone of H2 is equipped with two hodoscopes based on wire chambers which determine the position of the incident particles with a very good accuracy (~ 1 mm). This information is highly useful to study the position dependence of CFCAL response. We selected events with particles position in concentric rings centered on the fiber $F88$. The distribution of the photoelectrons measured in these respective rings are provided in the left plot of Figure 7.14. We observe that the signal in the LuAG fiber is maximal when the impact point of the electrons is located close to the LuAG fiber. It is significantly reduced for particles impacting the calorimeter at distances bigger than 5 mm. The spacing of the fibers is therefore crucial to obtain a good energy resolution. The average interaction point in the fiber (as defined in 6.3) was also computed as a function of the distance of the incident particle from the LuAG fiber (see Figure 7.14, right plot). We note that the center of gravity of the energy deposition is moving towards the back of the fiber, as the radial distance between the incident particle and the fiber increases. When the impact point is located further away from the fiber, the energy detected in a fiber corresponds to the later stages of the electromagnetic shower development.

From this test beam campaign we can conclude that the batch of fibers produced in 2009 yields around 100 photoelectrons for incident electrons of 100 GeV (computed with the corrected sum of front and back readouts). The sampling fraction of the studied prototype is however too low to efficiently probe electromagnetic showers. Nevertheless, the use of both front and back readout associated with a good segmentation of the CFCAL (adequate number of fibers inserted inside) would then bring valuable insight of the shower development.
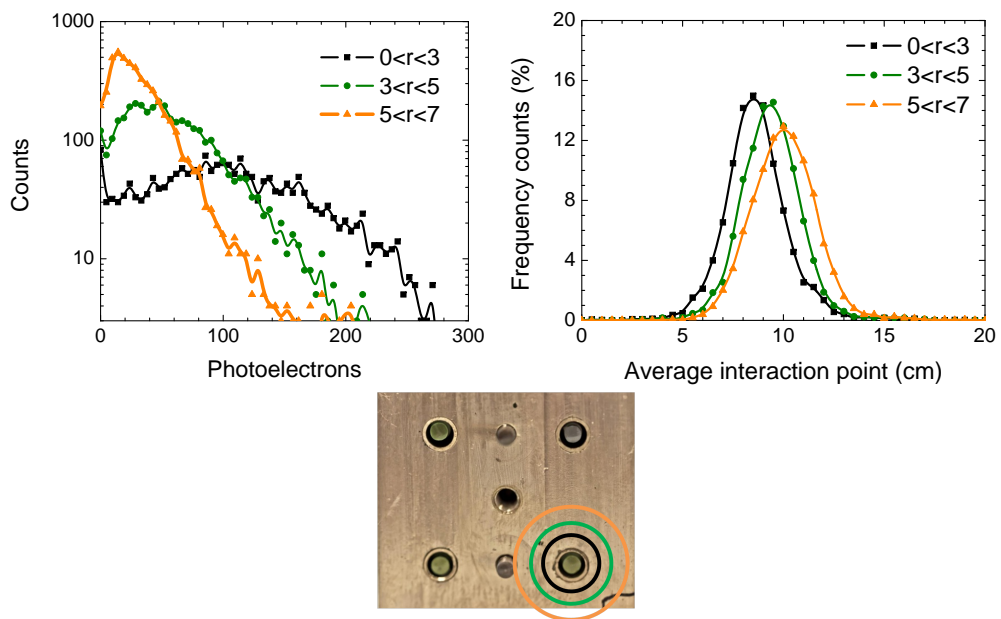
Figure 7.14: Histograms of number of photoelectrons detected (corrected sum of front and back readouts) and average interaction point as a function of the distance of the impinging particle with respect to the center of the LuAG fiber $F88$. Each curve corresponds to concentric rings of diameter 3, 5 and 7 mm.

7.2.2 Test beam of November 2012

This second test beam campaign was based on 9 LuAG fibers (7 doped with Cerium and 2 undoped) in a closer packing (5 mm spacing) as compared to earlier design, as illustrated in Figure 7.15. The fibers doped with Cerium were grown in the same conditions as fiber $C20$ which was demonstrated to present significantly better light attenuation properties (see chapter 6). The properties of the fibers used are summarized in the following table:

Fiber ID	Pulling date	Producer	Pulling rate (mm/min)	Doping
C20	July 2012	K. Lebbou	0.25	0.1 at.% Ce
C22	Oct. 2012	K. Lebbou	0.25	0.1 at.% Ce
C24	Oct. 2012	K. Lebbou	0.25	0.1 at.% Ce
C26	Oct. 2012	K. Lebbou	0.25	0.1 at.% Ce
C27	Oct. 2012	K. Lebbou	0.25	0.1 at.% Ce
C28	Oct. 2012	K. Lebbou	0.25	0.1 at.% Ce
C31	Oct. 2012	K. Lebbou	0.25	0.1 at.% Ce
B9	Jan. 2012	K. Lebbou	0.5	undoped
F1180	Nov. 2011	Fibercryst	0.5	undoped

Among the seven LuAG fibers doped with Cerium, five of them (in bold in the table) presented outstanding transmission properties. These fibers were located on the cross (vertical and horizontal center lines) of the nine absorber holes in order to obtain the best measurement in the core of the shower (see Figure 7.15). Two undoped fibers were located at opposite corners, the remaining positions were occupied by fibers $C27$ and $C28$. These fibers were grown while strong vibrations were affecting the growth facility. These vibrations led unfortunately to macroscopic defects observed at some positions of the fiber axis. These defects are responsible for the significantly higher light losses observed experimentally. Among the undoped fibers, we observed that sample $B9$ exhibited some remaining Cerium dopant (weak green color of the fiber). Therefore this fiber is not strictly transmitting all the Cherenkov signal (the light could be partly absorbed by these parasitic Cerium sites).
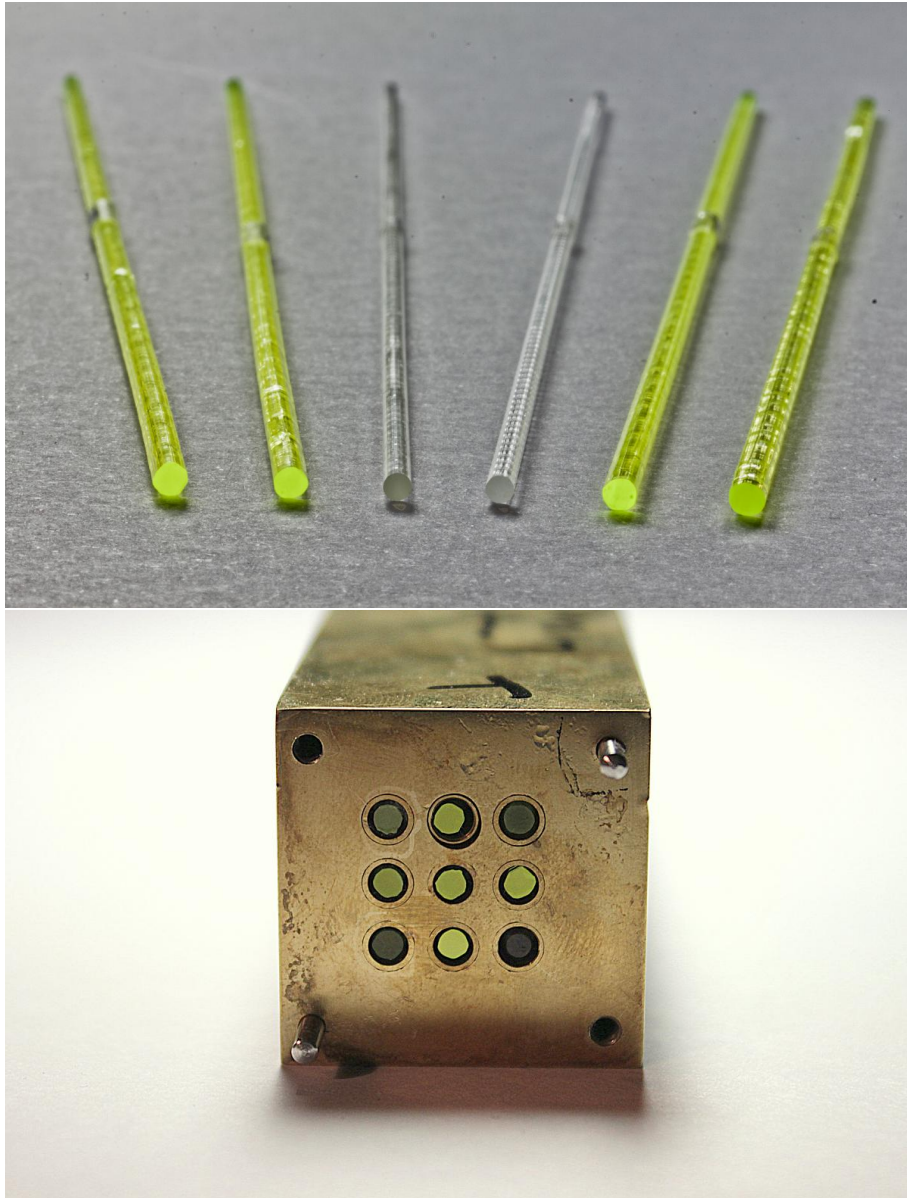
Figure 7.15: Pictures of the last batch of undoped and Cerium doped LuAG fibers (top) and of the second brass absorber containing nine LuAG fibers (bottom). The fibers in the top left and bottom right corners are undoped. The other two corner positions are occupied by LuAG:Ce fibers with poorer light transmission.

In this test beam campaign, the fibers were again read out from the front and back with help of optical fibers. Since only 16 channels were available in the HCAL readout module, the decision was taken to sum electronically the front and back readouts of the two bottom corner positions (corresponding to fibers $C27$ and $F1180$).

At the time this document is being written, the analysis is still at an early stage, therefore only a succinct overview will be presented. Analysis of the collected data has revealed that the back read out of the central fiber $C24$ (central position) has failed and that the fiber $C27$ and $C28$ show too low signals to be efficiently exploited. As a result, from the 7 Cerium fibers only 4 of them can be used for a full analysis of the shower. On the other hand, these fibers led to a drastic increase in the amount of photoelectrons collected, as compared to earlier fiber batches. We estimated a gain of a factor 10, which is consistent with the improvement of the optical quality of the fibers.

Concerning the undoped fibers, as expected, the directionality of the Cherenkov light favors the back readout. Since the front and back readouts of one of the undoped fibers were summed electronically, this resulted in a signal loss due to noise addition since the front readout only detected a very low number of Cherenkov photons. The remaining Cherenkov fiber was unfortunately the fiber $B9$ which exhibits noticeable concentration of a scintillating dopant.

The beam runs acquired here had in principle a significant advantage over earlier runs to allow a Cherenkov-Scintillation separation in a situation the closer to the concept presented in [24]. Two different types of fiber were indeed dedicated to the Cherenkov and scintillation signals and read out separately, thus resembling the situation expected in meta-crystals with diffractive readout. It is therefore rather unfortunate that only a very weak Cherenkov signature of the showers could be measured. Nevertheless, is not excluded that an accurate definition of the Cherenkov signals, a careful inter-calibration and, more generally, a more in-depth analysis may improve the quality of this Cherenkov-scintillation separation.

Despite the limitations mentioned earlier, we extracted some first results from the acquired data. The focus was set on the central fiber and only the front readout was considered. Figure 7.16 provides the values of the average energy deposited in the central fiber as a function of the incident particle impact point (determined with the wire chambers). The projection along the X and Y axis are also provided.

From the difference between the X and Y profiles ($\sigma = 6.0$ mm and $\sigma = 3.5$ mm, respectively) we suspect that the beam divergence was somewhat higher in the X direction. It would be possible to verify this hypothesis by comparing the interaction points used here (obtained from the last wire chambers) with the one of the other wire chambers, located upstream.

Nevertheless, as in section 7.2.1, we observe a significant dependence of the measured signal on the impact point of the particle. Distribution of the observed signals for the complete data set is shown as a black curve in Figure 7.17. Its shape is primarily a reflection of the distribution of distances between the incident particle and the fiber. Using the profiles shown in 7.16 we have derived a correction factor as a function of a distance between the beam particle and a fiber. Correction of the observed signal with this position-dependent factor yields the energy distribution shown as a red curve in Figure 7.17.

This correction was applied to runs acquired with different electron energies yielding the distributions of observed energies shown in the top graph of Figure 7.18.

The position of the peak is shifted towards higher ADC channels as the energy of the incident electrons is increased. Moreover, it is worth noting that, even with only one LuAG fiber, a good linearity is observed (see bottom graph of Figure 7.18). The energy resolution appears however constant, regardless of the incident electron energy. Since these energy distributions were obtained with only one LuAG fiber, this should be improved by making use of the entire set of fibers.

We analyzed the average energy deposited in the center column of the CFCAL (3 LuAG fiber selected, out of the 9). Figure 7.19 shows the average observed energy as function of the Y-coordinate of the incident electron impact point for
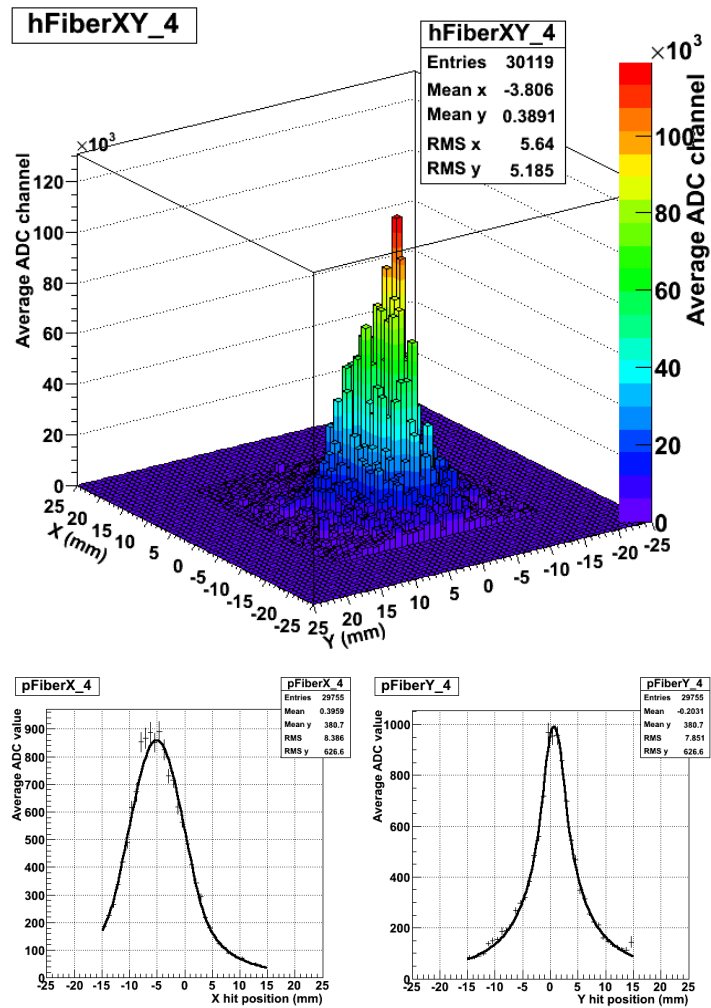
164

Figure 7.16: Average energy (in ADC channels) deposited in the central Cerium-doped LuAG fiber as a function of the position of the impact point of 100 GeV electrons. The X and Y coordinates were obtained from the wire chambers. Only the front readout, facing the beam, was used.
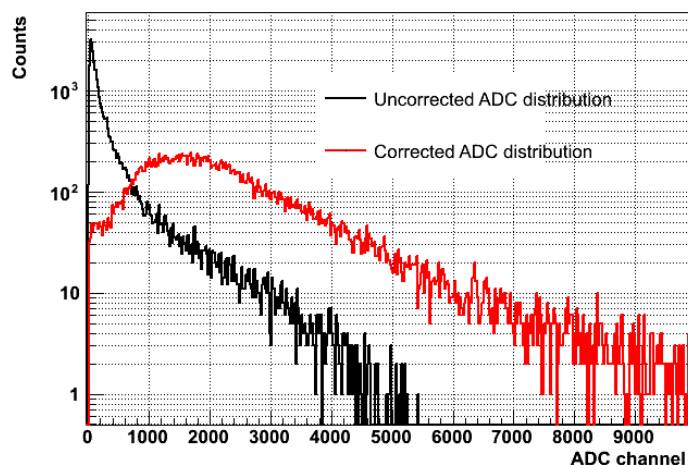
Figure 7.17: Energy (in ADC channels) distribution of the central Cerium-doped LuAG fiber with a 3×3 cm² beam of 100 GeV electrons before (black curve) and after (red curve) correction for the shower containment. Only the front readout was considered.

the three scintillating fibers (blue, black and green curves on the graph). We observe that the widths of the energy profiles do not significantly differ from fiber to fiber. Moreover, their respective maximum, which correspond to impact points of the incident electrons aligned with the LuAG fibers is of very similar magnitude, within ~15%. implying a fairly good uniformity in between scintillating LuAG fibers. Nevertheless, we inter-calibrated the fibers by correcting for the slight difference observed for these peaks. Subsequently, we summed the signals of the three fibers, event by event, as illustrated with 80 GeV incident electrons on the red curve of Figure 7.19.

We note that the middle peak is the highest of the three peaks observed for the sum plot (red curve). This is explained by the fact that showers corresponding to particles hitting the middle fiber are also probed by the two neighboring fibers. The energy leakage is thereby reduced. For Y-positions between -2 mm and 8 mm, the difference between peaks and valleys reflects the uniformity of response of the CFCAL: the peaks are obtained when hitting the LuAG fibers, lower values are obtained when hitting the absorber. These fluctuations can be decreased by changing the spacing distance between the fibers. The best results
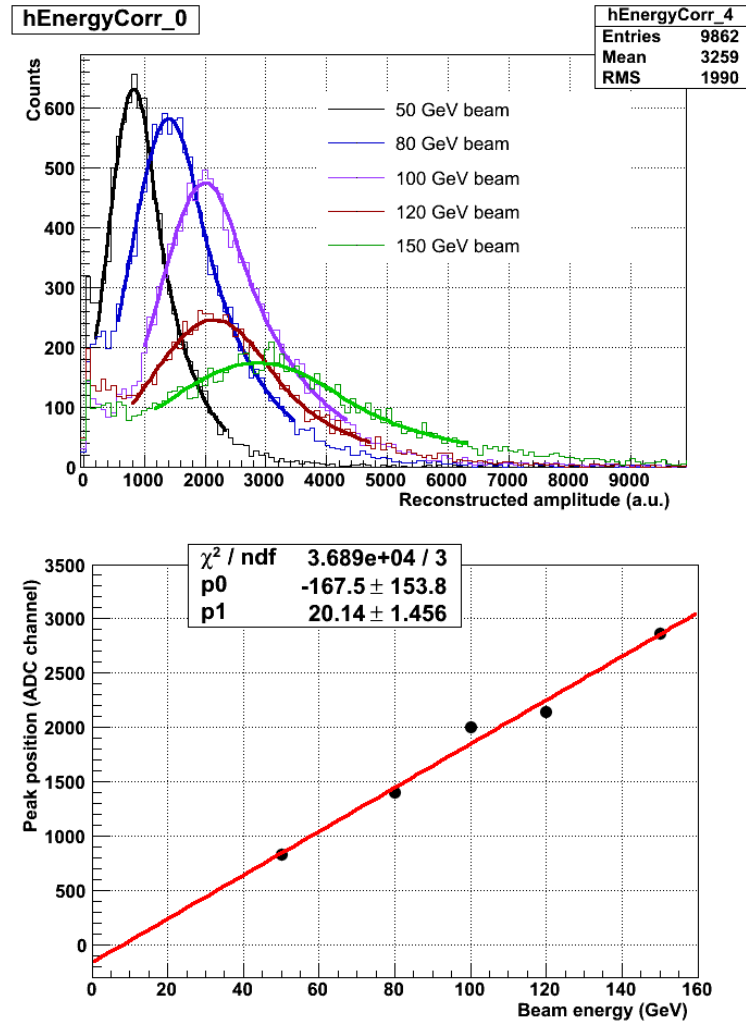
Figure 7.18: Corrected energy distribution (top) and dependence of the peak position of the electron beam energy (bottom) for the central Cerium-doped LuAG fiber with a 3×3 cm² beam of 50, 80, 100, 120 and 150 GeV electrons. Only the front readout was considered.
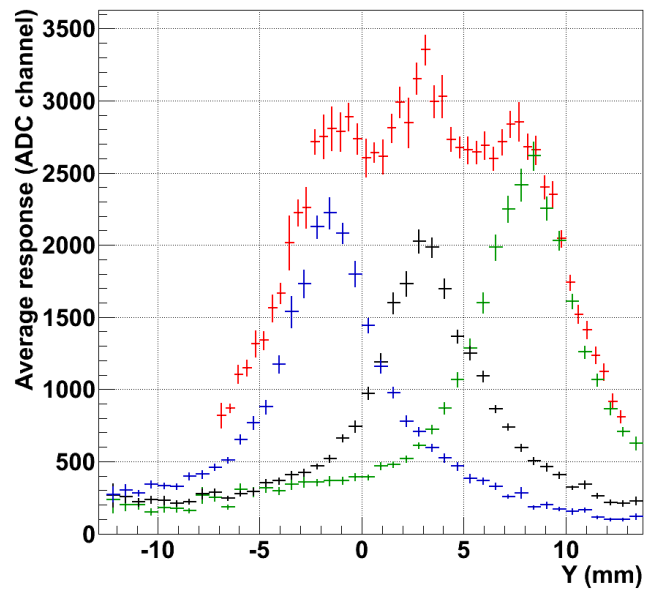
Figure 7.19: Average energy (in ADC channels) deposited in the Cerium-doped LuAG fibers of the center column as a function of the position of the impact point of 80 GeV electrons (blue, black and green curves). The red curve is the sum obtained after inter-calibration of the fiber responses.

would then be obtained with no dead-space, which means a meta-crystal as the one initially designed.

As mentioned earlier, the analysis of the entire data was not completed at the time this document is written. Future work could focus on the extraction of the signals of the 9 fibers, both in front and back readout. This information would allow to investigate the shower development both in radial and longitudinal directions. The undoped LuAG fibers could also be used for estimation of the Cherenkov signature of the showers. The run acquired with 150 GeV pions could be compared with the data acquired with electrons of the same energy in an attempt to discriminate events based on a dual-readout approach.

Chapter 8

Summary and outlook

Most hadronic calorimeters suffer from a poor energy resolution due to fluctuations in the electromagnetic fraction of hadronic showers. Dual-readout calorimeters, which measure simultaneously both Cherenkov and scintillation light, are able to cancel out these fluctuations by compensating the response of the calorimeter event by event. In this thesis, a new concept of dual-readout calorimetry based on heavy inorganic single-crystalline fibers was investigated. A garnet of Lutetium and Aluminium (LuAG) was selected as host matrix. Used as such, its high index of refraction, its low Cherenkov threshold and its good UV transmission make this material behave like an efficient Cherenkov radiator. Rare-earth doping can, in addition, activate scintillation processes. Fiber-shaped crystals of both types can then be assembled to form a homogeneous calorimeter (same host material) with a segmentation allowing dual-readout calorimetry (undoped fibers collect the Cherenkov fibers while the doped fibers generate scintillation).

To activate the scintillation of LuAG, Cerium ions were selected. The effects of the concentration of these doping centers on the scintillation light output and the timing properties were investigated. The best performances were obtained for Cerium concentrations higher than 0.2 at.%. Under these conditions, light outputs of around 30 000 photons per MeV were measured on a time window of 4 μs. Higher concentrations of Cerium lead to shorter scintillation decays due to quenching mechanisms. Hafnium and Scandium ions were also added to the matrix as co-dopant. Hafnium co-doping did not bring any significant modification

in the pulse shape. On the other hand, Scandium co-doping out-performs non co-doped LuAG:Ce for lower Cerium concentrations.

The challenge was then to produce LuAG fibers with properties as close as possible to the properties of bulk LuAG to maximize the performances of the calorimeter. The fiber geometry itself was demonstrated to cause non-negligible effects on the collection of the generated light. Even when high optical quality of the crystals was achieved, a drop in the light collection was observed when the width of the crystals was smaller than 2.5 mm. Moreover surface defects were demonstrated to further worsen the light collection. Obtaining this geometry with traditional growth methods would require cutting and polishing the grown ingots. Although a well-controlled surface state is achievable, these techniques are not applicable for large scale productions. Given the amount of fibers involved in the construction of a calorimeter for high energy physics, the micro-pulling down technique was selected instead. We demonstrated however that this choice has consequences on the properties of the LuAG crystals grown. The comparison of the thermally-stimulated luminescence (TSL) of samples grown by the Czochralski, Bridgman and μPD techniques revealed different nature and concentrations of the charge carriers traps. LuAG crystals grown by the Czochralski technique led to the lowest concentration of meta-stable traps. These traps are responsible for the slow light component observed on the scintillation pulses. Although the μPD technique is based on a process which seems close to the Czochralski process, a larger concentration of these defects was observed. This observation was attributed to the smaller size of the melting zone.

For what concerns the optical quality of the fibers grown by μPD, significant improvement could be achieved by optimizing the growth parameters. For the scintillating fibers, a Cerium concentration of 0.1 at.% was identified as the best compromise. This value implied a lower light output, as compared to the 30 000 photons per MeV, but large surfaces defects were responsible for important light losses at higher doping concentrations. A low pulling rate (0.25 mm/min) was selected to grow the LuAG fibers. This value led to a strong segregation of the Cerium ions but the light gain obtained with a better surface state motivated

this choice. Moreover, the effect of the segregation was found to not significantly affect the energy spectrum since most of the energy deposit occurs in the central part of the fiber where the Cerium distribution is homogeneous. The latest batch of fibers presented a light output of 8000 photons per MeV in the core and an adequate behavior as light guide with an attenuation length above 15 cm.

Furthermore, we tested the behavior of the single-crystalline fibers of LuAG when assembled in a calorimeter to detect high energy electrons and pions. Despite the light losses involved by the readout system, around 100 photoelectrons were measured on each side of these scintillating fibers per GeV of energy deposit. Collecting the signals out of all the fibers forming the calorimeter is thus yielding signals where photo-statistics are not dominating. The dual-readout approach was validated on batches of fibers with lower quality and is thus expected to apply on the fibers grown under optimized conditions.

This thesis thus confirmed the potential of LuAG fibers grown by micro-pulling down to be used for dual-readout calorimetry and allowed for optimistic perspectives. As a guideline for future work, we will suggest here a set of research directions.

Fiber environment Although the light propagation in the fibers progressed significantly, the use of different coatings and wrappings could be investigated for further improvement. Recent progresses made in designing quartz capillaries [95] could also be applied here. By inserting the LuAG fibers in these tubes of quartz with an adequate coupling media for index matching, the surface state of the fibers then would only play a minor role.

Radiation hardness It was shown very recently that LuAG presents a moderate radiation hardness when residual Yb is present in the raw Lu_2O_3 oxide [96]. Since it is likely that the radiation hardness also dependents on the growth method, radiations tests of the latest batch of fibers produced by micro-pulling down would be highly instructive. Depending on the outcome of these tests, the use of co-doping centers and of thermal annealing to improve the radiation

hardness might be required to be investigated.

Choice of material   The possibility to investigate other materials for the host matrix has not to be excluded. The recently investigated multicomponent garnets like $Gd_3Ga_3Al_2O_{12}$:Ce [97] could be considered for instance. While the feasibility of the growth of these alternative materials with the micro-pulling down technique is likely to be decisive, the cost of Lutetium as a raw material should also be included in the discussions. Another approach would be the use of an absorber, as for the last test beam runs. This would reduce the number of fibers required and ease the mechanical alignment of the readout. Besides, a brass absorber may allow the use of a host matrix of lower density. Garnets of Yttrium and Aluminium (YAG) might then be considered since the growth of these garnets with micro-pulling down was already efficiently optimized for laser applications [89, 98, 99]. On the contrary to the meta-material approach, such a design for a calorimeter will however lead to sampling fluctuations.

References

[1] J. WENNINGER. Operational challenges of the LHC, `http://irfu.cea.fr/Phocea/file.php?file=Seminaires/1595/Dapnia-Nov07-partA.ppt`, 2007.

[2] THE CMS COLLABORATION. The CMS experiment at the CERN LHC. *Journal of Instrumentation*, **08004(3)**, 2008.

[3] CMS COLLECTION. Hadronic calorimeter (HCAL) calibration with cosmics and wire source has started, `http://cdsweb.cern.ch/record/897985`, 2005.

[4] CMS COLLECTION. Assembly of the 7th wedge, `http://cdsweb.cern.ch/record/41645`, 2000.

[5] CMS COLLECTION. Early construction of muon chambers `http://cdsweb.cern.ch/record/1274451`, 2007.

[6] CMS COLLECTION. Completion of cathode strip chamber (CSC) installation on the plus endcap of CMS, `http://cdsweb.cern.ch/record/930099`, 2006.

[7] R. WIGMANS. Sampling calorimetry. *Nuclear Instruments and Methods in Physics Research Section A: Accelerators, Spectrometers, Detectors and Associated Equipment*, **494(1-3)**:277–287, Nov. 2002.

[8] N. AKCHURIN, K. CARRELL, J. HAUPTMAN, H. KIM, H. PAAR, a. PENZO, R. THOMAS and R. WIGMANS. Hadron and jet detection with a dual-readout

calorimeter. *Nuclear Instruments and Methods in Physics Research Section A: Accelerators, Spectrometers, Detectors and Associated Equipment*, **537(3)**:537–561, Feb. 2005.

[9] R. WIGMANS. Calorimetry - energy measurement in particle physics. Oxford University Press, 2000.

[10] D. ACOSTA, S. BUONTEMPO, L. CALBA, M. CARIA, R. DESALVO, A. EREDITATO, R. FERRARI *et al.* Electron, pion and multiparticle detection with a lead/scintillating-fiber calorimeter. *Nuclear Instruments and Methods in Physics Research Section A: Accelerators, Spectrometers, Detectors and Associated Equipment*, **308(3)**:481–508, 1991.

[11] E. BERNARDI, G. DREWS, M. GARCIA, R. KLANNER, U. KTZ, G. LEVMAN, M. LOMPERSKI, D. LKE, E. ROS, F. SELONKE, H. TIECKE, M. TSIROU and W. VOGEL. Perfomance of a compensating lead-scintillator hadronic calorimeter. *Nuclear Instruments and Methods in Physics Research Section A: Accelerators, Spectrometers, Detectors and Associated Equipment*, **262(23)**:229–242, 1987.

[12] E. GARUTTI. Overview on calorimetry. *Nuclear Instruments and Methods in Physics Research Section A: Accelerators, Spectrometers, Detectors and Associated Equipment*, **628(1)**:31–39, Feb. 2011.

[13] M. THOMSON. Particle flow calorimetry and the PandoraPFA algorithm. *Nuclear Instruments and Methods in Physics Research Section A: Accelerators, Spectrometers, Detectors and Associated Equipment*, **611(1)**:25–40, 2009.

[14] J.-C. BRIENT and H. VIDEAU. The Calorimetry at the future e$^+$-e$^-$ linear collider. *eConf*, **C010630**:E3047, 2001.

[15] The CALICE collaboration webpage, `https://twiki.cern.ch/twiki/bin/view/CALICE`.

[16] THE CALICE COLLABORATION. Design and electronics commissioning of the physics prototype of a Si-W electromagnetic calorimeter for the International Linear Collider. *Journal of Instrumentation*, **3(08)**:8001, 2008.

[17] THE CALICE COLLABORATION. Construction and commissioning of the CALICE analog hadron calorimeter prototype. *Journal of Instrumentation*, **5(05)**:5004, 2010.

[18] N. AKCHURIN, S. AYANB, G. L. BENCZEC, K. CHIKIND, H. COHNE, S. DOULASF, I. DUMANOGLUA *et al.* Beam test results from a fine-sampling quartz fiber calorimeter for electron , photon and hadron detection. *Nuclear Instruments and Methods in Physics Research Section A: Accelerators,Spectrometers, Detectors and Associated Equipment*, **9002(97)**, 1997.

[19] N. AKCHURIN, K. CARRELL, J. HAUPTMAN, H. KIM, H. PAAR, a. PENZO, R. THOMAS and R. WIGMANS. Muon detection with a dual-readout calorimeter. *Nuclear Instruments and Methods in Physics Research Section A: Accelerators, Spectrometers, Detectors and Associated Equipment*, **533(3)**:305–321, Nov. 2004.

[20] N. AKCHURIN, K. CARRELL, J. HAUPTMAN, H. KIM, H. PAAR, a. PENZO, R. THOMAS and R. WIGMANS. Electron detection with a dual-readout calorimeter. *Nuclear Instruments and Methods in Physics Research Section A: Accelerators, Spectrometers, Detectors and Associated Equipment*, **536(1-2)**:29–51, Jan. 2005.

[21] R. WIGMANS. The DREAM project: Towards the ultimate in calorimetry. *Nuclear Instruments and Methods in Physics Research Section A: Accelerators, Spectrometers, Detectors and Associated Equipment*, **617(1-3)**:129–133, May 2010.

[22] N. AKCHURIN, F. BEDESCHI, a. CARDINI, M. CASCELLA, G. CIAPETTI, A. D'ORAZIO, L. COLLICA *et al.* Detection of electron showers in dual-readout crystal calorimeters. *Nuclear Instruments and Methods in Physics Research Section A: Accelerators, Spectrometers, Detectors and Associated Equipment*, **686**:125–135, Sep. 2012.

[23] E. AUFFRAY, D. ABLER, P. LECOQ and G. MAVROMANOLAKIS. Dual read-out with PWO crystals and LuAG crystal scintillating fibers. *Nuclear Science, IEEE Transactions on*, **57(3)**:1454–1459, June 2010.

[24] P. LECOQ. New crystal technologies for novel calorimeter concepts. *Journal of Physics: Conference Series*, **160(1)**:12016, 2009.

[25] E. AUFFRAY, D. ABLER, P. LECOQ, C. DUJARDIN, J. FOURMIGUE and D. PERRODIN. Dual readout calorimeter with heavy scintillating crystal fibers. 3262–3265, Oct. 2008.

[26] P. LECOQ. Metamaterials for novel X- or γ-ray detector designs. *2008 IEEE Nuclear Science Symposium Conference Record*, 1405–1409, Oct. 2008.

[27] E. AUFFRAY, D. ABLER, S. BRUNNER, B. FRISCH, A. KNAPITSCH, P. LECOQ, G. MAVROMANOLAKIS, O. POPPE and A. PETROSYAN. LuAG material for dual readout calorimetry at future high energy physics accelerators. *2009 IEEE Nuclear Science Symposium Conference Record (NSS/MIC)*, 2245–2249, 2009.

[28] A. HERVE, P. LECOQ, J. M. LE GOFF, F. ALLEGRETTI, S. PIZZINI, B. BORGIA, F. FERRONI *et al.* R&D proposal for the study of new fast and radiation hard scintillators for calorimetry at LHC. Tech. Rep. CERN-DRDC-91-15. DRDC-P-27, CERN, Geneva, 1991.

[29] C. GRUPEN and B. SCHARTZ. Particle detectors. Cambridge university press, 2008.

[30] D. GROOM and S. KLEIN. Passage of particles through matter. *The European Physical Journal C - Particles and Fields*, **15**:163–173, 2000.

[31] M.J. BERGER, J.S. COURSEY, M.A. ZUCKER AND J. CHANG. Stopping-power and range tables for electrons, protons, and Helium ions.

[32] K. HIKASA *et al.* Review of Particle Physics. *Phys. Rev. D*, **46**, 1992.

[33] M.J. BERGER, J.H. HUBBELL, S.M. SELTZER, J. CHANG, J.S. COURSEY, R. SUKUMAR, D.S. ZUCKER, AND K. OLSEN. Photon cross sections database.

[34] C. LEROY and P.-G. RANCOITA. Ultrahigh-energy and compensating calorimetry physics of cascading shower generation and propagation in matter : principles of high-energy , ultrahigh-energy and compensating calorimetry. *Reports on Progress in Physics*, **63(4)**:505, 2000.

[35] G. MAVROMANOLAKIS. Quartz fiber calorimetry and calorimeters. Tech. Rep. physics/0412123. HEP-Cavendish-2004-34. UA-NPPS-06-2003-06, Athens Univeristy, Athens, Dec. 2004.

[36] P. ANFRÉ. Localisation des interactions de rayonnements ionisants sur des fibres monocristallines scintillatrices. Ph.D. thesis, Université Claude Bernard - Lyon I, 2006.

[37] Y. ZORENKO, V. GORBENKO, A. VOLOSHINOVSKII, G. STRYGANYUK, V. MIKHAILIN, V. KOLOBANOV, D. SPASSKY, M. NIKL and K. BLAZEK. Exciton-related luminescence in LuAG:Ce single crystals and single crystalline films. *Physica Status Solidi (a)*, **202(6)**:1113–1119, 2005.

[38] M. NIKL, A. YOSHIKAWA and T. FUKUDA. Charge transfer luminescence in Yb^{3+}-containing compounds. *Optical Materials*, **26(4)**:545–549, 2004.

[39] M. NIKL, a. VEDDA, M. FASOLI, I. FONTANA, V. LAGUTA, E. MIHOKOVA, J. PEJCHAL, J. ROSA and K. NEJEZCHLEB. Shallow traps and radiative recombination processes in $Lu_3Al_5O_{12}$:Ce single crystal scintillator. *Physical Review B*, **76(19)**:1–8, Nov. 2007.

[40] P. LECOQ, A. ANNENKOV, A. GEKTIN, M. KORZHIK and C. PEDRINI. Inorganic Scintillators for Detector Systems. Springer, 2006.

[41] J. M. OGIEGLO, A. ZYCH, K. V. IVANOVSKIKH, T. JSTEL, C. R. RONDA and A. MEIJERINK. Luminescence and energy transfer in $Lu_3Al_5O_{12}$ scintillators co-doped with Ce^{3+} and Tb^{3+}. *The Journal of Physical Chemistry A*, **116(33)**:8464–8474, 2012.

[42] P. ECKERT, H.-C. SCHULTZ-COULON, W. SHEN, R. STAMEN and A. TADDAY. Characterisation studies of silicon photomultipliers. *Nuclear Instruments and Methods in Physics Research Section A: Accelerators, Spectrometers, Detectors and Associated Equipment*, **620(23)**:217–226, 2010.

[43] A. PETROSYAN. Crystal growth of laser oxides in the vertical Bridgman configuration. *Journal of Crystal Growth*, **139(3-4)**:372–392, May 1994.

[44] A. PETROSYAN, K. OVANESYAN, R. SARGSYAN, G. SHIRINYAN, D. ABLER, E. AUFFRAY, P. LECOQ, C. DUJARDIN and C. PEDRINI. Bridgman growth and site occupation in LuAG:Ce scintillator crystals. *Journal of Crystal Growth*, **312(21)**:3136–3142, Oct. 2010.

[45] R. WILLIAMS and K. SONG. The self-trapped exciton. *Journal of Physics and Chemistry of Solids*, **51(7)**:679–716, 1990.

[46] V. BABIN, K. BLAZEK, a. KRASNIKOV, K. NEJEZCHLEB, M. NIKL, T. SAVIKHINA and S. ZAZUBOVICH. Luminescence of undoped LuAG and YAG crystals. *Physica Status Solidi (C)*, **2(1)**:97–100, Jan. 2005.

[47] Y. KUWANO, K. SUDA, N. ISHIZAWA and T. YAMADA. Crystal growth and properties of $(Lu,Y)_3Al_5O_{12}$. *Journal of Crystal Growth*, **260(12)**:159–165, 2004.

[48] M. LETZ, A. GOTTWALD, M. RICHTER, V. LIBERMAN and L. PARTHIER. Temperature-dependent Urbach tail measurements of Lutetium Aluminum garnet single crystals. *Phys. Rev. B*, **81**:155109, April 2010.

[49] Y. SHAO. A new timing model for calculating the intrinsic timing resolution of a scintillator detector. *Physics in medicine and biology*, **52(4)**:1103–17, 2007.

[50] P. BRUZA, V. FIDLER and M. NIKL. Table-top instrumentation for time-resolved luminescence spectroscopy of solids excited by nanosecond pulse of soft X-ray source and/or UV laser. *Journal of Instrumentation*, **6(09)**:9007, Sep. 2011.

[51] S. Derenzo, J. Weber, W. Moses and C. Dujardin. Measurements of the intrinsic rise times of common inorganic scintillators. **1**:152–156, 1999.

[52] M. Weber, S. Derenzo and W. Moses. Measurements of ultrafast scintillation rise times: evidence of energy transfer mechanisms. *Journal of Luminescence*, **87-89**:830–832, 2000.

[53] M. Kronberger, E. Auffray and P. Lecoq. Determination of the absolute light yields of LuYAP and LYSO. *2008 IEEE Nuclear Science Symposium Conference Record*, 1153–1157, 2008.

[54] M. Kronberger. Optimization of the light extraction from heavy inorganic scintillators. Ph.D. thesis, University of Technology, Vienna, 2008.

[55] C. Dujardin, C. Mancini, D. Amans, G. Ledoux, D. Abler, E. Auffray, P. Lecoq, D. Perrodin, A. Petrosyan and K. L. Ovanesyan. LuAG:Ce fibers for high energy calorimetry. *Journal of Applied Physics*, **108(1)**:13510, 2010.

[56] E. Bellamy, G. Bellettini, J. Budagov, F. Cervelli, I. Chirikov-Zorin, M. Incagli, D. Lucchesi, C. Pagliarone, S. Tokar and F. Zetti. Absolute calibration and monitoring of a spectrometric channel using a photomultiplier. *Nuclear Instruments and Methods in Physics Research Section A: Accelerators, Spectrometers, Detectors and Associated Equipment*, **339(3)**:468–476, Feb. 1994.

[57] E. Auffray, B. Frisch, F. Geraci, A. Ghezzi, S. Gundacker, H. Hillemanns, P. Jarron, T. Meyer, M. Paganoni, K. Pauwels, M. Pizzichemi and P. Lecoq. A comprehensive and systematic study of coincidence time resolution and light yield using scintillators of different size, wrapping and doping. *2011 IEEE Nuclear Science Symposium Conference Record*, 64–71, Oct. 2011.

[58] A. Zych, M. de Lange, C. de Mello Donega and A. Meijerink. Analysis of the radiative lifetime of Pr^{3+} d–f emission. *Journal of Applied Physics*, **112(1)**:13536, July 2012.

[59] F. You, A. J. J. Bos, Q. Shi, S. Huang and P. Dorenbos. Thermoluminescence investigation of donor (Ce^{3+}, Pr^{3+}, Tb^{3+}) acceptor (Eu^{3+}, Yb^{3+}) pairs in $Y_3Al_5O_{12}$. *Phys. Rev. B*, **85**:115101, March 2012.

[60] A. Petrosyan, K. Ovanesyan, G. Shirinyan, R. Sargsyan, C. Dujardin and C. Pedrini. Site occupation and solubility limit of Sc in $Lu_3Al_5O_{12}$. *Journal of Crystal Growth*, **338(1)**:143–146, 2012.

[61] M. Fasoli, a. Vedda, M. Nikl, C. Jiang, B. Uberuaga, D. Andersson, K. McClellan and C. Stanek. Band-gap engineering for removing shallow traps in rare-earth $Lu_3Al_5O_{12}$ garnet scintillators using Ga^{3+} doping. *Physical Review B*, **84(8)**:1–4, Aug. 2011.

[62] J. A. Mares, M. Nikl, A. Beitlerova, P. Horodysky, K. Blazek, K. Bartos and C. D'Ambrosio. Scintillation properties of Ce^{3+} - and Pr^{3+} -doped LuAG, YAG and mixed $Lu_xY_{1-x}AG$ Garnet Crystals. *Nuclear Science, IEEE Transactions on*, in press, 2012.

[63] S. W. S. Mc Keever and R. Aviv. Luminescence models, vol. 27. Cambridge university press, 1998.

[64] D. J. Huntley. An explanation of the power-law decay of luminescence. *Journal of Physics: Condensed Matter*, **18(4)**:1359–1365, Feb. 2006.

[65] M. Nikl, V. V. Laguta and A. Vedda. Energy transfer and charge carrier capture processes in wide-band-gap scintillators. *Physica Status Solidi (a)*, **204(3)**:683–689, 2007.

[66] M. Nikl. Energy transfer phenomena in the luminescence of wide band-gap scintillators. *Physica Status Solidi (a)*, **202(2)**:201–206, Jan. 2005.

[67] M. Nikl, J. Mares, A. Yoshikawa, H. Ogino, K. Nejezchleb, K. Blazek and A. Vedda. Ten years of the LuAG-based scintillators development. State of art and prospects. In SCINT2011, Giessen, Germany., 2011.

[68] A. Vedda et al. to be published.

[69] M. Nikl, J. A. Mares, N. Solovieva, J. Hybler, A. Voloshinovskii, K. Nejezchleb and K. Blazek. Energy transfer to the Ce^{3+} centers in $Lu_3Al_5O_{12}$:Ce scintillator. *Physica Status Solidi (a)*, **201(7)**:41–44, May 2004.

[70] Y. Zorenko, A. Voloshinovskii, V. Savchyn, T. Voznyak, M. Nikl, K. Nejezchleb, V. Mikhailin, V. Kolobanov and D. Spassky. Exciton and antisite defect-related luminescence in $Lu_3Al_5O_{12}$ and $Y_3Al_5O_{12}$ garnets. *physica status solidi (b)*, **244(6)**:2180–2189, 2007.

[71] K. Pauwels, E. Auffray, S. Gundacker, A. Knapitsch and P. Lecoq. Effect of aspect ratio on the light output of scintillators. *Nuclear Science, IEEE Transactions on*, **59(5)**:2340–2345, 2012.

[72] A. Del Guerra and N. Belcari. State-of-the-art of PET scanners for small animal and breast cancer imaging. *Nuclear Instruments and Methods in Physics Research Section A: Accelerators, Spectrometers, Detectors and Associated Equipment*, **580(2)**:910–914, Oct. 2007.

[73] K. Ziemons, R. Barbier, G. Brandenburg, P. Bruyndonckx, Y. Choi, D. Christ, N. Costes *et al.* The ClearPET project: development of a 2nd generation high-performance small animal PET scanner. *Nuclear Instruments and Methods in Physics Research Section A: Accelerators, Spectrometers, Detectors and Associated Equipment*, **537(1-2)**:307–311, Jan. 2005.

[74] M. Abreu, D. Aguiar, E. Albuquerque, F. Almeida, P. Almeida, P. Amaral, E. Auffray *et al.* Clear-PEM: A PET imaging system dedicated to breast cancer diagnostics. *Nuclear Instruments and Methods in Physics Research Section A: Accelerators, Spectrometers, Detectors and Associated Equipment*, **571(1-2)**:81–84, Feb. 2007.

[75] W. Drozdowski, P. Dorenbos, A. J. J. Bos, J. T. M. D. Haas, S. Kraft, E. Maddox, A. Owens, F. G. A. Quarati, C. Dathy and V. Ouspenski. Effect of proton dose, crystal size and Cerium concentration

on scintillation yield and energy resolution of LaBr$_3$:Ce. *Nuclear Science, IEEE Transactions on*, **54(3)**:736–740, 2007.

[76] U. Heinrichs, A. Blume, N. Bu, R. Engels, G. Kemmerling, S. Weber and K. Ziemons. Statistical studies on the light output and energy resolution of small LSO single crystals with different surface treatments combined with various reflector materials. **486**:60–66, 2002.

[77] J. de Haas, P. Dorenbos and C. van Eijk. Measuring the absolute light yield of scintillators. *Nuclear Instruments and Methods in Physics Research Section A: Accelerators, Spectrometers, Detectors and Associated Equipment*, **537(1-2)**:97–100, Jan. 2005.

[78] J. S. Huber, W. W. Moses, M. S. Andreaco, M. Loope, C. L. Melcher and R. Nutt. Geometry and surface treatment dependence of the light collection from LSO crystals. **437**:374–380, 1999.

[79] W. Drozdowski, A. J. Wojtowicz, T. Lukasiewicz and J. Kisielewski. Scintillation properties of LuAP and LuYAP crystals activated with Cerium and Molybdenum. *Nuclear Instruments and Methods in Physics Research Section A: Accelerators, Spectrometers, Detectors and Associated Equipment*, **562(1)**:254–261, 2006.

[80] C. Dujardin, C. Pedrini, W. Blanc, J. C. Gacon, J. C. van't Spijker, O. W. V. Frijns, C. W. E. van Eijk, P. Dorenbos, R. Chen, A. Fremout, F. Tallouf, S. Tavernier, P. Bruyndonckx and A. G. Petrosyan. Optical and scintillation properties of large LuAlO$_3$:Ce^{3+} crystals. *Journal of Physics: Condensed Matter*, **10(13)**:3061, 1998.

[81] M. Moszynski, M. Kapusta, M. Mayhugh, D. Wolski and S. Flyckt. Absolute light output of scintillators. *Nuclear Science, IEEE Transactions on*, **44(3)**:1052–1061, June 1997.

[82] M. Gierlik, M. Moszynski, A. Nassalski, A. Syntfeld-Kazuch, T. Szczesniak and L. Swiderski. Investigation of absolute light output measurement techniques. **3**:1583–1588, Nov. 2006.

[83] S. Yamamoto, H. Horii, M. Hurutani, K. Matsumoto and M. Senda. Investigation of single, random, and true counts from natural radioactivity in LSO-based clinical PET. *Annals of Nuclear Medicine*, **19**:109–114, 2005.

[84] F.-X. Gentit. Litrani: a general purpose Monte-Carlo program simulating light propagation in isotropic or anisotropic media. Tech. Rep. CMS-NOTE-2001-044, CERN, Geneva, October 2001.

[85] D. Wahl, V. Mikhailik and H. Kraus. The Monte-Carlo refractive index matching technique for determining the input parameters for simulation of the light collection in scintillating crystals. *Nuclear Instruments and Methods in Physics Research Section A: Accelerators, Spectrometers, Detectors and Associated Equipment*, **570(3)**:529–535, Jan. 2007.

[86] C. Mancini. Mise en place d'un microscope confocal achromatique. Ph.D. thesis, Université Claude Bernard - Lyon I, 2010.

[87] H. Ogino, A. Yoshikawa, M. Nikl, A. Krasnikov, K. Kamada and T. Fukuda. Growth and scintillation properties of Pr-doped $Lu_3Al_5O_{12}$ crystals. *Journal of Crystal Growth*, **287(2)**:335–338, 2006.

[88] M. Sugiyama, Y. Yokota, Y. Fujimoto, T. Yanagida, Y. Futami, S. Kurosawa and A. Yoshikawa. Dopant segregation in rare earth doped Lutetium Aluminum garnet single crystals grown by the micro-pulling down method. *Journal of Crystal Growth*, **352(1)**:110–114, 2012.

[89] D. Sangla, N. Aubry, A. Nehari, A. Brenier, O. Tillement, K. Lebbou, F. Balembois, P. Georges, D. Perrodin, J. Didierjean and J. Fourmigue. Yb-doped $Lu_3Al_5O_{12}$ fibers single crystals grown under stationary stable state for laser application. *Journal of Crystal Growth*, **312(1)**:125–130, 2009.

[90] R. D. Shannon. Revised effective ionic radii and systematic studies of interatomic distances in halides and chalcogenides. *Acta Crystallographica Section A*, **32(5)**:751–767, Sep 1976.

[91] N. Akchurin, O. Atramentov, K. Carrell, K. Gümü, J. Hauptman, H. Kim, H. Paar, A. Penzo and R. Wigmans. Separation of scintillation and Cherenkov light in an optical calorimeter. *Nuclear Instruments and Methods in Physics Research Section A: Accelerators, Spectrometers, Detectors and Associated Equipment*, **550(1-2)**:185–200, Sep. 2005.

[92] G. Mavromanolakis, E. Auffray and P. Lecoq. Studies on sampling and homogeneous dual readout calorimetry with meta-crystals. *Journal of Instrumentation*, **6(10)**:10012, Oct. 2011.

[93] S. Agostinelli, J. Allison, K. Amako, J. Apostolakis, H. Araujo, P. Arce, M. Asai *et al.* Geant4a simulation toolkit. *Nuclear Instruments and Methods in Physics Research Section A: Accelerators, Spectrometers, Detectors and Associated Equipment*, **506(3)**:250–303, 2003.

[94] J. Allison, K. Amako, J. Apostolakis, H. Araujo, P. Dubois, M. Asai, G. Barrand *et al.* Geant4 developments and applications. *Nuclear Science, IEEE Transactions on*, **53(1)**:270 –278, Feb. 2006.

[95] B. Baumbaugh, B. Dolezal, A. Heering, D. Karmgard, M. McKenna, R. Ruchti, S. Sharkey, J. Taylor, M. Trip and M. Vigneault. Update on fibrous light source development. *CMS Forward Calorimetry Task Force*, June 2012.

[96] M. Derdzyan, K. Ovanesyan, A. Petrosyan, A. Belsky, C. Dujardin, C. Pedrini, E. Auffray, P. Lecoq, M. Lucchini and K. Pauwels. Radiation hardness of LuAG:Ce and LuAG:Pr scintillator crystals. *Journal of Crystal Growth*, **361(0)**:212–216, 2012.

[97] K. Kamada, T. Yanagida, T. Endo, K. Tsutumi, Y. Usuki, M. Nikl, Y. Fujimoto, A. Fukabori and A. Yoshikawa. 2 inch diameter single crystal growth and scintillation properties of $Ce:Gd_3Al_2Ga_3O_{12}$. *Journal of Crystal Growth*, **352(1)**:88–90, 2012.

[98] V. Chani, A. Yoshikawa, Y. Kuwano, K. Hasegawa and T. Fukuda. Growth of $Y_3Al_5O_{12}$:Nd fiber crystals by micro-pulling-down technique. *Journal of Crystal Growth*, **204(1-2)**:155–162, July 1999.

[99] D. SANGLA, N. AUBRY, J. DIDIERJEAN, D. PERRODIN, F. BALEMBOIS, K. LEBBOU, A. BRENIER, P. GEORGES, O. TILLEMENT and J. M. FOUR-MIGUE. Diode-pumped laser with Yb:YAG single-crystal fiber grown by the micro-pulling down technique. *Applied Physics B-Lasers and Optics*, **94(2)**:203–207, Feb. 2009.